DISS. ETH Nr. 29761

FRACTURE INITIATION AND PROPAGATION IN ANISOTROPIC ROCKS

A thesis submitted to attain the degree of

DOCTOR OF SCIENCES

(Dr. Sc. ETH Zurich)

presented by

Mahsa Sakha

M.Sc Mechanical engineering, Amirkabir University of Technology

born on 27.05.1992

accepted on the recommendation of

Prof. Dr. Thomas Driesner
Prof. Dr. Laura De Lorenzis
Prof. Dr. Keita Yoshioka
Dr. Morteza Nejati

2023

Acknowledgements

Without a doubt, this journey could have come to an end with the great support and guidance of many people, to whom I wish to express my sincere gratitude.

I would like to thank my supervisor, Prof. Dr. Thomas Driesner, who has shown unwavering trust in me from the very beginning of my PhD journey. His support and confidence have been instrumental in helping me find my path through this challenging journey. Thomas taught me a valuable lesson that in science, it is not about good or bad results, but rather about how we approach and address scientific problems. This lesson has greatly enhanced my methodology and enabled me to overcome the difficulties I faced throughout my entire PhD.

I am also indebted to the guidance and supervision of Dr. Morteza Nejati during the first half of my PhD. Under his mentorship, I developed a critical mindset and learned to approach solutions with a healthy skepticism. His dedication to training me as an independent researcher is something I am sincerely grateful for.

In the latter half of my PhD, I had the privilege of being supervised by Prof. Dr. Laura De Lorenzis, a highly knowledgeable and sophisticated mentor. With her expertise in physics of fracturing and computational mechanics, she greatly expanded my understanding and skills in these areas. I am truly honored to have had the opportunity to learn from her.

I would like to extend my gratitude to those who have assessed the quality of my thesis and evaluated my knowledge throughout my PhD. Particularly, I am grateful to Prof. Dr. Madonna and Prof. Dr. Ruh for their meticulous evaluation during my qualification exam. Special thanks to Prof. Dr. Lecampion for reviewing my initial proposal and offering insightful comments at early stage of my PhD. Their constructive feedback inspired the development of the third chapter of my thesis. Furthermore, I would like to express my appreciation to Prof. Dr. Yoshioka for accepting the invitation to be a part of my examination committee. Their presence and input during the evaluation process added significant value to my research.

I would like to seize this moment to express my heartfelt gratitude to my colleagues and friends in the Department of Earth Sciences and the Department of Mechanical and Process Engineering. Their unwavering guidance, support, and patience have been of immense value to me during the highs and lows of my PhD journey. I will never forget how each and everyone of you has offered guidance and stood by me during this challenging time.

I am profoundly indebted to my loving family, and words cannot fully express the depth of my gratitude for their support. Without their unwavering love, countless sacrifices, and constant encouragement, I would not have achieved the level of success I have today. My dear parents, sisters Maryam and Mona, have been a constant source of inspiration, and I am forever grateful for their unwavering support. To my beloved husband, Naeim, your love, understanding, and belief in me have guided me through the darkest of times. I am truly blessed to have such an incredible family by my side.

To my beloved Naeim and my family

Abstract

A comprehensive understanding of fracturing in rock formations requires a deep knowledge of the intrinsic mechanical characteristics of rock-type materials. While conventional isotropy-based models can be easily implemented from mathematical and numerical perspectives, the unique arrangement found in many rocks, characterized by a preferred orientation of constituent minerals and micro-cracks, sets them apart from isotropic solids. This distinctiveness aligns them more closely with transversely isotropic materials. The introduction of directional dependency in mechanical properties adds a layer of complexity to the fracturing problem, transforming the trajectory of fracture formation into an enigmatic puzzle. No longer readily predictable or a priori, this directional dependency poses a new challenge that calls for advanced theories and modeling techniques to ensure accurate fracture analysis in anisotropic rock formations.

While predicting fracture initiation and propagation in anisotropic rock-type materials is still a challenging task, the complexity further intensifies with the introduction of complex mixed-mode I/II loading regimes within the subsurface. This inevitable complication underscores the need for a robust approach. This thesis strives to address both these challenges in fracture mechanics by offering modified theories and implementing advanced models capable of effectively capturing fracture behavior in anisotropic solids. Leveraging the availability of experimental data sets, this research evaluates the robustness of the proposed theories. Moreover, it adopts an integrated validation strategy to endorse the presented results and establish their reliability in cases where no experimental data is available. By combining theoretical advancements, numerical simulations, and reliable validation, this thesis seeks to deepen our understanding of fracture mechanics in anisotropic rock-type materials and provide valuable insights for practical applications.

This thesis presents valuable experimental data sets of Grimsel Granite samples undergoing mixed-mode loading through a modified SCB test. It unveils a competition between the material anisotropy and loading. The competition between material anisotropy and loading, not understood by classical energy-based fracture growth criteria, is better captured using the Maximum Tangential Stress theory. Modifications to energy-based theories address this oversight, as the modified versions allow tensile crack propagation only under opening displacement while distinguish between shearing and opening contributions. Additionally, the thesis explores the robustness of phase-field modeling in reproducing experimental data. Surprisingly, despite assuming direction-independent fracture toughness, the phase-field model tracks the fracture trajectory with relative accuracy. This phase-field model, however, is unable to precisely reproduce the ultimate loading at the onset of fracture, which leads to an underestimation in the predicted effective fracture toughness.

To understand hydraulic fracture initiation within anisotropic rock formations, this thesis adopts the theory of finite fracture mechanics, and extends its scope to the behavior of an edge crack in an infinite anisotropic formation interacting with a pressurized hole. Through this investigation, the intricate interplay between material and stress anisotropy, coupled with the size effect, emerges as a key determinant of initiation parameters. To address this complex problem, in the first attempt, a combination of analytical relations and a specific numerical scheme named DDM (Displacement Discontinuity Method) is employed. In the absence of experimental data, finite element modeling is utilized to validate and reproduce the obtained results. Notably, the final observations confirm the significant influence of the interplay between *Loading*- and *Material*- dominance regimes on determining hydraulic fracture initiation parameters in an anisotropic formation.

The thesis ends with a comprehensive discussion of the main findings and observations, aimed at unveiling the underlying physics governing fracture initiation and propagation in anisotropic solids. It delineates the similarities and differences in various fracture mechanisms, shedding light on their distinct characteristics. Moreover, the thesis paves the way for future investigations into fracturing in anisotropic solids under more complex conditions, offering promising avenues for further exploration in this field.

Abstract

Ein umfassendes Verständnis von Brüchen in Gesteinsformationen erfordert eine tiefgehende Kenntnis der intrinsischen mechanischen Eigenschaften von Gesteinsmaterialien. Während konventionelle Isotropie-basierte Modelle aus mathematischer und numerischer Sicht leicht umsetzbar sind, unterscheidet sich die einzigartige Anordnung vieler Gesteine, die durch eine bevorzugte Ausrichtung der Bestandteile von Mineralien und Mikrorissen gekennzeichnet ist, von isotropen Feststoffen. Diese Besonderheit bringt sie näher an transversal isotrope Materialien heran. Die Einführung von richtungsabhängigen mechanischen Eigenschaften fügt dem Bruchproblem eine Schicht Komplexität hinzu und verwandelt die Frakturbildung in eine rätselhafte Herausforderung. Diese Richtungsabhängigkeit ist nicht mehr leicht vorhersagbar oder a priori, was eine neue Herausforderung darstellt, die fortschrittliche Theorien und Modellierungstechniken erfordert, um eine genaue Bruchanalyse in anisotropen Gesteinsformationen sicherzustellen.

Die Vorhersage von Bruchinitiierung und -ausbreitung in anisotropen Gesteinsmaterialien ist immer noch eine anspruchsvolle Aufgabe. Die Komplexität intensiviert sich weiter durch die Einführung von komplexen gemischten I/II-Belastungsregimen im Untergrund. Diese unvermeidliche Komplikation unterstreicht die Notwendigkeit eines robusten Ansatzes. Diese Dissertation versucht, beide Herausforderungen in der Bruchmechanik anzugehen, indem sie modifizierte Theorien präsentiert und fortschrittliche Modelle implementiert, die in der Lage sind, das Bruchverhalten in anisotropen Feststoffen effektiv zu erfassen. Unter Nutzung von vorhandenen experimentellen Datensätzen bewertet diese Forschung die Robustheit der vorgeschlagenen Theorien. Darüber hinaus wird eine integrierte Validierungsstrategie angenommen, um die präsentierten Ergebnisse zu unterstützen und deren Zuverlässigkeit in Fällen zu etablieren, in denen keine experimentellen Daten verfügbar sind. Durch die Kombination von theoretischen Fortschritten, numerischen Simulationen und zuverlässiger Validierung versucht diese Dissertation, unser Verständnis von Bruchmechanik in anisotropen Gesteinsmaterialien zu vertiefen und wertvolle Erkenntnisse für praktische Anwendungen zu liefern.

Diese Dissertation präsentiert wertvolle experimentelle Datensätze von Grimsel-Granitproben, die einer gemischten Belastung im Rahmen eines modifizierten SCB-Tests ausgesetzt sind. Sie enthüllt einen Wettbewerb zwischen Materialanisotropie und Belastung. Der Wettbewerb zwischen Materialanisotropie und Belastung, der von klassischen energiebasierten Bruchwachstumskriterien nicht verstanden wird, wird besser durch die Theorie der maximalen Tangentialspannung erfasst. Modifikationen an energiebasierten Theorien beheben diesen Fehler, da die modifizierten Versionen Rissausbreitung unter Zugöffnung ermöglichen und zwischen Scher- und Öffnungsbeiträgen unterscheiden. Darüber hinaus erforscht die Dissertation die Robustheit der Phasenfeldmodellierung bei der Reproduktion experimenteller Daten. Überraschenderweise verfolgt das Phasenfeldmodell trotz Annahme einer richtungsunabhängigen Bruchzähigkeit die Bruchbahn relativ genau. Dieses Phasenfeldmodell kann jedoch die ultimative Belastung zu Beginn des Bruchs nicht genau reproduzieren, was zu einer Unterschätzung der vorhergesagten effektiven Bruchzähigkeit führt.

Um das Entstehen hydraulischer Rissbildungen in anisotropen Gesteinsformationen zu verstehen, greift diese Dissertation auf die Theorie der endlichen Rissmechanik zurück und erweitert ihren Anwendungsbereich auf das Verhalten eines Kantenrisses in einer unendlichen anisotropen Formation, der mit einem unter Druck stehenden Loch interagiert. Durch diese Untersuchung wird das komplexe Zusammenspiel zwischen Material- und Spannungsanisotropie in Verbindung mit dem Größeneffekt als entscheidender Faktor für die Initiierungsparameter deutlich. Um dieses komplexe Problem anzugehen, wird im ersten Versuch eine Kombination aus analytischen Beziehungen und einer speziellen numerischen Methode namens DDM (Displacement Discontinuity Method) verwendet. In Ermangelung experimenteller Daten wird die Methode der Finite-Elemente-Modellierung genutzt, um die erhaltenen Ergebnisse zu validieren und zu reproduzieren. Bemerkenswert ist, dass die abschließenden Beobachtungen die signifikante Rolle des Zusammenspiels zwischen den Regimen der *Belastungsdominanz* und *Materialdominanz* bei der Bestim-

mung der Initiierungsparameter hydraulischer Rissbildungen in einer anisotropen Formation bestätigen.

Die Dissertation endet mit einer umfassenden Diskussion der wichtigsten Erkenntnisse und Beobachtungen, die darauf abzielen, die zugrunde liegende Physik bei der Initiierung und Ausbreitung von Brüchen in anisotropen Feststoffen aufzudecken. Sie grenzt die Ähnlichkeiten und Unterschiede bei verschiedenen Bruchmechanismen ab und wirft Licht auf ihre charakteristischen Eigenschaften. Darüber hinaus ebnet die Dissertation den Weg für zukünftige Untersuchungen von Brüchen in anisotropen Feststoffen unter komplexeren Bedingungen und bietet vielversprechende Ansätze für weitere Erkundungen in diesem Bereich.

List of Figures

1.1 Comparing the size of nonlinear hardening and softening regions ahead of the crack tip in (a) brittle materials, (b) quasi-brittle materials, and (c) ductile materials. 2

2.1 (a) Schematic view of hydraulic fracturing around boreholes in the presence of mixed-mode I/II loading; The parallel lines show the isotropy plane (bedding or foliation) in transversely isotropic rocks. Here, a compressive stress is represented with a positive value. (b) Schematic illustration of the interaction of loading and anisotropy based on the sign of the mode-mixity parameter $\lambda = K_{\mathrm{II}}/(K_{\mathrm{I}}^2 + K_{\mathrm{II}}^2)^{1/2}$. The principal axes 1 and 2 respectively denote the strong and weak directions of the material. 16

2.2 Schematic illustration of the principal values of (a) mode I and (b) true mode II fracture toughness and their variations with direction in an anisotropic material; (c) variations of the fracture toughness associated with mode I and true mode II in Grimsel Granite. 22

2.3 Schematics of the SCB test setup for (a) $\lambda < 0$ and (b) $\lambda > 0$; (c) a tested sample of Grimsel Granite with the configuration $\lambda = +0.71$ and $\beta = 75°$. 24

2.4 Schematic representation of the existing fracture growth criteria when the kinked crack is subjected to mixed tensile and shear stresses. 29

2.5 Comparison of the experimental data on the kink angle, θ_0, and the effective fracture toughness, K_{eff}^c, and the predictions of the MTS, MERR, and MSED criteria in their classical forms, i.e. Eqs. (2.1), (2.5), and (2.9), respectively. 34

2.6 Schematic representation of the decomposition of the energy release rate into tensile and shear components. 36

2.7 Comparison of experimental data on kink angle, θ_0, and the effective fracture toughness, K_{eff}^c), with the predictions of the MTS (Eq. 2.1), modified MERR (Eq. 2.15), and modified MSED (Eq. 2.19). 41

2.8 Comparison of experimental data on θ_0 and K_{eff}^c with the predictions of the MERR criterion with different assumptions. 45

2.9 Comparison of the experimental data on θ_0 and K_{eff}^c with the predictions of the MTS, modified MERR, and modified MSED criteria when T-stress is ignored. 48

3.1 A sketch of the configuration governing the initiation problem from an unnotched wellbore wall. (a) the potential crack at the instant before initiation (b) the instantaneous formation of the initial cracks when pressure reaches p_{b0}. Note that the parallel grey lines inclined at the angle β indicate the orientation of the isotropy planes of the formation and the direction 2 is aligned with the symmetry axis of the material. 55

3.2 Two symmetrical cracks radially emanating from a cylindrical wellbore subjected to in-situ compressive stresses. (a) Implementation of Bueckner's theorem based on superposition of loaded intact body (b), and unloaded cracked body (c). 61

3.3 Comparison of the wellbore initiation pressure and length as a function of Irwin's number $\mathcal{I}$ estimated by the mixed criterion applied to the isotropic formation under different values for the dimensionless far-field compressive mean stress; isotropy is originally assumed by directly applying the isotropic relations [Lecampion, 2012] or approached by taking limit of the relations corresponding to anisotropic solids. 67

3.4 Variations of wellbore initiation parameters as functions of the orientation β for different material and stress anisotropy ratios. Here, Irwin's number $\mathcal{I}$ is kept to a constant value of 0.96. Note that the legend denoting the color code used for each material anisotropy, applies to all subsequent plots. The marker star shows the highest deviation, ϕ_0^* at each material anisotropy when $\lambda \geq 1$. In order to analyze the trend in the data, a Gaussian smoothing technique was applied. This method effectively smoothed the trend while preserving the overall shape of the original data. 69

3.5 Variation of wellbore initiation parameters (pressure and length) with Irwin's number for different material anisotropy ratios under a constant stress anisotropy ($\lambda = 1.5$). Here, the results are provided for the following three different anisotropy orientations: $\beta = 0°, 45°, 75°$. Note that the legend denoting the color code used for each material anisotropy, applies to all subsequent plots. 73

3.6 Variation of wellbore initiation pressure with the material anisotropy at different Irwin's number $\mathcal{I}$. Here, the stress anisotropy is kept constant at $\lambda = 1.5$. 75

4.1 Phase-field evolution of an initial edge crack within an isotropic square plate subjected to shearing. (a) Symmetric bifurcated crack propagation using a symmetric compression-tension phase-field model. (b) Singular crack kinking in the tensile region using an asymmetric compression-tension phase-field modeling. 82

4.2 (a) The Mohr circle of $\boldsymbol{\epsilon}$ showing the eigenvalues/vectors of the strain tensor. (b) the Mohr circle of $(\sqrt{\boldsymbol{\mu}}\boldsymbol{\epsilon})$ showing the eigenvalues/vectors of the tensor $\boldsymbol{\Psi}_\mu$. 84

4.3 Schematics of the square plate with an initial edge crack under (a) the tensile loading, and (b) the shear loading. The material coordinate system is rotated by the angle β with respect to the original coordinate system xy. 90

4.4 (a) Phase-field evolution, and comparison of (b) the fracture path, and (c) the load-displacement relationship for the cracked square plate under tensile loading: present study vs. Ziaei-rad et al. [2023]. 91

4.5 The effect of boundary conditions on the phase-field trajectory of a square plate with a material orientation of $\beta = -\pi/4$. (a) the top side of the plate is constrained along the x-direction, leading to the propagation on the weaker direction of the material in elasticity [Dijk et al., 2020; Ziaei-rad et al., 2023]. (b) the top side is free to move along the x-direction, leading to the propagation on the strong direction of the material in elasticity [Hirshikesh et al., 2021]. 92

4.6 Phase-field evolution, and comparison of (b) the fracture path, and (c) the load-displacement relationship for the cracked square plate under shear loading: present study vs. Ziaei-rad et al. [2023]. 94

4.7 Schematics of the SCB test setup for two types of mixed-mode loading (a) $K_{\mathrm{II}}/K_{\mathrm{I}} \leq 0$, and (b) $K_{\mathrm{II}}/K_{\mathrm{I}} > 0$. 96

4.8 The variation of span ratios for different material orientations and mode-mixity ratios. 97

4.9 Polar plot of the fracture toughness for Grimsel Granite (a) as a transversely isotropic material under plane-strain condition, and (b) assumed as an isotropic solid. The fracture toughness is given in N/mm 99

4.10 Comparison of the experimental data on the kink angle, θ_0, and the effective fracture toughness, $K^{\mathrm{c}}_{\mathrm{eff}}$, with the phase-field simulations and the predictions reported by Sakha et al. [2022] based on the MTS, modified MERR, and modified MSED criteria for the mode-mixity $\lambda = -0.37$. (a) Evolution of phase-field, (b) displacement magnitude (in mm), and (c) y-displacement (in mm) for material orientation $\beta = 75°$. 101

4.11 Comparison of the experimental data on the kink angle, θ_0, and the effective fracture toughness, $K_{\text{eff}}^{\text{c}}$, with the phase-field simulations and the predictions reported by Sakha et al. [2022] based on the MTS, modified MERR, and modified MSED criteria for the mode-mixity $\lambda = 0.37$. (a) Evolution of phase-field, (b) displacement magnitude (in mm), and (c) y-displacement (in mm) for material orientation $\beta = 45°$. 102

A.1.1 An anisotropic plane with two local coordinate systems x′y′ and nt which coincide with the principal material directions and the direction of fracture growth, respectively. The global coordinate system xy makes the angle $-\beta$ with respect to x′y′. A-2

C.1.1 The distribution of the hoop stress around the notch-free wellbore at initiation obtained by finite element (FE) modelling and analytical relations (see B.1) for different material anisotropy ratios and orientations. C-2

C.1.2 Comparing wellbore initiation parameters calculated through FEM and DDM for various material anisotropy under stress anisotropy $\lambda = 2$. . . . C-3

List of Tables

2.1 A list of studies that evaluated three well-know fracture growth criteria in anisotropic materials using experimental data. 18

2.2 The elastic properties and fracture toughness values measured for Grimsel Granite. $\kappa_1, \kappa_2, \kappa_3$ are reported for plane-strain conditions. The elastic moduli and fracture toughness are given in GPa and MPa$\sqrt{\text{m}}$, respectively, and the FPZ length is given in mm. 21

2.3 The directional dependence of the different measures of fracture toughness in tensile- and shear-based failure mechanisms, adopted from Nejati et al. [2020b, 2021a]. Here, $\xi = E/E'$ is the anisotropy ratio of Young's modulus, $\kappa_1 = \kappa_2 = \kappa_3 = 1$ for the plane-stress condition and $\kappa_1 = 1 - \nu^2$, $\kappa_2 = 1 - \xi\nu'^2$, $\kappa_3 = 1 + \nu$ for the plane-strain condition. 23

2.4 Geometry and loading details of the SCB tests for different experiment sets conducted on Grimsel Granite ($R = 47.5$ mm). 25

2.5 Calculated values of the dimensionless T-stress, $\bar{T}$, for the four sets of experiments at different angles of β. 26

2.6 Comparison of the prediction errors for different fracture growth criteria. The error norms are defined in Eq. (2.20). 42

2.7 Comparison of the prediction errors for different formulations of the MERR criterion. The error norms are defined in Eq. (2.20). 45

2.8 Comparison of the prediction errors for different formulations of the MSED criterion. The error norms are defined in Eq. (2.20). 47

3.1 The directional dependence of the material tensile strength and the different measures of fracture toughness in tensile-based failure mechanisms, adopted from Nejati et al. [2020b, 2021b]. Here, $\xi = E/E'$ is the anisotropy ratio of Young's modulus, $\kappa_1 = \kappa_2 = 1$ for the plane-stress condition and $\kappa_1 = 1 - \nu^2, \ \kappa_2 = 1 - \xi\nu'^2,$ for the plane-strain condition. 59

3.2 The elastic modulus, strength, and fracture toughness values measured for Grimsel Granite [Nejati et al., 2020b, 2021b]. The strength, stress, and elastic modulus are given in MPa. This table reports size-independent values of fracture toughness in MPa$\sqrt{\text{m}}$. The stress states is also taken from Dutler et al. [2020]. 68

4.1 Material properties for the orthotropic material studied for validation with numerical results given by Ziaei-rad et al. [2023]. 90

4.2 Material properties for the Grimsel Granite taken from Sakha et al. [2022]. 98

4.3 The directional dependency of the different measures of fracture toughness adopted from Nejati et al. [2020b, 2021a]. The parameters ξ, and κ_is are related to the elastic constants through the definition given by Sakha et al. [2022]. 99

A.2.1 Comparison of the prediction errors for different techniques used to determine the ERR function. The error functions are defined in Eq. (2.20). . . A-11

Contents

Acknowledgements **ii**

Abstract **v**

Abstract **viii**

1 Introduction **1**

1.1 Brittle fracture in rocks 1
1.2 Fracture initiation, finite fracture mechanics 3
1.3 Fracture propagation, LEFM and T-stress 4
1.4 Fracture modelling 6
1.5 Fracturing within subsurface 9
1.6 Thesis outline 10

2 Crack growth criteria **13**

2.1 Abstract 13
2.2 Introduction 14
2.3 Experimental setup 20
  2.3.1 Material 20
  2.3.2 Tests 23
2.4 Fracture growth criteria 26
  2.4.1 Maximum tangential stress (MTS) 26
  2.4.2 Maximum energy release rate (MERR) 29

2.4.3 Maximum strain energy density (MSED) 31

2.5 Experimental data versus theoretical predictions 32

2.6 Revisiting energy-based growth criteria 35

2.6.1 Modification of the MERR criterion 35

2.6.2 Modification of the MSED criterion 39

2.6.3 Re-assessment of the energy-based fracture criteria 41

2.7 Discussion 42

2.7.1 MTS criterion 43

2.7.2 MERR criterion 44

2.7.3 MSED criterion 46

2.7.4 Effects of T-stress 47

2.8 Conclusions 49

3 Hydrualic fracture initiation 51

3.1 Abstract 51

3.2 Introduction 52

3.3 Problem description 54

3.4 Initiation criteria 56

3.4.1 Strength-based criterion 56

3.4.2 Mixed criterion: strength and energy 57

3.5 Rock anisotropy 58

3.6 Elasticity problem 60

3.7 Solution algorithm and non-dimensionalization 64

3.8 Results and discussion 66

3.8.1 Anisotropy effect on the initiation parameters 67

3.8.2 Size effect on the initiation parameters 72

3.8.3 Comparison of strength-based and mixed criteria 74
3.9 Conclusions 76

4 Phase-field modelling 77
4.1 Abstract 77
4.2 Introduction 78
4.3 Model Formulation: Phase-field 80
4.3.1 Miehe decomposition for isotropic materials 83
4.3.2 Generalized Miehe decomposition for orthotropic materials 85
4.4 Results and discussions 88
4.4.1 Validation with numerical studies 89
4.4.2 Validation with experimental data 95
4.5 Conclusion 104

5 Conclusion 105
5.1 Unveiling the role of material anisotropy 106
5.2 Fracture path: not a priori assumption 107
5.3 Toward a sophisticated fracture model 107
5.4 Outlook 109

A ELASTICITY PROBLEM: KINKED CRACK IN ANISOTROPIC SOLIDS A-1
A.1 Theoretical background on anisotropic elasticity A-1
A.2 Energy release rate (ERR) function A-6
A.2.1 Dislocation technique A-7
A.2.2 Approximate solution A-10
A.2.3 Comparison of the approximate solution with dislocation technique A-11

B ELASTICITY PROBLEM: ANISOTROPIC PLANE WITH A HOLE B-1

B.1 Infinite anisotropic plane with a circular hole B-1

B.2 Infinite anisotropic plane with an inclusion B-3

C MODELING HYDRAULIC FRACTURE INITIATION C-1

C.1 Finite element modelling C-1

Chapter 1

Introduction

1.1 Brittle fracture in rocks

Brittle or ductile fracturing is often associated with the failure of a material, signaling the end of a component's lifetime and sounding the alarm for potential hazards [Kiener and Han, 2022]. However, over the past 100 years since Griffith's theory on brittle fracture [Griffith, 1921], brittle fracturing has evolved into a functional tool in various geo-engineering applications such as shale oil and gas extraction, mining operations, enhanced geothermal systems (EGS), carbon sequestration projects, wastewater injection plans, and a range of other endeavors.

One such example is in enhanced geothermal systems, where brittle fracture in quasi-brittle rock formations can be utilized to enhance the permeability of the reservoir [McClure and Horne, 2014]. In cases where the hot rock lacks appreciable permeability necessary for effective convective heat transport and economically thermal energy harvesting, pressurized fluid is injected into the reservoir to either create new cracks or expand pre-existing fractures [Krietsch et al., 2020b; Stober and Bucher, 2021; Fink et al., 2022]. This hydraulic stimulation generally proceeds in a stable manner, however, it can induce seismic activity by altering the stress field in the reservoir [Cuenot et al., 2011; Randolph and Saar, 2011]. To address this concern and mitigate unwelcome induced seismicity, a comprehensive understanding of fracture behavior in quasi-brittle rock formations is indispensable. Such knowledge will enable us to understand and, importantly control fracturing mechanisms within the subsurface by optimizing the design and operation of similar geo-engineering applications in a reliable and risk-minimized manner.

The first step towards gaining this knowledge is to understand brittle fracturing in rock formations, particularly when the rock behaves as a quasi-brittle material. Unlike brittle materials, where the inelastic region is negligible (i.e. in order of micrometers [Bažant et al., 2022]) compared to the elastic asymptotic stress field, in quasi-brittle and ductile materials, the inelastic region usually develops significantly ahead of the crack tip [Elices et al., 2002; Bažant et al., 2022] (see Figure 1.1). While ductile materials follow a strain hardening regime in the inelastic region, quasi-brittle materials (e.g. rocks, concrete, ceramics, and wood) undergo a strain softening process after reaching the peak stress. This distinction originates from how energy is dissipated within the inelastic region. In ductile materials, energy is dissipated through plastic deformations, whereas in quasi-brittle materials, the progressive softening regime occurs due to a micro-damaging dissipation process within the so-called fracture process zone [Romanowicz and Seweryn, 2008; Mohammadnejad and Andrade, 2016; Manafi Farid and Fakoor, 2019; Nejati et al., 2020b; Bažant et al., 2022; Xi et al., 2022]. To model the softening behavior in the fracture process zone, a cohesive zone model pioneered by Hillerborg et al. [1976] can be utilized [Elices et al., 2002; Lecampion, 2012; Xi et al., 2022].

Although some argue that employing traction-separation laws is the only way to fully capture the physics of fracturing in quasi-brittle materials [Mohammadnejad and Andrade, 2016; Mehraban et al., 2023], our focus in the next two subsections remains on effective methods to address fracture initiation and propagation in rock-type quasi-brittle materials, while still accurately representing the fracturing behavior.

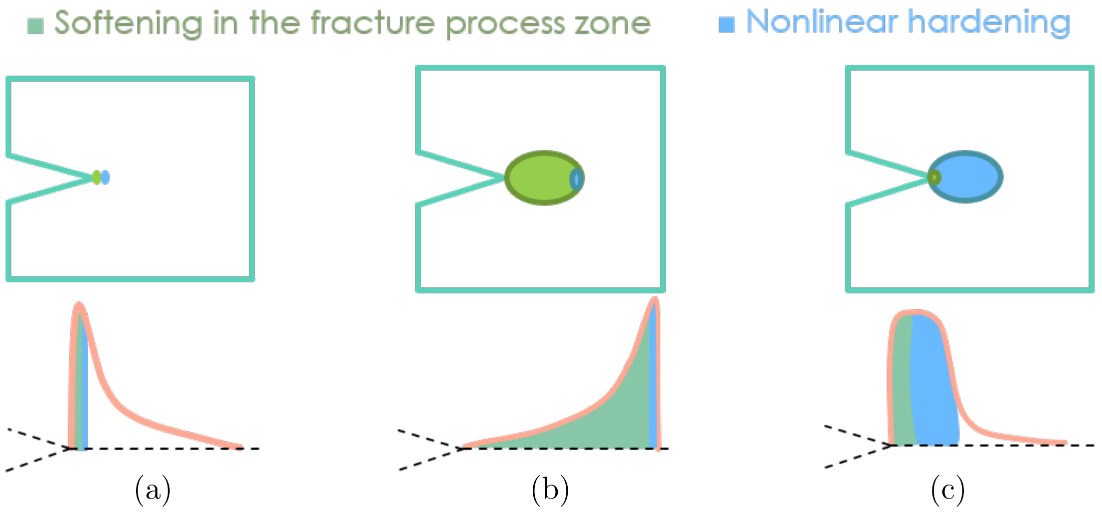

Figure 1.1: Comparing the size of nonlinear hardening and softening regions ahead of the crack tip in (a) brittle materials, (b) quasi-brittle materials, and (c) ductile materials.

1.2 Fracture initiation, finite fracture mechanics

From a physical perspective, fracture initiation in a crack-free solid can be understood as the point at which the stress distribution exceeds the tensile strength of the material, resulting in the formation of a starter crack. This concept has been widely used in numerous studies to capture fracture initiation and provide a rough estimate of the tensile loading required to overcome the material's strength [Hubbert and Willis, 1957; Haimson and Fairhurst, 1967; Ito, 2008; Zhang et al., 2017a; Gehne, 2018; Jolfaei and Lakirouhani, 2023]. However, depending on the material and structure size, this estimation may significantly underestimate the actual loading value [Lecampion, 2012]. In reality, the process is more akin to a sudden transition from a defect-free state to a cracked state with a certain length, rather than a smooth and continuous process [Cornetti et al., 2006]. The absence of length consideration in the purely strength-based criterion is the primary reason for this underestimation.

One approach to address the lack of consideration for crack length in the purely strength-based criterion is to assume an arbitrary crack length and apply the criterion to the modified configuration. However, unlike the crack-free state where robustness is well-defined, the presence of a notch creates a singularity that results in infinite stress at the crack tip. Consequently, this criterion predicts failure at a null loading [Leguillon, 2002; Cornetti et al., 2006; Lecampion, 2012], indicating that the purely strength-based criterion is inadequate for accurately describing fracture initiation. In such cases, one may opt for a purely Linear Elastic Fracture Mechanics (LEFM) approach to address fracture initiation [Atkinson and Thiercelin, 1993]. However, this approach often results in an unrealistically low failure load prediction for large defects and lacks the ability to account for size effects [Lecampion, 2012]. It should be noted that this arbitrary length is often associated with the Irwin's material lengthscale [Lecampion, 2012; Ito and Hayashi, 1991].

When the purely strength-based approach fails to capture initiation, the energy criterion can be invoked, which states that initiation occurs when the crack energy release rate exceeds a critical value. In the case of a crack-free material, the energy release approach predicts an infinite failure load due to the zero stress intensity factor [Leguillon, 2002; Cornetti et al., 2006; Lecampion, 2012; Sapora et al., 2023]. While the energy approach provides good predictions for solids with sufficiently large cracks, the purely strength-based criterion is suitable for crack-free bodies. These two ideas represent the extremes of a spectrum.

In general, fracture initiation is not adequately described by either the purely strength-based or the energy criterion alone. The intermediate case is better described when both conditions are applied [Leguillon, 2002; Cornetti et al., 2006; Lecampion, 2012; Cornetti et al., 2022; Sapora et al., 2023]. The stress field surrounding the yet-to-be-initiated crack must satisfy the strength condition, while the energy released between the cracked and crack-free states must exceed the critical energy. As a result, the potential crack instantaneously forms instead of gradually propagating, conceptualizing the formation of a finite fracture. Within the framework of finite fracture mechanics, not only the material's lengthscale but also the dimensions of the structure can influence the fracturing process [Sapora et al., 2015; Torabi et al., 2017; Doitrand and Sapora, 2020]. Lecampion [2012] illustrated that the experimental data presented by Carter et al. [1992] for hydraulic fracture initiation from different types of rock can be well reproduced by both the cohesive zone model and the mixed energy-stress criterion. This finding confirms the applicability of finite fracture mechanics to accurately capture fracture initiation in rock-type quasi-brittle materials.

1.3 Fracture propagation, LEFM and T-stress

Numerous studies in the literature have highlighted the lack of consistency among existing fracture growth criteria, especially when dealing with mixed-mode loading that drives the fracture [Gao and Chiu, 1992; Sakha et al., 2022, 2023]. However, researchers have observed that incorporating the first non-singular term in the stress-strain field, commonly referred to as the T-stress, can significantly resolve this inconsistency and enhance the predictive accuracy of fracture growth criteria [Williams and Ewing, 1984; Smith et al., 2001; Akbardoost and Ayatollahi, 2014; Ayatollahi et al., 2015; Hou et al., 2019].

To understand how the non-singular term surpasses the dominance of the singular term, it is crucial to consider the presence of a softening/hardening region preceding the crack tip in most materials. Assuming that the fracture process can still be effectively described within the framework of Linear Elastic Fracture Mechanics (LEFM), the onset of fracture growth takes place at a critical distance from the crack tip [Smith et al., 2001; Romanowicz and Seweryn, 2008; Hou et al., 2019; Bahrami et al., 2020]. This critical distance in many rock-type materials is substantial enough to diminish the dominance of the singular term, allowing the non-singular term to exert its influence [Nejati et al., 2020b].

In the case of quasi-brittle materials like rocks, this critical distance corresponds to the size of the fracture process zone [Ayatollahi and Aliha, 2006, 2008; Hou et al., 2019; Nejati et al., 2020a]. Fracture process zone, commonly known as FPZ, is an inelastic region ahead of the crack tip, where the softening regime develops in form of micro-cracking, frictional micro-slips, and grain interlock [Bažant et al., 2022]. Depending on the material type and the structure geometry, this region is a particular fraction of the material's lengthscale, connecting two essential material properties: fracture toughness and material strength [Akbardoost and Ayatollahi, 2014; Dutler et al., 2018; Bažant et al., 2022]. The size of the FPZ, however, may exhibit directional dependency in anisotropic rocks, where a higher concentration of micro-cracks is often observed along the foliation and bedding planes [Dutler et al., 2018; Nejati et al., 2020b]. Undoubtedly, a precise understanding of the fracture process zone (FPZ) is essential for accurately modeling fracture growth, especially when fractures develop in a curvilinear fashion due to the influence of loading and material complexity. Therefore, both theoretical studies [Schmidt, 1980; Bazant and Kazemi, 1990; Akbardoost and Ayatollahi, 2014] and experimental data [Chengyong et al., 1990; Zhi Kai Guo et al., 1993; Dutler et al., 2018] regarding the determination of FPZ dimensions under various configurations for different materials hold great significance within the existing literature.

1.4 Fracture modelling

The growing demand for effective fracturing in subsurface applications necessitates advanced mathematical modeling of fracture propagation in rock formations. Of particular interest in geo-engineering research is fluid-driven fracture. In addition to the complexities arising from the interaction of fluid pressure and fractures, our focus here is solely on numerical schemes capable of addressing crack discontinuities in a rock-type continuum.

The Discrete Element Method (DEM) is a widely employed numerical scheme for studying micro-fracturing in granular materials, concrete, and rocks [Fakhimi et al., 2002; Zhao and Paul Young, 2011; Yoon et al., 2014; Nejati, 2015; Yoon et al., 2015b,a]. This method considers the formation as a discontinuous medium in the micro-scale, comprising discrete particles bonded at contacts. When an individual particle moves relative to its neighbors, the contact between them is updated. In this framework, fracture growth occurs when the stress applied to the particles exceeds the strength of bonds, causing the bonds to break [Tan et al., 2009]. Despite its usefulness, the method is highly time-consuming and lacks the ability to provide detailed information about the fracture geometry.

The boundary element method (BEM) is another numerical scheme which requires the elasticity problem to be discretized only along the two fracture faces. Therefore, BEM can significantly reduce the dimensionality of the problem [Lecampion et al., 2018]. The displacement discontinuity method (DDM) is a BE-based approach which treats the two sides of a crack as a segment and describes the dislocation in the segment with the displacement discontinuity D_i [Shen et al., 2014]. The contributions of all the segments along the crack must be superposed to construct the elasticity equation of the crack. In hydraulic fracture modelling, the elasticity equation is coupled with the lubrication flow which is often descritized by either a finite element or finite volume scheme [Lecampion et al., 2018]. The efficiency of the BE-based schemes in representing hydraulic fracture propagation is well demonstrated in Siebrits and Peirce [2002]; Ke et al. [2009]; Shen and Shi [2016]; Kumar and Ghassemi [2016]; Moukhtari et al. [2019].

The finite element method (FEM) is an efficient numerical scheme when the additional coupling effects are also introduced into the conventional HM modeling (e.g. the THM simulation). The simulation of fracture propagation in the framework of the finite element method is also suitable when the domain shape is irregular, or any material heterogeneity and non-linearities are involved in the system [Lecampion et al., 2018]. The finite element scheme treats a fractured medium as a continuum. This scheme, however, can be subdivided into three conceptual models to model fractures: strong discontinuous, weak discontinuous, and continuous method. Here, these three conceptual models are distinguished.

- The strong discontinuous methods treat a fractured solid as a dislocated body and incorporate the fracture aperture to describe the jump discontinuity in the displacement field. Therefore, the geometry of the evolving fractures can be explicitly captured via two main discontinuum approaches: adaptive re-meshing, and extended/generalized finite element method (XFEM). In the adaptive re-meshing approach, the finite element mesh must fit with the fracture faces, and thus the mesh pattern is always updated during fracture growth [Eftekhari et al., 2015; Lecampion et al., 2018]. This method is computationally very demanding. A local re-meshing approach is, therefore, suggested to reduce the computation cost [Lecampion et al., 2018]. In this methodology, re-meshing is constrained to a local zone which surrounds the fracture tip and the rest of mesh is kept intact [Profit et al., 2015]. Unlike the adaptive re-meshing technique, XFEM does not require the finite element mesh to intersect the fracture surfaces at the element nodes. Instead, XFEM locally enriches the classical finite element interpolation on the elements intersected by the fracture boundary Richardson et al. [2009]. The XFEM scheme is only applicable for modeling of multiple hydraulic fractures where the fracture density is relatively low [Zeng et al., 2018].

- The weak discontinuity methods combine the strong discontiuum and continuum approaches to develop a methodology which is able to simulate sparse cracking [de Borst et al., 2004]. This behavior is strongly promoted in heterogeneous materials, such as concrete. To get a better insight into the weak discontinuous scheme, the difference between the cohesive zone models and the strong discrete schemes is first elaborated. In the strong discontinous methods, it is assumed that the fracture surfaces remain traction-free behind the physical crack tip. This approach consolidates the influence of fracturing on inelastic deformation by encapsulating it within a discrete discontinuity [Jirasek and Zimmermann, 1998]. In the cohesive zone models, however, the discontinuity develops ahead of the physical crack tip and the crack opening is therefore distributed in the fracture process zone [Moës and Belytschko, 2002]. Contrary to the traditional discrete methods, the cohesive traction is still transmitted across the discontinuum as a nonlinear function of the crack opening [Jirasek and Zimmermann, 1998]. The nonlinear fracture processes in the cohesive segment can be represented as the localized strain field if the crack opening is smeared over a band of width H. The localization band can arise at arbitrary locations, even far away from the main notch. Hence, the method is suitable to model hydraulic fracturing when the cracking pattern includes branching, bifurcation, and sparse cracking.

- The continuous methods assume that no dislocation exists in a continuum and thus the jump discontinuity across the fracture is smoothly smeared out within the damage zone. Particularly in the phase-field method, a continuous scalar variable (e.g. $0 \leq s \leq 1$) is introduced to form the failure region and describe the smooth transition from the fully broken zone (i.e. $s = 0$) to the intact region (i.e. $s = 1$) [Lecampion et al., 2018]. Indeed, the energy released over the failure region is translated to the deterioration of the material stiffness [Wu et al., 2020a]. This approach cannot explicitly track the fracture aperture, and thus estimating the fracture aperture remains a challenge in the HM modeling [Bourdin et al., 2012; Lecampion et al., 2018]. Nevertheless, this method can fully determine the fracture path through a fixed mesh, even if fracturing entails complex behaviors such as bifurcation, branching, and kinking. Hence, the phase-field method has become increasingly popular in modeling of hydraulic fracturing in recent decades [Bourdin et al., 2012; Chukwudozie et al., 2013; Wheeler et al., 2014; Chukwudozie et al., 2019].

1.5 Fracturing within subsurface

Unlike many engineering applications where fracture is primarily driven by in-situ tensile loading, subsurface fracture mechanisms are predominantly controlled by compressive stresses in the far-field. This inconsistency has led to controversy not only in the definition of the convention of positive stresses but also in the necessity to decompose the contribution of different modes of fracturing.

One well-known example in the field of geo-engineering involves an inclined central crack subjected to increasing uniaxial compressive loading [Ingraffea and Heuze, 1980; Shen and Stephansson, 1994; Zhang et al., 2017b]. This particular example holds significant importance, not only due to its high likelihood within subsurface environments but also because the propagation of natural pre-existing fractures under compressive in-situ loading can lead to unstable sliding fracturing [Ingraffea and Heuze, 1980; Zhang et al., 2017b].

Under such loading conditions, a distinct pattern of fracturing emerges. Initially, a tensile fracture, or so-called a wing crack, develops along a direction approximately 90° away from the original inclined crack. This wing crack gradually, yet stably, reorients itself towards the direction of maximum compressive loading. In rock-like materials, the fracturing process is further characterized by the occurrence of a secondary fracture that grows parallel to the original inclined fracture. This secondary fracture involves the sliding of the in-contact surfaces against each other, resembling a shearing failure [Ingraffea and Heuze, 1980; Shen and Stephansson, 1994; Bobet and Einstein, 1998; Wong and Einstein, 2009; Zhang et al., 2017b; Wu et al., 2020a]. Hence, it is of special importance to establish a comprehensive fracture propagation model, capable to effectively capture this initial stable tensile fracture followed by the subsequent relatively-unstable shearing fracture.

Even in phase-field modeling, which is often considered a robust fracture modeling technique capable of handling complex loading conditions without any additional criterion, studies focusing on rock fracture under far-field compressive loading have demonstrated that the phase-field method can capture the formation of wing cracks followed by secondary cracks, provided that the elastic energy density can effectively distinguish between shearing and tensile fracturing [Zhang et al., 2017b; Bryant and Sun, 2018]. However, this approach may not be supported from a variational perspective [Zhuang et al., 2022], as the decomposition of shearing and opening is applicable only to the strong form of governing equations and cannot be extended to the energy functional governing the fracturing process. Hence, the capability of well-known phase-field fracture models to accurately describe fracturing under compression should be further investigated.

Compressive in-situ stresses within the subsurface often exhibit stress anisotropy, meaning that the horizontal compressive stresses may not be equal to the vertical in-situ stress. This deviation, or stress anisotropy, significantly influences the fracturing mechanisms in the subsurface [Fu et al., 2013; Valliappan et al., 2019; Dong and Tang, 2019]. For instance, stress anisotropy can enhance failure in cases of shear-reactivation.

When it comes to hydraulic fracture initiation, higher deviatoric stress can make initiation more dependent on the material's lengthscale, structure size, particularly when Irwin's material lengthscale is significantly larger than the structure lengthscale [Lecampion, 2012]. In the context of fracture propagation in initially perforated wellbores, it has been observed that the degree of reorientation of hydraulic fractures, known as tortuosity, is strongly influenced by stress anisotropy [Dong and Tang, 2019; Xi et al., 2022]. However, it is worth noting that most studies have been conducted under the assumption of isotropic behavior of the rock mass, and further research is needed to understand the influence of stress anisotropy on fracture initiation and propagation, especially in scenarios where other factors, such as material anisotropy are present.

1.6 Thesis outline

The primary objective of this thesis is to investigate the influence of material anisotropy on fracture initiation and propagation in rock formations within the subsurface. In doing so, we undertake three key steps in order to establish reliable theories and models that can accurately predict the behavior of hydraulic fracture initiation and propagation in anisotropic rock formations.

Firstly, we focus on developing theories and models capable of capturing the kinking behavior observed in anisotropic materials, where the fracture path is not a priori assumption. An accurate theory can effectively capture fracture propagation regardless of the complexity of the loading conditions ahead of the initial crack. This entails the model's ability to identify complex compressive loading zones ahead of the crack, preventing the crack from being driven solely by compression, thereby avoiding crack kinking toward such regions. Additionally, the model may need to distinguish between the contributions of tensile and shearing forces along the direction of the fracture path, as the dominance of the tensile force driving the fracture may diminish under complex loading conditions, giving rise to shearing forces that do not drive tensile fractures.

Secondly, we strive to apply a model suitable for hydraulic fracture initiation in an initially notch-free wellbore, that can understand fracture initiation as an instantaneous process, where a finite crack forms suddenly rather than gradually grows. This model must encompass the influences of material anisotropy, in-situ stress anisotropy, and the size of the material and structure to capture hydraulic fracture initiation as it occurs in reality.

Lastly, by integrating these models, we can comprehensively understand how material anisotropy interacts with other contributing factors to propagate and initiate fractures within the subsurface. In this study, we exclusively assume rock anisotropy as a transversely isotropic material, wherein the ratio of two principal Young's moduli, along with the orientation of the isotropy plane relative to the fracture orientation, are the key aspects of the rock's anisotropic behavior. By targeting each of these two characteristics, we aim to investigate their influence on fracture behavior and provide insights into the complex mechanics governing fracture propagation and initiation in anisotropic rock formations.

The structure of this thesis is as follows: In Chapter 2, we evaluate the accuracy of most notable fracture growth criteria in predicting crack paths in anisotropic rocks under mixed-mode I/II loading. This evaluation is accomplished by comparing the theories with a set of reliable experimental data. We demonstrate that the classical formulation of energy-based criteria results in inaccurate predictions of fracture trajectory. To address this inaccuracy, we propose a modification to the energy-based criteria and compare the performance with the experimental data. Through reassessment with the experimental data, we observe a good agreement between the results, indicating the significance of modifying energy-based theories when complex loading regimes exist ahead of the crack in many rock-type materials with moderate to high disparities in mode I and mode II fracture toughnesses. In Chapter 3, we employ a mixed criterion to investigate hydraulic fracture initiation in anisotropic rocks, considering the influence of both material and loading anisotropy on the geometry of the starter crack and the initiation pressure. Analytical relations of the corrective stresses and the kernel matrix, along with the displacement discontinuity method are implemented in this chapter. Due to a lack of experimental tests for validation purposes, we utilize finite element modeling to reproduce the initiation parameters observed in Chapter 3. Therefore, C.1 complements Chapter 3 by employing a different approach for studying hydraulic fracture initiation in anisotropic rocks.

In Chapter 4, we employ the phase-field model to predict fracture trajectories in anisotropic rocks, as experimentally tested in the first step of this thesis. Given the likelihood of interpenetration due to compression, we apply a decomposition technique from the existing literature to the model. We assess the reliability of its implementation and the robustness of the decomposition through comparison with numerical studies in the literature and experimental tests, respectively. Finally, Chapter 5 concludes the thesis by providing the main findings and discussing potential areas for future research work. Additionally, the thesis includes three appendices that present the analytical relations used in this study, providing additional reference for the readers.

Chapter 2

On the validation of mixed-mode I/II crack growth theories for anisotropic rocks

M. Sakha[a], M. Nejati[a], A. Aminzadeh[a], S. Ghouli[b], M. O.Saar [c,d], T. Driesner[a]

[a] *Department of Earth Sciences, ETH Zurich, Switzerland*
[b] *School of Mechanical Engineering, Iran University of Science and Technology, Tehran, Iran*
[c] *Geothermal Energy and Geofluids Group, Department of Earth Sciences, ETH Zurich, Switzerland*
[c] *Department of Earth and Environmental Sciences, University of Minnesota, Minneapolis, USA*

2022, Published in *International Journal of Solids and Structures*, 241.

2.1 Abstract

We evaluate the accuracy of three well-known fracture growth theories to predict crack trajectories in anisotropic rocks through comparison with new experimental data. The results of 99 fracture toughness tests on the metamorphic Grimsel Granite under four different ratios of mixed-mode I/II loadings are reported. For each ratio, the influence of the anisotropy orientation on the direction of fracture growth is also analyzed. Our results show that for certain loading configurations, the anisotropy offsets the loading influence in determining the direction of crack growth, whereas in other configurations, these factors reinforce each other. To evaluate the accuracy of the fracture growth theories, we compare the experiment results for the kink angle and the effective fracture toughness with the predictions of the maximum tangential stress (MTS), the maximum energy release rate (MERR), and the maximum strain energy density (MSED) criteria. The criteria are first assessed in their classical forms employed in the literature. It is demonstrated that the energy-based criteria in their classical formulation cannot yield good predictions. We then present modified forms of the ERR and SED functions in which the tensile and shear components are decomposed. These modified forms give significantly better predictions of fracture growth paths. The evaluation of the three criteria illustrates that the modified MSED criterion is the least accurate model even in the modified form, while the results predicted by MTS and modified MERR are well matched with the experimental results.

2.2 Introduction

As an intrinsic property of geomaterials, anisotropy plays an important role in governing the mechanics of fracture growth in rocks, relevant for applications in geomechanics and geophysics. Rock anisotropy is known to be the result of the preferred orientation of micro-cracks and anisotropic constituent minerals. For example, mechanically weak, platy mica grains are dominantly oriented along foliation in metamorphic rocks, or clay minerals are aligned with bedding planes in sedimentary rocks. The analysis of fracture growth in these types of rocks has direct applications in many industries such as oil and gas shale, carbon sequestration, enhanced geothermal systems, tunneling and mining. For example, hydraulic fracturing is employed in enhanced geothermal systems in order to increase permeability in the host rock, which often consists of anisotropic metagranite or gneiss. The stress perturbation due to the injection of pressurized fluid can cause the creation of new fractures, the growth of pre-existing fractures, and/or the shear-activation of faults and fractures with associated earthquakes, which raises concerns regarding the safety of these processes [Amann et al., 2018; Berryman, 2016]. In-situ experiments conducted in the deep underground laboratory at the Grimsel test site in Switzerland have recently demonstrated that the anisotropy of the rock mass should be taken into account when analyzing fracture growth patterns [Gischig et al., 2018].

Figure 2.1a schematically shows how anisotropy can influence the mechanics of hydraulic fracturing near a borehole in a reservoir. In addition to the creation of new fractures, the injected fluid can induce growth in pre-existing fractures and/or result in their shear activation (hydro-shearing). Although large-scale hydraulic fractures tend to propagate normal to the direction of minimum in-situ stress (i.e. a pure mode I crack growth), their propagation in the vicinity of a borehole is often associated with a mixed-mode I/II/III loading condition. We note that, based on the geo-mechanics convention, the in-situ stresses are taken as positive values here. For example, when the borehole is situated obliquely with respect to the principal stresses, the presence of the complex stress regime near the borehole may lead to the formation and/or growth of mixed-mode fractures. Even in boreholes that align with one principal in-situ stress direction, strength anisotropy can cause the hydraulic-fractures to initiate and grow in an oblique direction with respect to the principal stresses, hence inducing mixed-mode fracture growth. Such fractures then turn and twist in complex geometrical patterns to eventually be oriented in a direction that is normal to the minimum in-situ stress at larger scales [Moukhtari et al., 2020].

Generally, the angle of fracture growth depends on geometry, loading, and material anisotropy. Assuming a fixed geometry, loading and anisotropy remain the major influences on the fracture growth trajectory in an anisotropic solid. While, in some configurations, loading and anisotropy reinforce each other in driving the fracture growth in a certain direction, in other configurations they may compete with each other in determining the direction of crack growth. This concept is schematically shown in Figure 2.1b, where the mode-mixity parameter, defined as $\lambda = K_{\mathrm{II}}/(K_{\mathrm{I}}^2 + K_{\mathrm{II}}^2)^{1/2}$, and the anisotropy direction, β, characterize how loading and anisotropy interact. Here, K_{I} and K_{II} are respectively mode I and mode II stress intensity factors. The material is also assumed to have higher tensile strength along direction 1, meaning that the material is more resistant to failure along direction 2. We assume that the principal directions 1 aligns with the material's isotropy plane (bedding or foliation). In the case of $\lambda < 0$, loading and anisotropy reinforce each other, both promoting positive kink angles ($\theta_0 > 0$). In the case of $\lambda > 0$, however, while anisotropy facilitates growth along $\theta_0 > 0$, due to the lower tensile strength, the loading promotes kinks with $\theta_0 < 0$. In this case, anisotropy and loading compete to determine the direction of fracture growth. We note that this interaction of loading and anisotropy is significant only in materials that have low to moderate

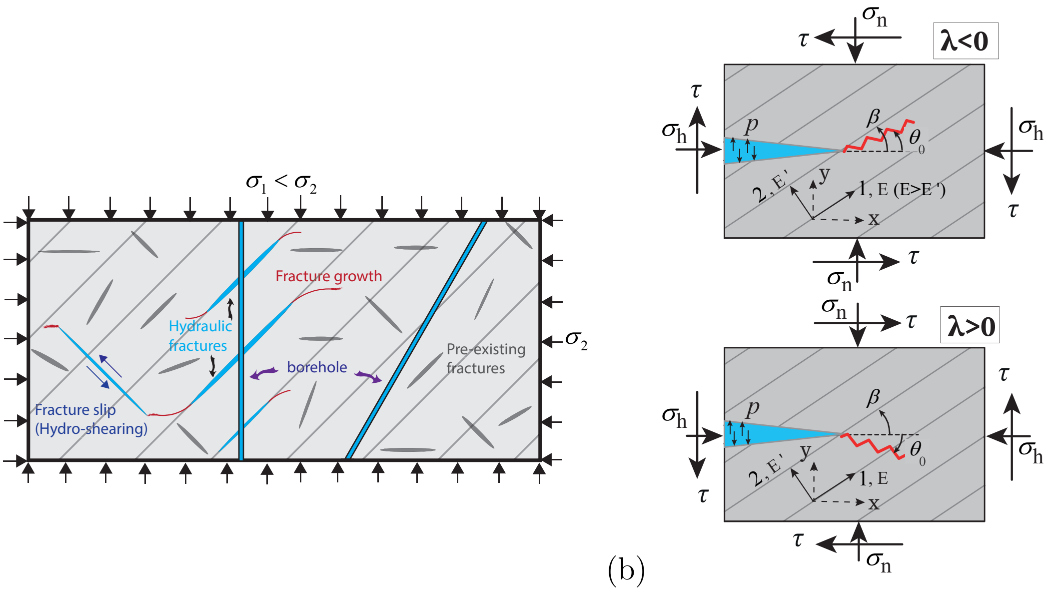

(a) (b)

Figure 2.1: (a) Schematic view of hydraulic fracturing around boreholes in the presence of mixed-mode I/II loading; The parallel lines show the isotropy plane (bedding or foliation) in transversely isotropic rocks. Here, a compressive stress is represented with a positive value. (b) Schematic illustration of the interaction of loading and anisotropy based on the sign of the mode-mixity parameter $\lambda = K_{\text{II}}/(K_{\text{I}}^2 + K_{\text{II}}^2)^{1/2}$. The principal axes 1 and 2 respectively denote the strong and weak directions of the material.

anisotropy ratios such as many rocks. In highly anisotropic materials such as wood and some engineering composites, the effect of anisotropy is much stronger than that of loading, thereby causing the crack extension to almost always occur along the weakest planes of the material, i.e. the fibers [Jernkvist, 2001; Cahill et al., 2014].

In order to predict the fracture growth trajectory in anisotropic solids, an accurate fracture growth criterion must be employed to describe failure at the crack tip based on the state of stress and deformation. Sih et al. [1965] first introduced the solution of crack tip fields in anisotropic media. Thereafter, the most notable isotropic fracture growth criteria were extended to those applicable to anisotropic solids. These include the maximum tangential stress (MTS, Saouma et al. [1987]; Buczek and Herakovich [1985]; Lim et al. [2001]; Carloni and Nobile [2005]), maximum energy release rate (MERR, Obata et al. [1989]; Gao and Chiu [1992]; Azhdari and Nemat-Nasser [1996]; Yang and Yuan [2000]; Argatov and Nazarov [2002]), and maximum (minimum in isotropic materials) strain energy density (MSED, Zhang et al. [1989]; Ye and Ayari [1994]; Carloni and Nobile [2002]; Manafi Farid and Fakoor [2019]). These studies merely focused on the formulation and characteristics of different theoretical models, and, importantly, lack evaluations of the accuracy of models using experimental data. Inconsistencies between the results of different theoretical models on crack path geometries, highlighted by Gao and Chiu [1992]; Azhdari and Nemat-Nasser [1996, 1998], also add to the uncertainties regarding the accuracy of these theoretical predictions.

A literature survey reveals several studies that compared the results of different theoretical models with experimental data (Table 2.1). Some of these studies included the effects of the first non-singular term, T-stress, while others only considered the singular terms. We point out here that in highly anisotropic materials, such as wood and engineering composites, cracks tend to grow along the fiber direction [Cahill et al., 2014; Romanowicz, 2019; Manafi Farid and Fakoor, 2019; Fakoor and Khezri, 2020]. In such cases, the fracture path is often an *a priori* assumption, used in the growth criteria. In materials with a moderate anisotropy ratio such as rocks, however, the fracture path is unknown and must be estimated along with the critical fracture load. Thus, the performance of a theoretical model must be evaluated based on its predictions in moderate anisotropic solids, where the crack growth direction is the outcome of the interaction of both loading and anisotropy. In this framework, it is evident that most of these research articles focused on only one growth criterion, and lack a comparison of the performance of different models. This highlights the limited knowledge regarding the performance and accuracy of different growth criteria in anisotropic solids, and, in particular, in rock-type materials. To the best of our knowledge, the literature lacks a rigorous validation study that compares the performance of all three criteria using one comprehensive experimental data set.

Loading	Material	Employed criteria	References
Mode I	Composite	MTS, MERR	Judt et al. [2019]
Mode I	Rock	MTS (T-stress inclusion), MERR, MSED	Nejati et al. [2020a]
Mixed-mode I/II	Rock	MTS	Chen et al. [1998]
Mixed-mode I/II	Crystal	MTS, MERR	Azhdari and Nemat-Nasser [1998]
Mixed-mode I/II	Composite	MTS	Motamedi and Mohammadi [2010]
Mixed-mode I/II	Composite	MTS	Cahill et al. [2014]
Mixed-mode I/II	Rock	MTS (T-stress inclusion)	Mohtarami et al. [2017]
Mixed-mode I/II	Wood	MTS (T-stress inclusion)	Romanowicz [2019]
Mixed-mode I/II	Wood	MSED (T-stress inclusion)	Manafi Farid and Fakoor [2019]
Mixed-mode I/II	Wood	MSED	Fakoor and Khezri [2020]
Mixed-mode I/II	Rock	MTS	Wang et al. [2020]
Mixed-mode I/II/III	Foam	MTS	Arakere et al. [2008]

Table 2.1: A list of studies that evaluated three well-know fracture growth criteria in anisotropic materials using experimental data.

According to Table 2.1, MTS is by far the most widely used criterion for predicting fracture growth in anisotropic solids. This is perhaps due to the mathematical simplicity of the criterion, and also its accurate predictions for the kink angle. Most studies reported that MTS predictions match experimental data well. In contrast, limited studies on the MERR criterion show inconsistent conclusions. For example, while Judt et al. [2019] observed a good agreement between the experimental data and the MERR predictions, Azhdari and Nemat-Nasser [1998] reported inconsistencies between the MERR predictions and the observed crack deflections. Based on test results on a crystal, Azhdari and Nemat-Nasser [1998] concluded that the MTS yields better predictions on fracture path geometries than the MERR criterion. Similarly, the evaluation of the MSED criterion also revealed some inconsistencies. While Nejati et al. [2020a] concluded that the MSED fails to provide good predictions on fracture path geometry, Manafi Farid and Fakoor [2019] reported good agreements between the MSED predictions and the experimental data. One, however, should note that Manafi Farid and Fakoor [2019] used *a priori* assumptions on kink angle (along the wood fiber), and did not employ the MSED criterion to predict the crack path direction. In conclusion, while most studies indicate good predictions of the MTS criterion, the reports on the MERR and MSED criteria are rather inconsistent.

In order to quantitatively assess mixed-mode I/II fracture growth criteria in rocks, a comprehensive set of experimental data is required. To obtain such a data set, (1) controlled experiments must be designed and conducted at different mode-mixity parameters, $-1 < \lambda < 1$. Such a setup must also be able to keep the mode-mixity ratio, λ, constant while the anisotropy orientation varies. To achieve this, we employ an asymmetrical semi-circular bend (SCB) test, proposed by Nejati et al. [2019a] and used in Nejati et al. [2020a] for pure mode I tests. This test setup allows us to use the exact same sample geometry to conduct different sets of tests, each with a fixed λ but different anisotropy orientations. (2) A well-characterized rock must be used for the tests, as the material parameters, such as elastic constants, fracture toughness, and the size of the fracture process zone, are directly employed in the formulation of the growth criteria to predict the fracture growth trajectory. We conduct tests on anisotropic Grimsel Granite samples, a rock that has been extensively studied in terms elastic constants [Nejati et al., 2019b; Dambly et al., 2019], fracture toughness variation [Nejati et al., 2020b, 2021a], and the size of the fracture process zone [Dutler et al., 2018; Nejati et al., 2021a]. Using such well-characterized rocks significantly reduces uncertainties in parameters that are directly implemented in the formulations for fracture growth.

In this paper, we present the results of four sets of fracture growth tests on the anisotropic Grimsel Granite under four different ratios of mixed mode I/II loadings: $\lambda = -0.37,\ 0.37, -0.71,$
0.71. Keeping λ constant in each set allows the evaluation of the influence of the anisotropy direction, β, on the fracture path. We then evaluate the accuracy of the three major fracture growth criteria proposed for brittle materials, namely the MTS, MERR, and the MSED. In doing so, the fracture growth criteria are first formulated based on the classical forms available in the literature. The comparison between the theoretical predictions and the experimental data reveals that the energy-based criteria (i.e. MERR and MSED) are unable to properly describe the fracture growth behavior. We therefore introduce modified versions of the energy-based theories and re-assess their predictions with the experiments. The improvement in the results shows that the proposed modifications to the energy-based criteria are essential to yield reasonable predictions. According to the comparison of the theoretical predictions with experimental data, we can conclude that:

- The suggested modified version of MERR predicts the experimental data much better compared to the classical version that is commonly used in the literature.
- The MSED criterion, even in its modified form, is the least accurate criterion to

predict the fracture growth trajectory.

- Both MTS and the modified version of the MERR give equally accurate predictions for the kink angle and effective fracture toughness.

This paper is structured as follows: Section 2 discusses the experimental setup for collecting mixed-mode I/II fracture growth data. Section 3 describes the formulations of the three criteria as they are currently presented in the literature. Section 4 compares the results of these theoretical models with the experimental data, concluding that the energy-based criteria do not perform well in the prediction of growth path. Section 5 presents modified versions of the energy-based criteria, and shows that these modifications yield significantly more accurate predictions. Finally, Section 6 presents a discussion of each of the growth theories, and Section 7 presents the concluding remarks.

2.3 Experimental setup

2.3.1 Material

Samples of Grimsel Granite were used in this research in order to conduct mixed-mode I/II fracturing tests. These samples were obtained from one drill core extracted from the injection boreholes used in the In-situ Stimulation and Circulation (ISC) experiment conducted in the Grimsel Test Site (GTS) in the central Alps of Switzerland (see Amann et al. [2018]; Gischig et al. [2018] for details). This underground laboratory is located in the granitic formations of the Aare massif at a depth of about 450 m underneath the *Juchlistock* [Gischig et al., 2020]. The Grimsel Granite was metamorphosed during the Alpine deformation, causing a reorientation of sheet silicates and forming a pervasive foliation that is clearly visible in the samples. Dambly et al. [2019] showed that the Grimsel Granite exhibits transversely isotropic behavior, with the isotropy plane coinciding with the foliation plane. Therefore, the foliation plane (direction 1) and the plane normal to it (direction 2) represent two principal material directions. Table 2.2 lists the elastic properties of the Grimsel Granite, obtained from Brazilian disk tests [Dutler et al., 2018]. These values are comparable to the ones obtained from uniaxial compression tests [Nejati et al., 2019b]. E and E' are the Young's moduli along (direction 1) and normal (direction 2) to the foliation plane, ν and ν' are the Poisson's ratios within and normal to the foliation plane, respectively, and G' is the transverse shear modulus. The parameters $\xi, \eta, \kappa_1, \kappa_2, \kappa_3$ are related to the elastic constants through the definition given in A.1.

Elastic properties										Fracture toughness properties				
E	E'	ν	ν'	G'	ξ	η	κ_1	κ_2	κ_3	$K_{\mathrm{Ic},1}$	$K_{\mathrm{Ic},2}$	$K_{\mathrm{IIc},1}$	$K_{\mathrm{IIc},2}$	L_c
36	18	0.3	0.15	10	2	1	0.91	0.96	1.3	0.78	1.35	1.90	2.88	10

Table 2.2: The elastic properties and fracture toughness values measured for Grimsel Granite. $\kappa_1, \kappa_2, \kappa_3$ are reported for plane-strain conditions. The elastic moduli and fracture toughness are given in GPa and MPa$\sqrt{\mathrm{m}}$, respectively, and the FPZ length is given in mm.

As important parameters, the principal values of the fracture toughness of Grimsel Granite are also listed in Table 2.2. The details of the measurement procedure of these parameters are given in Nejati et al. [2021a]. $K_{\mathrm{Ic},1}$ and $K_{\mathrm{Ic},2}$ are, respectively, the mode I fracture toughness values in the principal directions 1 (along the foliation) and 2 (normal to the foliation) (see Figure 2.2a). Nejati et al. [2020b] showed via experimental data that $K_{\mathrm{Ic}}(\phi)$ follows a sinusoidal fit of the principal values (see Figure 2.2c). Here, ϕ is the direction of fracture growth with respect to the principal direction 1. In addition to K_{Ic}, which represents the resistance of a material against tensile fracturing, the shearing fracture toughness, also referred to as the true mode II fracture toughness (K_{IIc}), is of significant importance in rock fracturing [Bahrami et al., 2020]. K_{IIc} represents the material resistance against a co-planar extension of a mode II crack, as shown in Figure 2.2b. Table 2.2 presents the values of $K_{\mathrm{IIc},1}$ and $K_{\mathrm{IIc},2}$ that are, respectively, the principal values of true mode II fracture toughness along principal directions 1 and 2 (see Figure 2.2b). Similar to mode I, an experimental study by Nejati et al. [2021a] showed that $K_{\mathrm{IIc}}(\phi)$ also follows a sinusoidal variation between the two principal planes (see Figure 2.2c). Lastly, Table 2.2 presents the length of the fracture process zone, L_c, in the SCB samples of the Grimsel Granite. This value was obtained in an independent study using the digital image correlation technique [Dutler et al., 2018]. Nejati et al. [2021a] showed that the length of the fracture process zone during the true mode II fracturing mechanism is similar to the one during mode I fracturing.

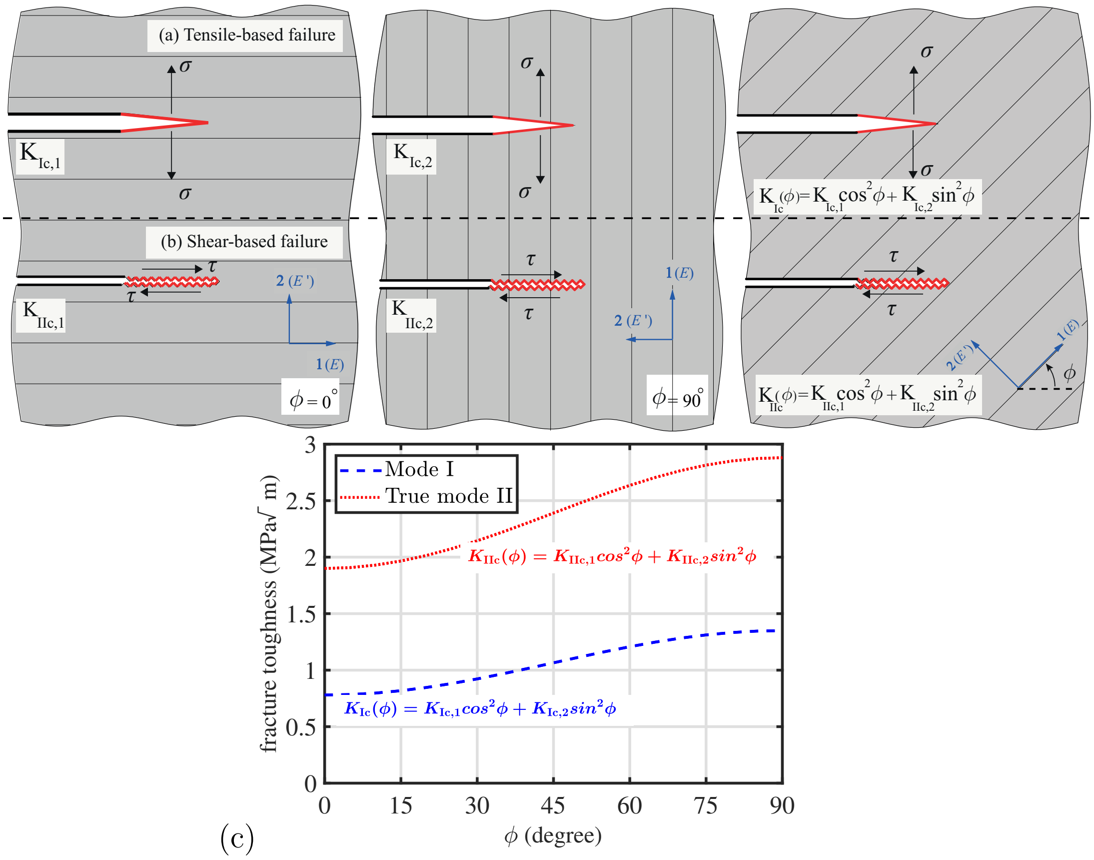

Figure 2.2: Schematic illustration of the principal values of (a) mode I and (b) true mode II fracture toughness and their variations with direction in an anisotropic material; (c) variations of the fracture toughness associated with mode I and true mode II in Grimsel Granite.

When using the MERR or MSED criteria, one needs knowledge of the direction dependency of the critical mode I and true mode II energy release rates, also referred to as fracture energy, (i.e. $\mathcal{G}_{\mathrm{Ic}}(\phi)$ and $\mathcal{G}_{\mathrm{IIc}}(\phi)$), and the critical strain energy density, $\mathcal{S}_{\mathrm{Ic}}(\phi)$. Direction-dependent fracture energy is also an important input parameter used for phase-field modeling of fracture growth [Rezaei et al., 2021]. The MERR criterion considers the energy release rate as the driving force that overcomes the critical energy release rate, $\mathcal{G}_{\mathrm{c}}$, at the onset of crack growth [Hussain et al., 1974]. In MSED, the strain energy density acts as the diving force and triggers fracturing once it reaches the critical strain energy density, $\mathcal{S}_{\mathrm{c}}/r$ [Sih, 1973]. Irrespective of the mode of failure, all these measures are determined for a crack that propagates in a co-planar manner. Using linear elasticity theory, Nejati et al. [2020b, 2021a] introduced simple functions that govern the directional dependencies of $\mathcal{G}_{\mathrm{Ic}}$, $\mathcal{G}_{\mathrm{IIc}}$, and $\mathcal{S}_{\mathrm{Ic}}$ in anisotropic solids (see Table 2.3). When deriving these functions, the parameter η, defined in Eq. (A.1.4), is assumed to be equal to unity, denoting that the transverse shear modulus follows the Saint-Venant relation. Nejati et al. [2019a] showed that this is a good approximation for many anisotropic rock types. The above summarized comprehensive experimental and theoretical characterizations make Grimsel Granite probably the currently best-characterized material to assess the performance of fracture growth criteria in anisotropic rocks.

	Measure of Fracture Toughness	Variation against ϕ
Tensile-based failure	Critical SIF-K_{Ic}	$K_{\mathrm{Ic}}(\phi) = K_{\mathrm{Ic},1}\cos^2\phi + K_{\mathrm{Ic},2}\sin^2\phi$
	Critical ERR-$\mathcal{G}_{\mathrm{Ic}}$	$\mathcal{G}_{\mathrm{Ic}}(\phi) = \dfrac{K_{\mathrm{Ic}}^2(\phi)}{2E}\left(\kappa_2\left(\xi+\sqrt{\xi}\right)\cos^2\phi + \kappa_1\left(\sqrt{\xi}+1\right)\sin^2\phi\right)$
	Critical SED-$\mathcal{S}_{\mathrm{Ic}}$	$\mathcal{S}_{\mathrm{Ic}}(\phi) = \dfrac{K_{\mathrm{Ic}}^2(\phi)}{4\pi E}\left(\xi\cos^2\phi + \sin^2\phi + \dfrac{\xi(\kappa_1+\kappa_2-1-2\kappa_3\nu'\sqrt{\xi})}{\cos^2\phi+\xi\sin^2\phi}\right)$
Shear-based failure	Critical SIF-K_{IIc}	$K_{\mathrm{IIc}}(\phi) = K_{\mathrm{IIc},1}\cos^2\phi + K_{\mathrm{IIc},2}\sin^2\phi$
	Critical ERR-$\mathcal{G}_{\mathrm{IIc}}$	$\mathcal{G}_{\mathrm{IIc}}(\phi) = \dfrac{K_{\mathrm{IIc}}^2(\phi)}{2E}\left(\kappa_1\left(\sqrt{\xi}+1\right)\cos^2\phi + \kappa_2\left(\xi+\sqrt{\xi}\right)\sin^2\phi\right)$

Table 2.3: The directional dependence of the different measures of fracture toughness in tensile- and shear-based failure mechanisms, adopted from Nejati et al. [2020b, 2021a]. Here, $\xi = E/E'$ is the anisotropy ratio of Young's modulus, $\kappa_1 = \kappa_2 = \kappa_3 = 1$ for the plane-stress condition and $\kappa_1 = 1-\nu^2$, $\kappa_2 = 1-\xi\nu'^2$, $\kappa_3 = 1+\nu$ for the plane-strain condition.

2.3.2 Tests

The asymmetrical semi-circular bend (SCB) test configuration in Figure 2.3 was employed in this study to conduct mixed-mode fracturing tests. This test configuration enables obtaining different combinations of mixed-mode I/II loading simply by varying the span ratio, S_2/S_1. This test was proposed by Ayatollahi et al. [2011] for mixed-mode fracturing tests of isotropic rocks. Nejati et al. [2019a] later employed this test to configure a pure mode I fracturing test for anisotropic rocks. The asymmetrical SCB test enables obtaining both positive and negative values of mode-mixity parameter, λ, by adopting different span ratios, S_2/S_1. While fixing $S_1/R = 0.8$, the ratio S_2/S_1 was calculated, via finite element analyses in ABAQUS, in such a way that the mode-mixity of interest (λ) is achieved. For a fixed λ, the span ratio, S_2/S_1, depends on ξ, η, and β. More details can be found in Nejati et al. [2019a].

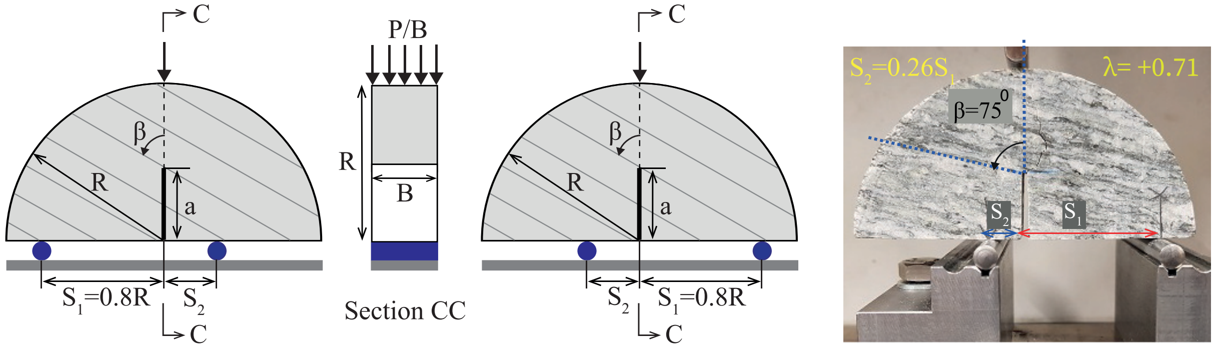

(a)

(b)

(c)

Figure 2.3: Schematics of the SCB test setup for (a) $\lambda < 0$ and (b) $\lambda > 0$; (c) a tested sample of Grimsel Granite with the configuration $\lambda = +0.71$ and $\beta = 75°$.

We conducted four sets of tests on Grimsel Granite samples that were prepared via sub-coring in the direction of the foliation plane. Each set of tests contains samples with seven different foliation angles (direction 1) with the original notch planes ($\beta = 0°, 15°, 30°, 45°, 60°, 75°, 90°$) subjected to a load with a fixed mode-mixity parameter, $\lambda = K_{\mathrm{II}}/K_{\mathrm{eff}}$, where the effective stress intensity factor K_{eff} is defined as $K_{\mathrm{eff}} = (K_{\mathrm{I}}^2 + K_{\mathrm{II}}^2)^{1/2}$. Table 2.4 lists the geometry and loading details in all sets of experiments. We tested the samples at a displacement rate of 0.1 mm/min, using a Zwick/Roell 1474 RetroLine universal testing machine with a load capacity of 100 kN, and a load resolution of 10 N.

Set Name	Number of Tests	$B/2R$	a/R	β (°)	$K_{\mathrm{II}}/K_{\mathrm{I}}$	λ
Set I	18	0.39-0.45	0.40-0.44	0, 15, 30, 45, 60, 75, 90	-0.4	-0.37
Set II	19	0.35-0.47	"	"	0.4	0.37
Set III	30	0.38-0.44	"	"	-1	-0.71
Set IV	32	0.37-0.46	"	"	1	0.71

Table 2.4: Geometry and loading details of the SCB tests for different experiment sets conducted on Grimsel Granite ($R = 47.5$ mm).

The crack tip parameters, including K_{I} and K_{II} and T-stress were calculated using the finite element method. The SCB specimen was modeled in the finite element software ABAQUS, where K_{I} and K_{II} were determined using the domain integral method for the test configurations given in Table 2.4. In addition, the values of T-stress were determined using the finite element over-deterministic (FEOD) method [Ayatollahi et al., 2020]. In fracture growth criteria, T-stress appears in a dimensionless form of $\bar{T} = T\sqrt{2\pi L_{\mathrm{c}}}/K_{\mathrm{eff}}$. Table 2.5 provides the values calculated for $\bar{T}$ in all the test configurations. After conducting the tests, the kink angles on both sides of the samples were determined by measuring the angle between the crack path within the process zone and the notch plane. The average of the kink angles at the two sides of each sample is reported as the kink angle, θ_0. The effective fracture toughness is also calculated by inserting the stress intensity factors at peak load in $K_{\mathrm{eff}}^{c} = (K_{\mathrm{If}}^2 + K_{\mathrm{IIf}}^2)^{1/2}$, where K_{If} and K_{IIf} respectively represent the critical values of stress intensity factors at the onset of fracturing.

	β (°)						
	0	15	30	45	60	75	90
Set I	-0.89	-1.01	-1.02	-0.96	-0.87	-0.78	-0.71
Set II	-0.90	-0.76	-0.64	-0.59	-0.60	-0.65	-0.72
Set III	-1.99	-2.13	-2.00	-1.88	-1.73	-1.59	-1.54
Set IV	-2.05	-1.85	-1.70	-1.58	-1.51	-1.51	-1.49

Table 2.5: Calculated values of the dimensionless T-stress, $\bar{T}$, for the four sets of experiments at different angles of β.

2.4 Fracture growth criteria

Three main criteria have been suggested to predict the direction of fracture growth in general solids: maximum tangential stress (MTS), maximum energy release rate (MERR), and maximum strain energy density (MSED). Although these criteria yield similar predictions in isotropic materials, they tend to give contradictory predictions in anisotropic solids (see for example the discussions in Gao and Chiu [1992]; Azhdari and Nemat-Nasser [1998]; Nejati et al. [2020a]). This section reviews the mathematical formulation of these three criteria in an anisotropic plane subjected to mixed-mode I/II loading, as they are presented and used in the literature. In order to formulate these criteria, the first two terms of the crack tip fields, i.e. the singular terms together with the T-stress term, are considered. The full series representation of the crack tip fields in an anisotropic plane is given in detail in Ghouli et al. [2020]; Nejati et al. [2021c], while a brief description of the fields, containing the first two terms only, is given in A.1.

2.4.1 Maximum tangential stress (MTS)

Originally proposed by Erdogan and Sih [1963], the MTS criterion postulates that a crack propagates in a radial direction at which the tangential stress reaches its critical value which is associated with the tensile strength of the material. Williams and Ewing [1984]; Smith et al. [2001] later showed that the T-stress inclusion in the MTS formulation improves its predictions. Saouma et al. [1987] extended the criterion to anisotropic solids by adopting a direction-dependent tensile strength. According to Table 2.1, the MTS criterion is the most widely used fracture growth criterion in anisotropic materials. This is due to its simplicity and accurate predictions. The MTS criterion in anisotropic materials is formulated as [Saouma et al., 1987; Nejati et al., 2020a]

$$\begin{cases} \dfrac{d\hat{\sigma}_\theta}{d\theta} = 0 \ , \quad \dfrac{d^2\hat{\sigma}_\theta}{d\theta^2} < 0 \ , \qquad \left(\hat{\sigma}_\theta = \dfrac{\sigma_\theta}{\sigma^c_\phi} \right) \ , \\ \\ \hat{\sigma}_\theta = 1 \ , \end{cases} \tag{2.1}$$

where $\hat{\sigma}_\theta$ is the tangential stress normalized by the direction-dependent tensile strength of the material, known as σ^c_ϕ. The subscript ϕ is the angle between the crack growth direction and the principal direction 1 (see Figure 2.4). The first statement in Eq. (2.1) states that a crack propagates along a direction where the normalized tangential stress reaches the maximum value (i.e. kinking along $\theta = \theta_0$). The second statement postulates that the tangential stress reaches the critical tensile strength at the onset of fracture growth.

We use Eq. (A.1.6) to write the tangential component of stress at the crack tip under mixed-mode I/II loading:

$$\sigma_\theta = \frac{K_{\text{eff}}}{\sqrt{2\pi r}} \left(\Re \left[\frac{-\left(\lambda \pm \mu_2\sqrt{1-\lambda^2}\right)\left(\mu_1 \sin\theta + \cos\theta\right)^{3/2} + \left(\lambda \pm \mu_1\sqrt{1-\lambda^2}\right)\left(\mu_2 \sin\theta + \cos\theta\right)^{3/2}}{(\mu_1 - \mu_2)} \right] + \frac{T\sqrt{2\pi r}}{K_{\text{eff}}} \sin^2\theta \right) . \tag{2.2}$$

Here, r and θ are the polar coordinates, μ_1 and μ_2 are the complex parameters defined in Eq. (A.1.5), $K_{\text{eff}} = (K_{\text{I}}^2 + K_{\text{II}}^2)^{1/2}$ and $\lambda = K_{\text{II}}/K_{\text{eff}}$ are respectively the effective stress intensity factor and the mode-mixity parameter (defined in Eq. (A.1.7)), and T is the T-term, a stress term acting parallel to the crack. $\lambda = 0$ and $\lambda = \pm 1$ respectively denote pure mode I and pure mode II loading conditions, while the range $-1 < \lambda < 1$ corresponds to different mixed-mode I/II configurations where different contributions of each mode are present. The ± sign in Eq. (2.2) represents the sign of the mode I stress intensity factor. The sign $+$ is used when $K_{\mathrm{I}} > 0$, whereas $-$ is employed for cases where $K_{\mathrm{I}} < 0$ (closure of initially-open cracks). A positive (tensile) T-stress enhances the tangential stress, σ_θ, while a negative (compressive) one reduces it.

Due to the complexity of the stress field near the crack tip, σ^c_ϕ cannot be measured directly. In order to circumvent this difficulty, σ^c_ϕ is often determined using the mode I fracture toughness of the material as follows. Assume $K_{\mathrm{Ic}}(\phi)$ is the mode I fracture toughness for a co-planar fracture growth along a direction which forms the angle of ϕ with the principal direction 1. Considering a linear elastic stress field near the crack tip, one can determine the tensile strength from the stress along the crack bisector at a critical distance, L_c, as

$$\sigma^c_\theta = \frac{K_{\mathrm{Ic}}(\phi)}{\sqrt{2\pi L_c}}\,, \tag{2.3}$$

where L_c is often assumed to be the length of the fracture process zone (FPZ) at the onset of crack propagation. By substituting $r = L_{\mathrm{c}}$, Eqs. (2.2) and (2.3) into Eq. (2.1), the normalized tangential stress is formulated as

$$\hat{\sigma}_\theta = \frac{K^c_{\mathrm{eff}}}{K_{\mathrm{Ic}}(\phi)} \left(\Re \left[\frac{-\left(\lambda \pm \mu_2\sqrt{1-\lambda^2}\right)\left(\mu_1 \sin\theta + \cos\theta\right)^{3/2} + \left(\lambda \pm \mu_1\sqrt{1-\lambda^2}\right)\left(\mu_2 \sin\theta + \cos\theta\right)^{3/2}}{(\mu_1 - \mu_2)} \right] + \frac{T\sqrt{2\pi L_{\mathrm{c}}}}{K_{\mathrm{eff}}} \sin^2\theta \right)\,. \tag{2.4}$$

Eq. (2.4) is used together with Eq. (2.1) to obtain the kink angle, θ_0, and the effective stress intensity factor at the onset of fracture extension, K^c_{eff}. It is worth noting that there is an important difference in the MTS formulation of anisotropic materials compared to isotropic ones. The predicted kink angle in isotropic materials always occurs along directions where the shear stress is zero. However, due to the variation of the tensile strength, the kink angle, θ_0, in anisotropic materials can be oriented along directions where a considerable shear stress exists.

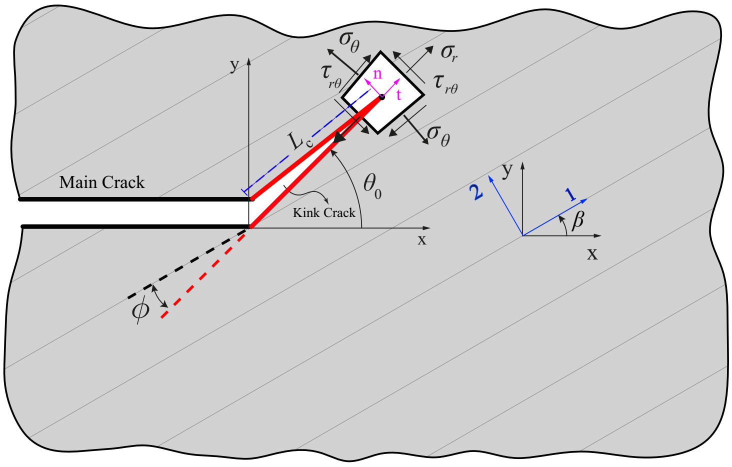

Figure 2.4: Schematic representation of the existing fracture growth criteria when the kinked crack is subjected to mixed tensile and shear stresses.

2.4.2 Maximum energy release rate (MERR)

The energy release rate (ERR) is defined as the rate at which the total potential energy of a cracked body, Π, decreases with respect to an increase in fracture surface, A: $\mathcal{G}(\theta) = -d\Pi/dA$. According to the maximum energy release rate (MERR) criterion, a crack extends in the direction θ_0 at which the maximum energy is released for an increment of crack extension. The fracture extends once the ERR reaches a critical value which is a material property. One can therefore formulate the classical MERR criterion as [Judt et al., 2015, 2019; Nejati et al., 2020a]

$$\begin{cases} \dfrac{d\hat{\mathcal{G}}(\theta)}{d\theta} = 0 \ , \quad \dfrac{d^2\hat{\mathcal{G}}(\theta)}{d\theta^2} < 0 \quad , \qquad \left(\hat{\mathcal{G}}(\theta) = \dfrac{\mathcal{G}(\theta)}{\mathcal{G}_{\mathrm{c}}(\phi)} \right) \quad , \\ \\ \hat{\mathcal{G}}(\theta) = 1 \ . \end{cases} \tag{2.5}$$

Here, $\mathcal{G}_{\mathrm{c}}(\phi)$ is the critical energy release rate along the direction of a potential crack extension, which forms an angle ϕ with the principal direction 1. In the classical form of the MERR criterion, it is assumed that $\mathcal{G}_{\mathrm{c}}(\phi)$ embodies the energy released due to tensile failure, so that $\mathcal{G}_{\mathrm{c}}(\phi) = \mathcal{G}_{\mathrm{Ic}}(\phi)$. Note that ϕ depends on θ: $\phi = \theta - \beta$. The first term in Eq. (2.5) states that the crack extends at an angle $\theta = \theta_0$, where the normalized ERR,

$\hat{\mathcal{G}}(\theta)$, reaches its maximum. The second term in Eq. (2.5) defines the critical driving force at the onset of crack extension.

Generally, three approaches are available to determine the ERR due to crack extension: 1) Exact solution: Obata et al. [1989]; Azhdari and Nemat-Nasser [1996]; Yang and Yuan [2000] applied this method to anisotropic materials subjected to in-plane loadings. When employing this method, the function $\mathcal{G}(\theta)$ is exactly determined by using the dislocation technique, which formulates the post-kinking behavior. This formulation constructs a system of integral equations which can be solved by using different numerical methods (see Erdogan et al. [1973]). This method can model the crack kinking behavior even when the kinked segment is large. 2) Approximate solution: By applying the modified Irwin's method, the function $\mathcal{G}(\theta)$ can be computed for a virtual crack extension when noncollinear crack growth takes place at an angle θ. Hussain et al. [1974] first suggested the modified Irwin's method for isotropic solids. The method was then extended to anisotropic materials by Azhdari and Nemat-Nasser [1996]. Owing to the assumption of an infinitesimally small kink in this method, the stress intensity factors at the kinked crack can be directly derived by the elastic stress field around the main crack tip prior to crack kinking [Li and Xu, 2007]. Therefore, this method, which provides an approximation for the ERR function, has received considerable attention due to the simplicity of its closed-form solution. 3) The J-integral formulation: The third formulation uses the J-vector to determine the ERR function [Chang and Pu, 1996; Ma and Korsunsky, 2005; Judt et al., 2015, 2019]. Note that the J-vector approach determines the energy release rate function considering the state of crack fields before any kink formation. This is in contrast to the dislocation technique and approximate solution, which characterize the ERR function using the post-kinking state [Chang and Pu, 1996]. In this paper, we employ the exact formulation to calculate the ERR. However, a comparison of the results from the exact formulation with the ones from the approximate solution in A.2.3 indicates that the two methods yield similar values for the cases investigated in this paper.

The energy release rate due to the kink formation at the angle θ is determined from [Yang and Yuan, 2000]

$$\mathcal{G}(\theta) = \frac{1}{2}\mathbf{k}^{(k)\intercal}\boldsymbol{L}\,\mathbf{k}^{(k)}, \tag{2.6}$$

where $\boldsymbol{L}$ is a second-rank tensor related to the elasticity constants, and is defined in the kink coordinate system (tn) as

$$\boldsymbol{L} = \frac{\tilde{S}_{11}}{E}\begin{pmatrix} \cos\theta & \sin\theta \\ -\sin\theta & \cos\theta \end{pmatrix}\begin{pmatrix} \Im(\mu_1+\mu_2) & \Im(\mu_1\mu_2) \\ \Im(\mu_1\mu_2) & \Im(\mu_1\mu_2(\bar{\mu_1}+\bar{\mu_2})) \end{pmatrix}\begin{pmatrix} \cos\theta & \sin\theta \\ -\sin\theta & \cos\theta \end{pmatrix}^{\mathsf{T}} = \begin{pmatrix} L_{11} & L_{12} \\ L_{21} & L_{22} \end{pmatrix}, \tag{2.7}$$

and $\mathbf{k}^{(k)}$ is a vector containing mode I and II stress intensity factors at the kink:

$$\begin{pmatrix} K_{\mathrm{II}}^{(k)} \\ K_{\mathrm{I}}^{(k)} \end{pmatrix} = K_{\mathrm{eff}}\left(\begin{pmatrix} C_{22} & C_{21} \\ C_{12} & C_{11} \end{pmatrix}\begin{pmatrix} \lambda \\ \pm\sqrt{1-\lambda^2} \end{pmatrix} + \frac{T\sqrt{r}}{K_{\mathrm{eff}}}\begin{pmatrix} b_2 \\ b_1 \end{pmatrix}\right). \tag{2.8}$$

Here, the coefficients C_{ij} and b_{j} are determined based on the technique chosen to obtain the ERR function. Details regarding how to determine $\mathbf{k}^{(k)}$, employing both exact and approximate formulations are given in A.2. Once $\mathbf{k}^{(k)}$ is obtained, one simply substitutes the ERR function (Eq. 2.6) into Eq. (2.5) to formulate the MERR criterion based on the maximum of the normalized ERR value.

2.4.3 Maximum strain energy density (MSED)

The MSED criterion predicts that the crack extends along the direction at which the intensity of the local strain energy density, $\mathcal{S}(\theta)$, becomes stationary [Ye and Ayari, 1994; Nejati et al., 2020a]. For isotropic materials, this stationary point is a local minimum [Sih, 1974], whereas for anisotropic materials, a local maximum of the normalized SED determines the direction of crack growth [Zhang et al., 1989; Ye and Ayari, 1994; Nejati et al., 2020a]. We highlight that the minimum of the SED function gives highly inaccurate predictions for the angle of fracture growth [Zhang et al., 1989; Ye and Ayari, 1994; Nejati et al., 2020a]. The classical MSED criterion for anisotropic materials can therefore be formulated as [Nejati et al., 2020a]

$$\begin{cases} \dfrac{d\hat{\mathcal{S}}(\theta)}{d\theta} = 0 \ , \quad \dfrac{d^2\hat{\mathcal{S}}(\theta)}{d\theta^2} < 0 \ , \quad \left(\hat{\mathcal{S}}(\theta) = \dfrac{\mathcal{S}(\theta)}{\mathcal{S}_{\mathrm{Ic}}(\phi)} \right) \ , \\ \\ \hat{\mathcal{S}}(\theta) = 1 \ . \end{cases} \tag{2.9}$$

The first statement of Eq. (2.9) determines the orientation of the crack extension, θ_0, while the effective fracture toughness is evaluated according to the second expression at $\theta = \theta_0$. Note that $\mathcal{S}_{\mathrm{Ic}}(\phi)$ is the intensity of the direction-dependent critical strain energy density along ϕ, forming an angle $\phi = \theta - \beta$ with respect to direction 1 (see Figure 2.4). In general, the correlation between the strain energy intensity, $\mathcal{S}(\theta)$, and the strain energy density, $\tilde{U}$, can be written in polar coordinates as

$$\tilde{U} = \frac{\sigma_{\mathrm{r}}\epsilon_{\mathrm{r}} + \sigma_{\theta}\epsilon_{\theta} + \tau_{\mathrm{r}\theta}\gamma_{\mathrm{r}\theta}}{2} = \frac{\mathcal{S}(\theta)}{r} \ . \tag{2.10}$$

Employing the stress and strain relations given in Eqs. (A.1.6) and (A.1.11), the intensity function of the SED , $\mathcal{S}(\theta)$, is defined as

$$\mathcal{S}(\theta) = \frac{{K_{\mathrm{eff}}}^2}{4\pi E} \begin{pmatrix} \tilde{\sigma}_{\mathrm{r}}(\mu_{\mathrm{k}}, \theta, \lambda) + \dfrac{T\sqrt{2\pi r}}{K_{\mathrm{eff}}} \cos^2\theta \\ \tilde{\sigma}_{\theta}(\mu_{\mathrm{k}}, \theta, \lambda) + \dfrac{T\sqrt{2\pi r}}{K_{\mathrm{eff}}} \sin^2\theta \\ \tilde{\tau}_{\mathrm{r}\theta}(\mu_{\mathrm{k}}, \theta, \lambda) - \dfrac{T\sqrt{2\pi r}}{K_{\mathrm{eff}}} \sin\theta\cos\theta \end{pmatrix}^{\intercal} \begin{pmatrix} \tilde{\epsilon}_{\mathrm{r}}(\tilde{S}_{ij}, \mu_{\mathrm{k}}, \theta, \lambda) + \dfrac{T\sqrt{2\pi r}}{K_{\mathrm{eff}}} \tilde{S}_{\mathrm{r}} \\ \tilde{\epsilon}_{\theta}(\tilde{S}_{ij}, \mu_{\mathrm{k}}, \theta, \lambda) + \dfrac{T\sqrt{2\pi r}}{K_{\mathrm{eff}}} \tilde{S}_{\theta} \\ \tilde{\gamma}_{\mathrm{r}\theta}(\tilde{S}_{ij}, \mu_{\mathrm{k}}, \theta, \lambda) + \dfrac{T\sqrt{2\pi r}}{K_{\mathrm{eff}}} \tilde{S}_{r\theta} \end{pmatrix} . \tag{2.11}$$

2.5 Experimental data versus theoretical predictions

Figure 2.5 illustrates the variations of the experimental data regarding the effective fracture toughness, K^c_{eff}, and the kink angle, θ_0, against β for the four sets of experiments.

Recall that β is the angle between the main crack and the foliation plane (principal direction 1). As noted previously, the direction of fracture growth in anisotropic materials depends on the interplay among three parameters: loading, geometry, and material anisotropy. Having a fixed geometry for the tested samples, one can evaluate the interplay between the mode-mixity, λ, and the anisotropy direction, β, in the experimental data presented in Figure 2.5. Depending on the sign of the mode-mixity, λ, these two contributors may either reinforce or weaken each other's influence to determine the fracture growth trajectory. The following remarks are noted regarding this interplay:

- The variations of the effective fracture toughness against β for each λ show that the effective fracture toughness generally increases with the angle β. This behavior is attributed to the effects of the compressive T-stress, which prevents large kink angles and forces the main crack with the large angle β to extend in strong material directions.

- Figure 2.5 shows that in Sets I and III (negative λ), the fracture kinks along positive directions, while in Sets II and IV (positive λ) negative kink angles are observed. To explain this behavior, we first point out that the tendency of anisotropy is to drive the main crack to kink towards the weakest plane, i.e. towards direction 1 or the foliation plane ($\theta_0 = \beta$). A negative mode-mixity parameter, $\lambda < 0$, assists the tendency to kink towards direction 1, with the kink angles in the range $\theta_0 > 0$. On the other hand, a positive mixed-mode parameter, $\lambda > 0$, opposes the tendency of anisotropy, driving the main crack to kink at negative angles ($\theta_0 < 0$). For both negative and positive λ, the extent of the kink angle significantly depends on the value of the T-stress, where a compressive T-stress prevents the development of high kink angles.

- Another observation in Figure 2.5 is that the scatter of data in Set IV (positive λ) is more significant than the scatter in the data associated to Set III (negative λ). The data scatter in rocks can be attributed to the micro-cracking mechanism changing from the intergranular dominance to the transgranular dominance [Nejati et al., 2021a]. In the case of the dominant intergranular mechanism, the crack grows along the sheet silicates such as biotite and chlorite. In the transgranular dominance, however, the crack passes through patches of stiffer quartz and feldspar minerals. In rocks such as Grimsel Granite, the grain size can reach about 1 cm, which is quite large with respect to the specimen size. This means that the effect of heterogeneity is more pronounced when the transgranular mechanism becomes dominant, and thus the fracture toughness is more scattered. In the positive mode-mixity (such as Set IV), the competition is in favor of loading, and a transgranular mechanism with more data scatter is expected. On the other hand, in Set III with negative mode-mixity, the material tendency and loading both derive the crack at a small angle with respect to the foliation plane, where an intergranular failure and small scatter in data is expected.

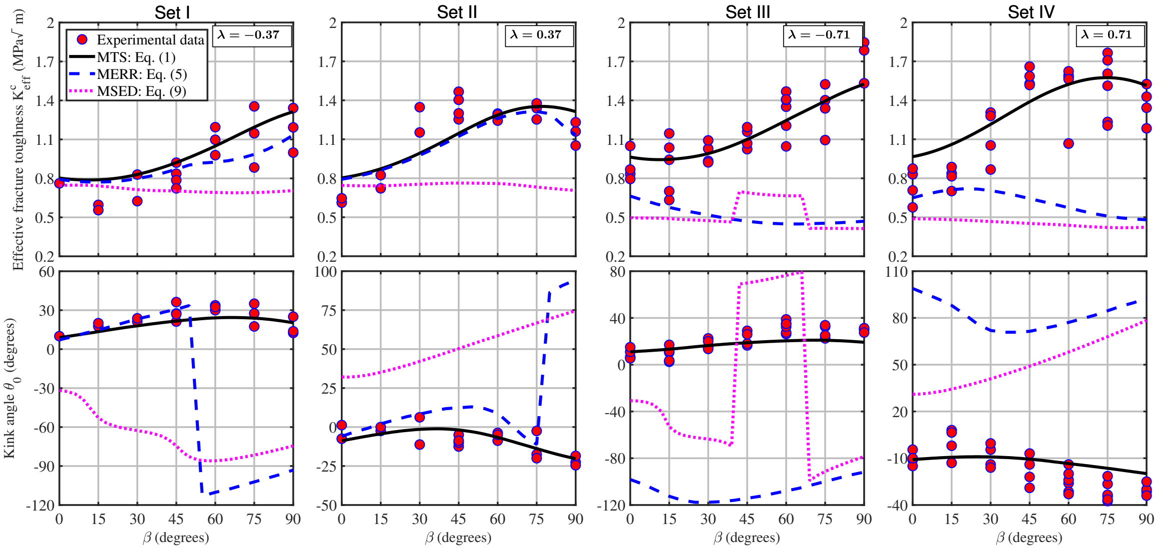

Figure 2.5: Comparison of the experimental data on the kink angle, θ_0, and the effective fracture toughness, K^c_{eff}, and the predictions of the MTS, MERR, and MSED criteria in their classical forms, i.e. Eqs. (2.1), (2.5), and (2.9), respectively.

Also shown in Figure 2.5 are the predictions of the three crack growth criteria: the maximum tangential stress (MTS) (Eq. 2.1), the maximum energy release rate (MERR) (Eq. 2.5 and assuming $\mathcal{G}_\text{c}(\phi) = \mathcal{G}_\text{Ic}(\phi)$), and the maximum strain energy density (MSED) (Eq. 2.9). While a good agreement is observed between the experimental data and the MTS predictions, the estimates made by the classical forms of the energy-based criteria (i.e. MERR and MSED) are significantly inaccurate. The accurate MTS predictions indicate that tensile failure is the dominant failure mode at the crack tip. We point out that any maximum in the the intensity function of the SED that is close to the main notch is considered unacceptable and is therefore excluded. In conclusion, the classical energy-based criteria may yield significantly inaccurate predictions for crack growth in anisotropic rocks.

2.6 Revisiting energy-based growth criteria

The inconsistencies observed between the predictions of energy-based criteria and the experimental data indicate that the classical forms of the MERR and MSED criteria may not be accurate for rock-type materials. Therefore, modifications must be applied to these classical forms in order to improve their predictions. In this section, we identify the drawbacks of the classical forms of the ERR and SED intensity functions, and present improved versions of these criteria.

2.6.1 Modification of the MERR criterion

The classical formulation of the MERR criterion, given in Eq. (2.5), appears to have a significant problem when applied to quasi-brittle materials which have significantly different tensile and shear strengths. In order to elaborate on this, we first decompose the energy release rate in Eq. (2.6) into two components:

$$\mathcal{G}^{(k)} = \underbrace{\frac{1}{2}K_{\mathrm{I}}^{(k)}(L_{21}K_{\mathrm{II}}^{(k)} + L_{22}K_{\mathrm{I}}^{(k)})}_{\mathcal{G}_{\mathrm{I}}^{(k)}} + \underbrace{\frac{1}{2}K_{\mathrm{II}}^{(k)}(L_{11}K_{\mathrm{II}}^{(k)} + L_{12}K_{\mathrm{I}}^{(k)})}_{\mathcal{G}_{\mathrm{II}}^{(k)}} \; . \tag{2.12}$$

Here, $\mathcal{G}_{\mathrm{I}}^{(k)}$ and $\mathcal{G}_{\mathrm{II}}^{(k)}$ represent the ERR contributions of tensile opening and shear sliding of the kink, respectively, as schematically shown in Figure 2.6. In other words, $\mathcal{G}_{\mathrm{I}}^{(k)}$ is the ERR due to the release of the tensile stress, σ_θ, upon kink formation, while $\mathcal{G}_{\mathrm{II}}^{(k)}(\theta)$ is the ERR contribution due to the release of the shear stress, $\tau_{\mathrm{r}\theta}$. Note that Figure 2.6 depicts the state of the stress before kinking occurs. Due to kinking, the stresses σ_θ and $\tau_{\mathrm{r}\theta}$ along the kink are released to cause the displacement discontinuities Δu_{n} (normal to the kink) and Δu_{t} (along the kink).

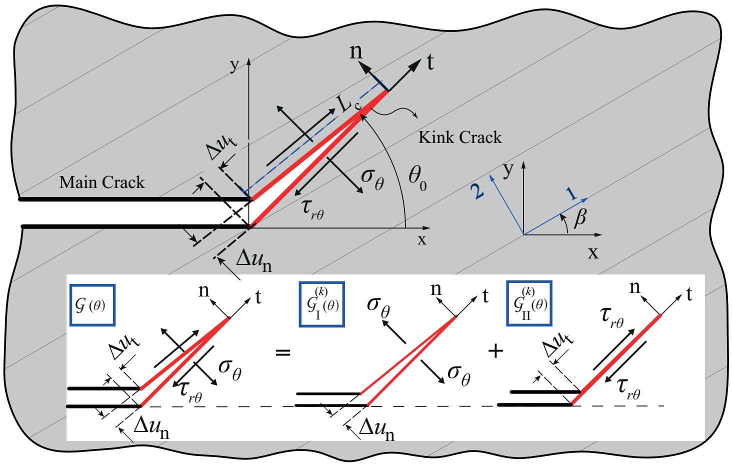

Figure 2.6: Schematic representation of the decomposition of the energy release rate into tensile and shear components.

It now becomes apparent that an incompatibility exists between the numerator and denominator in the definition of the normalized ERR function in Eq. (2.5). While $\mathcal{G}$ includes the contributions of both tensile opening and shear sliding due to the kink formation, $\mathcal{G}_{\mathrm{c}}$ is the critical fracture energy related to either tensile failure or shear rupture. When one uses the tensile fracture energy in the denominator of $\hat{\mathcal{G}}$, the term $\mathcal{G}_{\mathrm{II}}^{(k)}$ becomes irrelevant. Similarly the use of the shear fracture energy in the denominator of $\hat{\mathcal{G}}$ renders the term $\mathcal{G}_{\mathrm{I}}^{(k)}$ irrelevant. It is therefore essential to reformulate Eq. (2.5) in order to make it more physically meaningful, particularly for quasi-brittle materials that exhibit significantly different tensile and shear fracture energies.

Another important drawback of the formulation in Eq. (2.5) is that it does not enforce any constraint on the angle at which a kink can form. The energy released due to tensile opening, $\mathcal{G}_{\mathrm{I}}^{(k)}$, only contributes to the total energy release rate if the formation of an open kink is possible. This means that for $\mathcal{G}_{\mathrm{I}}^{(k)}$ to contribute to the total ERR, the following condition must be satisfied for the opening displacement at the kink (see Figure 2.6):

$$\Delta u_{\mathrm{n}}(\theta) = L_{21} K_{\mathrm{II}}^{(k)} + L_{22} K_{\mathrm{I}}^{(k)} \geq 0\,. \tag{2.13}$$

The component $\mathcal{G}_{\mathrm{I}}^{(k)}$ can not be released in an angle, where no opening is possible, i.e. $\Delta u_{\text{n}} < 0$. For such an angle, adding $\mathcal{G}_{\text{I}}^{(k)}$ indicates an energy release rate due to the penetration of the kink surfaces into one another, which is physically impossible. Therefore, the opening-based ERR function, $\mathcal{G}_{\text{I}}^{(k)}(\theta)$, must be constrained to an interval of validity in which a potential kink can in fact open. We can define this interval of validity as $\theta_1 \leq \theta \leq \theta_2$, where θ_1 and θ_2 represent the lower and the upper bounds of the interval of validity, respectively. We note that Gao and Chiu [1992]; Yang and Yuan [2000] also emphasized the importance of constraining the ERR function to an interval of validity. However, they did not consider any decomposition of the ERR function into tensile and shear parts.

Note that from Eq. (2.8), the kink stress intensity factor, $\mathbf{k}^{(k)}$, depends on the T-stress value, T, of the main crack. This dependency indicates that the T-stress value can play a crucial role in constraining the interval of validity. A compressive T-stress reduces the kink stress intensity factors, thereby preventing an opening of the kink at certain angles. A highly compressive T-stress can therefore shrink the interval of validity for the opening mode ERR to a small interval near the notch bisector. In such cases, the main crack deflects back toward the main straight path and thus the kink angle, θ_0, is predicted to be in the vicinity of the main crack bisector (see Gao and Chiu [1992]). On the other hand, a significant tensile T-stress can expand the interval of validity back to the original interval, $-\pi \leq \theta \leq \pi$. Note that the contribution of $\mathcal{G}_{\text{I}}^{(k)}(\theta)$ to the total ERR must vanish outside the interval of validity. In those regions, however, energy can still be released due to shear sliding, $\mathcal{G}_{\text{II}}^{(k)}(\theta)$. By considering the interval of validity for $\mathcal{G}_{\text{I}}^{(k)}(\theta)$, we re-write Eq. (2.12) as

$$\begin{aligned}
&\mathcal{G}^{(k)}(\theta) = \mathcal{G}_{\text{I}}^{(k)}(\theta) + \mathcal{G}_{\text{II}}^{(k)}(\theta)\,, \\
&\mathcal{G}_{\text{I}}^{(k)}(\theta) = \begin{cases} \dfrac{1}{2} K_{\text{I}}^{(k)} (L_{21} K_{\text{II}}^{(k)} + L_{22} K_{\text{I}}^{(k)}) & \theta_1 \leq \theta \leq \theta_2 \\ 0 & \text{otherwise} \end{cases}\,, \\
&\mathcal{G}_{\text{II}}^{(k)}(\theta) = \frac{1}{2} K_{\text{II}}^{(k)} (L_{11} K_{\text{II}}^{(k)} + L_{12} K_{\text{I}}^{(k)}) \qquad -\pi \leq \theta \leq \pi\,.
\end{aligned} \tag{2.14}$$

In order to re-write the MERR criterion in a physically more meaningful manner, we suggest to decompose the total normalized ERR, $\hat{\mathcal{G}}$, into two components: The contribution $\hat{\mathcal{G}}_{\text{I}} = \mathcal{G}_{\text{I}}^{(k)} / \mathcal{G}_{\text{Ic}}$, constrained to an interval of validity, representing a tensile fracturing indicator, and the contribution $\hat{\mathcal{G}}_{\mathrm{II}} = \mathcal{G}_{\mathrm{II}}^{(k)}/\mathcal{G}_{\mathrm{IIc}}$, representing a shear failure indicator. Using the definition of the normalized ERR, we introduce a modified form of the MERR criterion given as

$$\begin{cases} \dfrac{d\hat{\mathcal{G}}(\theta)}{d\theta} = 0 \ , \quad \dfrac{d^2\hat{\mathcal{G}}(\theta)}{d\theta^2} < 0 \ , \quad \hat{\mathcal{G}}(\theta) = \begin{cases} \overbrace{\dfrac{\mathcal{G}_{\mathrm{I}}^{(k)}(\theta)}{\mathcal{G}_{\mathrm{Ic}}(\phi)}}^{\hat{\mathcal{G}}_{\mathrm{I}}(\theta)} + \overbrace{\dfrac{\mathcal{G}_{\mathrm{II}}^{(k)}(\theta)}{\mathcal{G}_{\mathrm{IIc}}(\phi)}}^{\hat{\mathcal{G}}_{\mathrm{II}}(\theta)} & \theta_1 \leq \theta \leq \theta_2 \\ \dfrac{\mathcal{G}_{\mathrm{II}}^{(k)}(\theta)}{\mathcal{G}_{\mathrm{IIc}}(\phi)} & \text{otherwise} \end{cases} \ , \\ \\ \hat{\mathcal{G}}(\theta) = 1 \ . \end{cases} \tag{2.15}$$

In fact, the classical normalized ERR function, often reported in the literature, is a special case of Eq. (2.15) which assumes $\mathcal{G}_{\mathrm{IIc}} = \mathcal{G}_{\mathrm{Ic}}$ with no assumption concerning the interval of validity (see for example Azhdari and Nemat-Nasser [1998]; Nejati et al. [2020b]; Judt et al. [2019]). The classical form may be accurate for materials that exhibit comparable shear and tensile fracture toughness values, or for cases where the contribution of the T-stress is insignificant. However, the classical form can result in highly inaccurate predictions for quasi-brittle materials for which $\mathcal{G}_{\mathrm{IIc}}$ is significantly greater than $\mathcal{G}_{\mathrm{Ic}}$, or for cases where significant T-stresses considerably confine the interval of validity. The ratio of true mode II to mode I fracture toughness in rocks is normally $K_{\mathrm{IIc}}/K_{\mathrm{Ic}} \geq 3$, which translates to a ratio of $\mathcal{G}_{\mathrm{IIc}}/\mathcal{G}_{\mathrm{Ic}} > 9$ for fracture energy [Shen and Stephansson, 1994; Bahrami et al., 2020; Nejati et al., 2021a]. This suggests that, assuming $\mathcal{G}_{\mathrm{IIc}} = \mathcal{G}_{\mathrm{Ic}}$ is a very inaccurate assumption for many rock-type materials, and that applying the classical form of the MERR criterion likely results in significant prediction errors.

We note that a simpler form of the modified MERR criterion (Eq. 2.15) was suggested by Shen and Stephansson [1994] for isotropic materials and Shen and Shi [2016]; Shen et al. [2014] for transversely isotropic rocks. Their formulations, however, ignore the importance of defining an interval of validity for $\hat{\mathcal{G}}_{\mathrm{I}}$, and employ the first sub-function of the piecewise ERR function introduced in Eq. (2.15) without applying any interval of validity. This is mainly the case, as they do not consider the T-stress in their crack tip stress formulation. Nevertheless, numerical results by [Shen and Stephansson, 1994; Zhang et al., 2017b] have demonstrated that their modified versions are able to accurately predict crack growth patterns due to shear failure. We show in this paper that our modified version of the MERR criterion in Eq. (2.15) is not only potentially helpful when predicting shear failure, but additionally yields significantly better predictions for tensile-stress-based crack growth in anisotropic rocks.

We note that the difficulty in measuring shear fracture toughness, K_{IIc}, can limit the use of our modified ERR function. However, due to the large ratio of $\mathcal{G}_{\mathrm{IIc}}/\mathcal{G}_{\mathrm{Ic}}$, one can ignore the term $\mathcal{G}_{\mathrm{II}}^{(k)}/\mathcal{G}_{\mathrm{IIc}}$ in our modified formulation, and thus use the normalized form $\hat{\mathcal{G}} = \mathcal{G}_{\mathrm{I}}^{(k)}/\mathcal{G}_{\mathrm{Ic}}$ within the interval of validity. In such cases, the MERR criterion can only predict crack growth due to tensile failure. In addition, we expect that the modified MERR criterion can be superior to the MTS criterion in the sense that it can predict a potential failure due to shear stresses, whereas the MTS criterion fails in that regard. Shear failure is the predominant mode of failure when high compressive confining stresses are applied, e.g. under in-situ condition.

2.6.2 Modification of the MSED criterion

Similar to the MERR criterion, we can decompose the strain energy density, $\tilde{U}$, into two components, $\tilde{U} = \tilde{U}_{\mathrm{I}} + \tilde{U}_{\mathrm{II}}$, where $\tilde{U}_{\mathrm{I}}$ and $\tilde{U}_{\mathrm{II}}$ represent the strain energy due to normal stresses and shear stresses, respectively, in the polar coordinate system:

$$\tilde{U} = \frac{\sigma_{\mathrm{r}}\epsilon_{\mathrm{r}} + \sigma_{\theta}\epsilon_{\theta}}{2} + \frac{\tau_{\mathrm{r}\theta}\gamma_{\mathrm{r}\theta}}{2} = \tilde{U}_{\mathrm{I}} + \tilde{U}_{\mathrm{II}} \ . \tag{2.16}$$

Accordingly, one can decompose the intensity of strain energy density into two components: $\mathcal{S} = \mathcal{S}_{\mathrm{I}} + \mathcal{S}_{\mathrm{II}}$, where $\mathcal{S}_{\mathrm{I}}$ and $\mathcal{S}_{\mathrm{II}}$ represent the strain energy intensities due to normal stresses and shear stresses, respectively:

$$\tilde{U} = \frac{\mathcal{S}(\theta)}{r} = \frac{\mathcal{S}_{\mathrm{I}}(\theta)}{r} + \frac{\mathcal{S}_{\mathrm{II}}(\theta)}{r} \ . \tag{2.17}$$

Employing the stress and strain relations given in Eqs. (A.1.6) and (A.1.11), the SED intensity functions $\mathcal{S}_{\mathrm{I}}(\theta)$ and $\mathcal{S}_{\mathrm{II}}(\theta)$ are defined as

$$\begin{aligned}
\mathcal{S}_{\mathrm{I}}(\theta) &= \frac{{K_{\mathrm{eff}}}^2}{4\pi E}\begin{pmatrix} \tilde{\sigma}_{\mathrm{r}}(\mu_{\mathrm{k}},\theta,\lambda) + \dfrac{T\sqrt{2\pi r}}{K_{\mathrm{eff}}}\cos^2\theta \\ \tilde{\sigma}_{\theta}(\mu_{\mathrm{k}},\theta,\lambda) + \dfrac{T\sqrt{2\pi r}}{K_{\mathrm{eff}}}\sin^2\theta \end{pmatrix}^{\mathsf{T}} \begin{pmatrix} \tilde{\epsilon}_{\mathrm{r}}(\tilde{S}_{ij},\mu_{\mathrm{k}},\theta,\lambda) + \dfrac{T\sqrt{2\pi r}}{K_{\mathrm{eff}}}\tilde{S}_{\mathrm{r}} \\ \tilde{\epsilon}_{\theta}(\tilde{S}_{ij},\mu_{\mathrm{k}},\theta,\lambda) + \dfrac{T\sqrt{2\pi r}}{K_{\mathrm{eff}}}\tilde{S}_{\theta} \end{pmatrix} \ , \\
\mathcal{S}_{\mathrm{II}}(\theta) &= \frac{{K_{\mathrm{eff}}}^2}{4\pi E}\left(\tilde{\tau}_{\mathrm{r}\theta}(\mu_{\mathrm{k}},\theta,\lambda) - \frac{T\sqrt{2\pi r}}{K_{\mathrm{eff}}}\sin\theta\cos\theta\right)\left(\tilde{\gamma}_{\mathrm{r}\theta}(\tilde{S}_{ij},\mu_{\mathrm{k}},\theta,\lambda) + \frac{T\sqrt{2\pi r}}{K_{\mathrm{eff}}}\tilde{S}_{r\theta}\right) \ .
\end{aligned} \tag{2.18}$$

There are two remarks that should be taken into account: 1) Since the intensity of the strain energy density is compared to its critical value during tensile-based failure, $\mathcal{S}_{\mathrm{Ic}}$, only the tensile-based contribution of the intensity of the strain energy density, $\mathcal{S}_{\mathrm{I}}$, should be included as a driving force for the fracture growth. 2) The validity of the normalized intensity of the strain energy density must be constrained to an angular interval in which the tangential strain (given in Eq. A.1.11) is positive: $\epsilon_\theta > 0$. We therefore define an interval of validity, $\theta_1 \le \theta \le \theta_2$, for the SED intensity function. Any maximum occurring outside this interval of validity must be ignored, as tensile-based crack growth along a direction with negative tangential strain is physically impossible. By applying these two remarks, a modified formulation of the MSED criterion is given by

$$\begin{cases} \dfrac{d\hat{\mathcal{S}}(\theta)}{d\theta} = 0 \ , \quad \dfrac{d^2\hat{\mathcal{S}}(\theta)}{d\theta^2} < 0, \quad \left(\hat{\mathcal{S}}(\theta) = \dfrac{\mathcal{S}_{\mathrm{I}}(\theta)}{\mathcal{S}_{\mathrm{Ic}}(\phi)}; \quad \text{if} \quad \theta_1 \le \theta \le \theta_2\right), \\ \\ \hat{\mathcal{S}}(\theta) = 1 \ . \end{cases} \tag{2.19}$$

2.6.3 Re-assessment of the energy-based fracture criteria

Figure 2.7 re-assesses the MERR and the MSED theories by comparing the results of their modified versions with experimental data. It is evident that the modified versions are significantly more accurate than the classical formulations (Figure 2.5). According to Figure 2.7, while a good agreement is seen between the experimental data and the MTS and modified MERR predictions, the MSED, even in the modified form, yields somewhat inaccurate predictions that are furthest away from the experimental data. Particularly for sets III and IV, where higher levels of T-stresses exist (see Table 2.5), the MSED estimates seem to deviate more significantly from the experimental results.

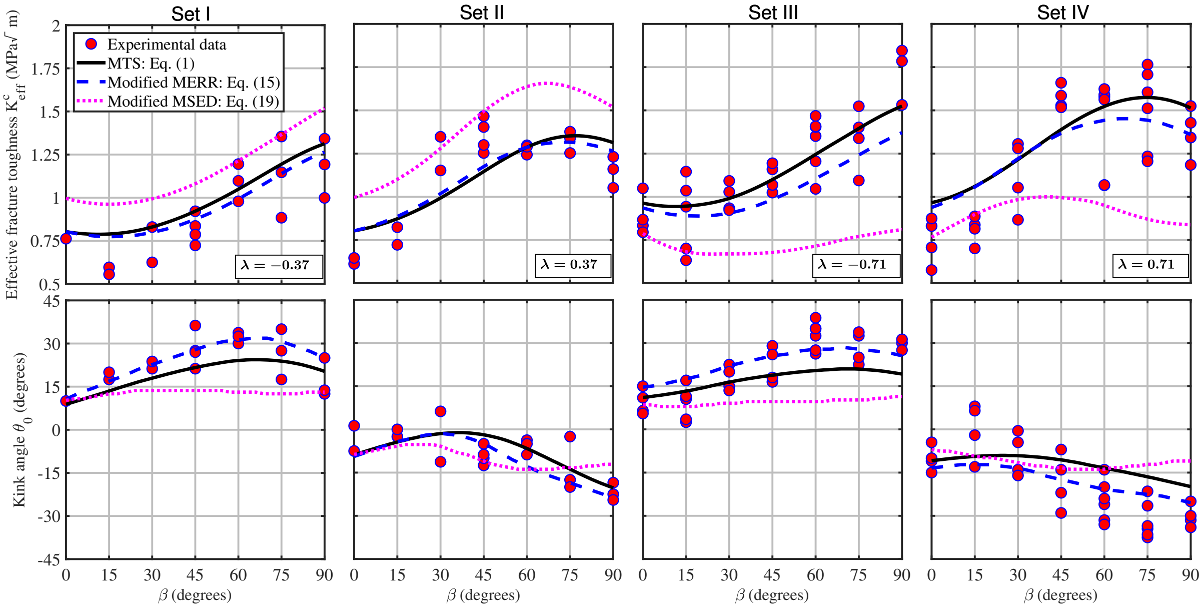

Figure 2.7: Comparison of experimental data on kink angle, θ_0, and the effective fracture toughness, K^c_{eff}), with the predictions of the MTS (Eq. 2.1), modified MERR (Eq. 2.15), and modified MSED (Eq. 2.19).

The accuracy of the MTS model and the modified energy-based criteria (i.e. MERR and MSED) are compared in Table 2.6, where the error norms, e_{θ_0} and $e_{K^c_{\mathrm{eff}}}$, are defined as

$$e_{\theta_0} = \sqrt{\frac{\sum_{i=1}^{N}\Big((\theta_0^{\rm e})_i - (\theta_0^{\rm p})_i\Big)^2}{\sum_{i=1}^{N}\Big((\theta_0^{\rm e})_i - (\bar{\theta}_0^{\rm e})_i\Big)^2}}, \quad e_{K_{\rm eff}^{c}} = \sqrt{\frac{\sum_{i=1}^{N}\Big((K_{\rm eff}^{\rm c,\,e})_i - (K_{\rm eff}^{\rm c,\,p})_i\Big)^2}{\sum_{i=1}^{N}\Big((K_{\rm eff}^{\rm c,\,e})_i - (\bar{K}_{\rm eff}^{\rm c,\,e})_i\Big)^2}}. \tag{2.20}$$

Here, $(\theta_0^{\rm e})_i$ and $(K_{\rm eff}^{\rm c,\,e})_i$ are the ith experiment data on the kink angle and effective fracture toughness, respectively, which are compared to the predictions of each individual growth criterion for that test, $(\theta_0^{\rm p})_i$ and $(K_{\rm eff}^{\rm c,\,p})_i$. The denominator is the standard deviation, which shows how different the experimental data are from the mean values $(\bar{\theta}_0^{\rm e})_i$ and $(\bar{K}_{\rm eff}^{\rm e})_i$. The lowest value of the error is unity, which implies that the predictions are exactly the same as the mean values of the experimental data. The higher the error values, the higher are the deviations of the predictions from the mean values. The errors in Table 2.6 indicate that the MTS and the MERR are equally accurate in their predictions, whereas the MSED results in predictions that are the furthest away from the experimental data.

Error function	Criterion	Set I	Set II	Set III	Set IV	Average
e_{θ_0}	MTS	1.53	**1.30**	1.93	1.86	1.66
	MERR	**1.28**	1.42	**1.52**	**1.45**	**1.42**
	MSED	2.87	1.57	3.43	2.20	2.52
$e_{K_{\rm eff}^{c}}$	MTS	1.40	2.65	**1.16**	1.36	**1.64**
	MERR	**1.28**	**2.37**	1.55	**1.29**	1.62
	MSED	2.54	4.69	3.81	2.79	3.46

Table 2.6: Comparison of the prediction errors for different fracture growth criteria. The error norms are defined in Eq. (2.20).

2.7 Discussion

Among the three criteria, the MERR criterion is expected to be theoretically the most accurate criterion since this model considers the energy release rate associated with both opening and shearing deformations at the kink. Unlike the MTS criterion, which focuses only on tensile-based fracturing due to the tensile stress, the MERR criterion includes the influence of shear stresses on the kink plane during the fracturing process, enabling the prediction of shear-based failure. However, in materials with large differences between the shearing and the opening fracture toughness, such as rocks in general, the modification introduced in the normalized MERR function must be taken into account in order to achieve acceptable predictions of fracture growth path. A similar modification must be applied to the normalized intensity of the SED function to yield reasonable results. We exclude the shear strain energy density from Eq. (2.19) since the effect of shearing is not included in the critical SED intensity function, $\mathcal{S}_{\mathrm{Ic}}(\phi)$. We also emphasize that the associated normalized energy functions in the MERR and MSED criteria must be constrained to their corresponding intervals of validity. Otherwise, the predictions of the energy-based criteria are no longer reasonable in cases, where significant compressive T-stresses are present. More discussions on the performance of each criterion are given next.

2.7.1 MTS criterion

Due to the mathematical simplicity and the accuracy of predictions, the MTS is the most widely used criterion for predicting fracture growth path in rocks. However, the MTS criterion has one intrinsic drawback, which is related to the assumption that tensile-based failure always precedes shear-based failure. As long as tensile fracturing prevails, the crack growth path is predicted accurately by MTS, even for dominant mode II loading types as seen in the experimental sets III and IV. However, there is a possibility in practical applications that shear-induced fracturing precedes tensile-induced fracturing, as described in detail in Bahrami et al. [2020]. Consider the case, where the main crack is aligned with the weak direction of the material and is subjected to a pure mode II loading. Since crack kinking requires failure in the stronger direction of the material, the failure may well occur along the weak direction due to shear stresses, provided that the anisotropy is strong enough, or the T-stress is compressive enough to hinder tensile-based crack kinking. In such cases, the MTS criterion fails to predict the kink angle, $\theta_0 = 0^\circ$, since the tensile stress along the notch plane is zero. Hence, it is of great importance to recognize that the MTS predictions are reliable only when the mechanism of fracturing is mainly tension-based.

2.7.2 MERR criterion

The use of the modified version of the MERR criterion is essential to accurately predict crack growth in anisotropic rocks. Figure 2.8 compares the experimental data for θ_0 and K_{eff} with the predictions of four different versions of the MERR criterion that incorporate different assumptions into the normalized ERR function. These versions are defined as follows. 1) The original modified version as formulated in Eq. (2.15); 2) A version of Eq. (2.15) that is based on the exclusion of the energy released due to kink sliding: $\mathcal{G}_{\text{II}}^{(k)}(\theta)/\mathcal{G}_{\text{IIc}}(\phi) = 0$. 3) A version of Eq. (2.15), where tensile- and shear-based fracture energies are assumed to be equal: $\mathcal{G}_{\text{IIc}}(\phi) = \mathcal{G}_{\text{Ic}}(\phi)$. 4) A version of Eq. (2.15), where no interval of validity is considered: $-\pi \leq \theta_0 \leq \pi$. Table 2.7 compares the errors e_{θ_0} and $e_{K_{\text{eff}}}$ associated with these four versions. These results show the necessity of the modifications introduced in this paper in order to obtain reasonable predictions of the MERR criterion. We specifically note the following:

- Comparing versions 1 and 2 shows that the contribution of the shearing term, $\mathcal{G}_{\text{II}}^{(k)}(\theta)/\mathcal{G}_{\text{IIc}}(\phi)$, in the ERR function is insignificant. Therefore, if a measurement for mode II fracture toughness is not available, assuming $\hat{\mathcal{G}}(\theta) = \mathcal{G}_{\text{I}}^{(k)}(\theta)/\mathcal{G}_{\text{Ic}}(\phi)$ can still provide excellent approximations of fracture growth paths with the MERR criterion, as long as tensile fracturing prevails.

- Comparing versions 1 and 3 shows that the classical ERR formulation in Eq. (2.5), which assumes $\mathcal{G}_{\text{IIc}}(\phi) = \mathcal{G}_{\text{Ic}}(\phi)$, fails to predict accurate kink angles and effective fracture toughness values, particularly for high values of the mode-mixity ratio, λ. This is because in rocks, the fracture energy during tensile-based failure is much smaller than the fracture energy during shear-based failure. It is worth noting that the peak of the second sub-function, given in Eq. (2.15), can exceed the maximum of the first sub-function when $\mathcal{G}_{\text{IIc}}(\phi) = \mathcal{G}_{\text{Ic}}(\phi)$ is assumed for $\lambda = 0.71$ and $\beta > 15°$. This means that, according to version 3, failure may happen due to shearing at higher values of loading, which is in contrast to our experimental observations.

- Comparing versions 1 and 4 shows that considering a correct interval of validity is essential for accurate predictions of fracture growth path with the MERR criterion. We point out that the maxima of the ERR function that fall outside the interval of validity for θ_0 result in significant errors in kink angle predictions. One therefore needs to consider the interval of validity for crack growth path predictions, especially when large compressive T-stresses act on the crack.

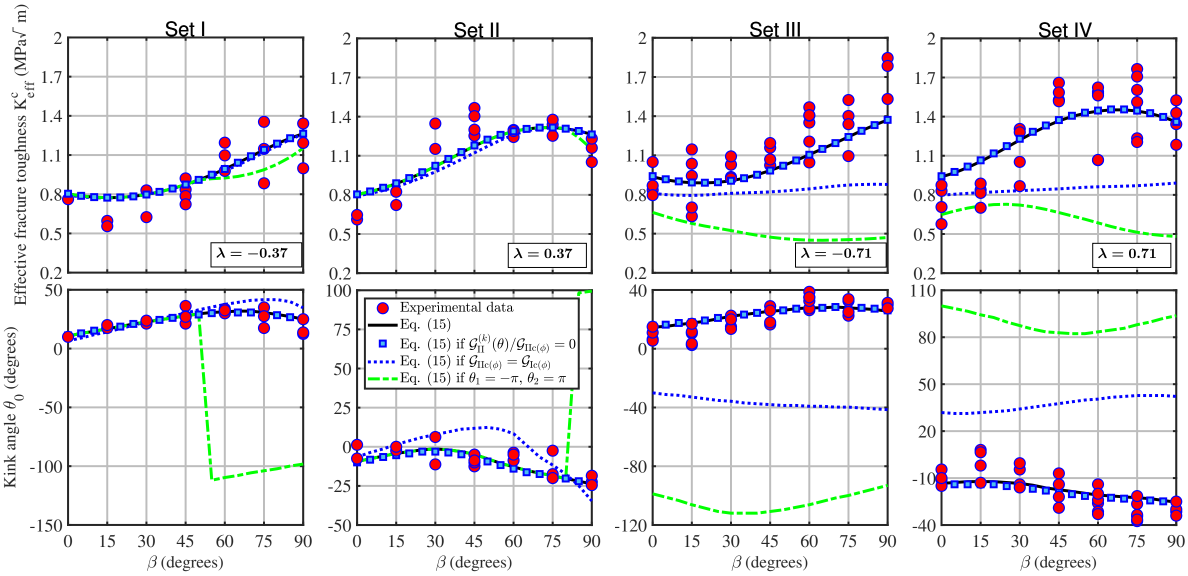

Figure 2.8: Comparison of experimental data on θ_0 and K^c_{eff} with the predictions of the MERR criterion with different assumptions.

Error function	Assumptions applied to Eq. (2.15)	Set I	Set II	Set III	Set IV	Average
e_{θ_0}	(1) No assumption	1.28	**1.42**	**1.52**	**1.45**	**1.42**
	(2) $\mathcal{G}^{(k)}_{\text{II}}(\theta)/\mathcal{G}_{\text{IIc}}(\phi) = 0$	**1.26**	1.43	1.57	1.49	1.44
	(3) $\mathcal{G}_{\text{IIc}}(\phi) = \mathcal{G}_{\text{Ic}}(\phi)$	2.37	2.88	13.53	9.37	7.04
	(4) $\theta_1 = -\pi$, $\theta_2 = \pi$	20.05	10.16	28.70	17.30	19.05
$e_{K^c_{\text{eff}}}$	(1) No assumption	**1.28**	2.37	**1.55**	**1.29**	**1.62**
	(2) $\mathcal{G}^{(k)}_{\text{II}}(\theta)/\mathcal{G}_{\text{IIc}}(\phi) = 0$	**1.28**	2.35	1.56	1.30	**1.62**
	(3) $\mathcal{G}_{\text{IIc}}(\phi) = \mathcal{G}_{\text{Ic}}(\phi)$	1.29	2.65	3.15	3.04	2.53
	(4) $\theta_1 = -\pi$, $\theta_2 = \pi$	1.43	**2.26**	5.42	4.43	3.39

Table 2.7: Comparison of the prediction errors for different formulations of the MERR criterion. The error norms are defined in Eq. (2.20).

We note that our finding about the necessity of decomposing the strain energy release function into shearing and opening parts can also give insight to derive more physically-meaningful phase-field formulations. Our results suggest that in order to build a phase-field model that accurately simulates the underlying physics of fracturing in anisotropic quasi-brittle materials, one needs to consider two directional-dependent fracture energy functions. While it is becoming more common in phase-field to use a directional-dependent fracture energy function [Rezaei et al., 2021], or to use separate tensile and shear energy functions [Li et al., 2021; Zhang et al., 2017b], it is yet to be seen the combination of both in the mathematical model which includes directional-dependent tensile and shear energy functions.

2.7.3 MSED criterion

In order to illustrate the significance of the modifications of the MSED criterion suggested in this paper, we compare in Table 2.8 the errors for different versions of the MSED criterion with different assumptions. These versions are defined as follows: 1) The original modified formula, given in Eq. (2.19); 2) The version of Eq. (2.19) that includes the intensity of the shear strain energy density; 3) The version of Eq. (2.19), where no interval of validity for θ_0 is taken into account: $-\pi < \theta_0 < \pi$. As seen in Table 2.8, the modifications suggested in this paper are essential to yield acceptable predictions for crack growth path. We also note that the inclusion of the intensity of the shear strain energy density, $\mathcal{S}_{\mathrm{II}}$ in Eq. (2.19), can lead to a maximum of the SED intensity function at the boundaries of the interval of validity, whereas excluding $\mathcal{S}_{\mathrm{II}}$ enables obtaining maxima within the interval. We also observe that the maximum value of $\mathcal{S}_{\mathrm{II}}(\theta)/\mathcal{S}_{\mathrm{Ic}}(\phi)$ always exceeds the maximum value of $\mathcal{S}(\theta)/\mathcal{S}_{\mathrm{Ic}}(\phi)$ at the interval boundary, and therefore the second version of the MSED criterion predicts material failure due to shearing only. We also note that only maximum values (and not minima) of the SED functions, located within the interval of validity, yield reasonable values for kink angles.

Error function	Assumptions applied to Eq. (2.19)	Set I	Set II	Set III	Set IV	Average
e_{θ_0}	(1) No assumption	**2.87**	**1.57**	**3.43**	**2.20**	**2.52**
	(2) $\mathcal{S}_{\mathrm{II}}(\theta) \neq 0$	14.11	11.05	29.52	9.29	15.99
	(3) $\theta_1 = -\pi$, $\theta_2 = \pi$	24.69	21.57	25.53	16.11	21.98
$e_{K^c_{\mathrm{eff}}}$	(1) No assumption	2.54	**4.69**	**3.81**	**2.79**	**3.46**
	(2) $\mathcal{S}_{\mathrm{II}}(\theta) \neq 0$	**2.04**	5.37	5.53	4.78	4.43
	(3) $\theta_1 = -\pi$, $\theta_2 = \pi$	2.84	5.51	5.70	4.85	4.73

Table 2.8: Comparison of the prediction errors for different formulations of the MSED criterion. The error norms are defined in Eq. (2.20).

2.7.4 Effects of T-stress

The T-stress is the second term in the crack tip stress series solution, acting as a constant stress parallel to the crack plane. The classical work of Cotterell and Rice [1980] on the influence of T-stress on fracture path stability in an isotropic medium was extended by Gao and Chiu [1992]; Goldstein and Shifrin [2012] to anisotropic media. Studies on the influence of the T-stress on fracture growth of anisotropic solids have been mainly theoretical [Gao and Chiu, 1992; Yang and Yuan, 2000; Shah et al., 2006], as only few articles addressed this topic experimentally [Nejati et al., 2020a]. Figure 2.9 compares the experimental data for θ_0 and K^c_{eff} with the predictions of the MTS (Eq. 2.1), the MERR (Eq. 2.15), and the MSED (Eq. 2.19), when the term containing the T-stress is excluded from the formulation of these criteria. Comparing with Figure 2.7 shows that neglecting the T-stress increases the error of predicted θ_0 and K^c_{eff} values for all three criteria. Note that the inaccuracy of the predictions is more pronounced in Sets III and IV ($\lambda = \pm 0.71$), where larger values of compressive T-stress are present. This illustrates the significant influence of the T-stress on the crack growth behavior in the tested rock samples. In addition, the predictions obtained by the MSED criterion show unacceptable, sharp variations in the kink angle. Recall that, contrary to Figure 2.9, a smooth trend of the MSED crack growth path predictions was previously observed (Figure 2.7), when the T-stress effect was taken into account.

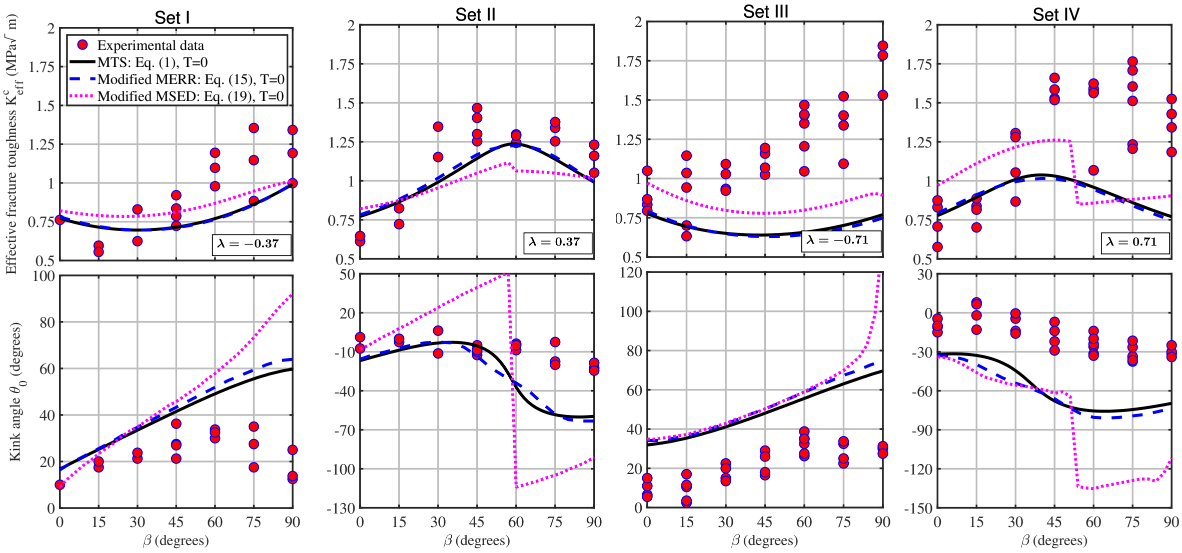

Figure 2.9: Comparison of the experimental data on θ_0 and K_{eff}^c with the predictions of the MTS, modified MERR, and modified MSED criteria when T-stress is ignored.

Lastly we highlight the fact that the adopted theoretical model, based on a homogeneous transversely isotropic material behaviour, deviates from the real-world rock material in that neither homogeneity nor transverse isotropy can perfectly describe the material response. Grimsel Granite is a heterogeneous material at the sample scale, with quartz grain diameters as large as 1 cm, and the data scatter seen in Figure 2.5 is evidence for the influence of material heterogeneity, as discussed in Section 2.5. All minerals composing Grimsel Granite (quartz, two feldspars, mica, and accessories) are themselves materials with very different degrees of anisotropy, in different orientations relative to complex geometric grain shapes. Adopting a homogeneous material model is therefore not ideal, but avoids the need to accurately capture the heterogeneity that is specific to each sample. Previous results on Grimsel Granite suggest that the transverse isotropy assumption provides a decent approximation to the material behaviour (see Dambly et al. [2019]). Adopting a model with more material constants may lead to improved accuracy, but at the expense of introducing additional complexity to the mathematical model as well as requiring additional effort to measure a large number of potentially sample-specific material parameters. We believe that the adopted mechanical model employed in this paper provides a degree of efficiency and accuracy that is suitable for most engineering applications.

2.8 Conclusions

The main findings of this article are as follows.

- The presented experimental data clearly demonstrate how two factors, the mode-mixity, λ, and the material anisotropy interact with each other to determine the kink angle in crack growth paths in anisotropic rocks. For negative values of λ, the loading effect reinforces the anisotropy to kink towards the weak plane (i.e. the foliation plane in the Grimsel Granite). On the other hand, when λ is positive, the loading counteracts the influence of strength anisotropy and thus the crack kinks away from the plane of weakness.

- Comparing the experimental data with the predictions of the three investigated criteria shows that the MTS and modified MERR results match well with the experimental data, whereas the MSED, even in its modified form, yields the least accurate crack growth path predictions.

- The MTS is mathematically the simplest criterion, and gives accurate predictions for both kink angle and effective fracture toughness. However, the criterion is expected to be not practical in cases where there is a potential for crack extension due to shear stresses.

- The MERR criterion in its classical form does not yield good predictions for fracture growth path. However, its modified version, that is based on the decomposition of the ERR into two components, yields highly accurate crack growth path predictions. The MERR is superior to the MTS in the sense that it can also predict crack growth due to shear failure.

- The MSED criterion, even in its modified form, gives highly inaccurate predictions of crack growth. One therefore should avoid using the MSED to predict fracture growth in anisotropic rocks and potentially other anisotropic solids. Note that, as opposed to isotropic materials, for which the SED normally reaches a minimum at the kink angle, in anisotropic materials only the angle of the maximum SED yields reasonable crack kink predictions.

- Unlike the MTS criterion for which no constraint is needed, the normalized tensile-based ERR and SED energy functions must be confined to an interval of validity, where a kink can potentially open: $\Delta u_{\mathrm{n}} \geq 0$ or $\epsilon_\theta \geq 0$. Outside this region, the formation of a kink due to tensile stress is physically impossible.

- Inaccurate predictions of fracture growth paths when T-stress is excluded from fracture growth formulation demonstrate the significant influence of T-stress on fracture growth behavior.

Chapter 3

On the initiation of hydraulic fractures in anisotropic rocks

---

M. Sakha[a], M. Nejati[a], T. Driesner[a]

[a] *Department of Earth Sciences, ETH Zurich, Switzerland*

2023, Published in *International Journal of Rock Mechanics and Mining Sciences*, 169.

3.1 Abstract

This paper addresses hydraulic fracture initiation from an initially notch-free wellbore situated in an anisotropic host rock, where the rock mass is subjected to an in-situ stress state that is also anisotropic in nature. In such conditions, hydraulic fracture initiation is fully characterized by three parameters, namely initiation pressure, initiation orientation, and initiation length. While a strength-based criterion captures only two of these parameters, break-down pressure and orientation, the evaluation of initiation length requires a mixed criterion approach in which both stress and energy conditions are met. We extend the existing mixed criterion formulation for isotropic rocks to also include anisotropic material behaviour. We then investigate how material anisotropy interacts with stress anistropy to determine the break-down pressure as well as the size and orientation of the starter crack. The results show that material anisotropy can overshadow the stress anisotropy, in the sense that it can drive the crack towards the weakest plane. It is demonstrated from a fracture energy perspective that the initiation length cannot

extend as large as the fracture process zone length even when the wellbore size is unrealistically large. The difference between initiation pressures predicted by the mixed criterion and strength-based theory rises as the wellbore size decreases. Based on these observations, applying the mixed criterion is essential especially in relatively small wellbores.

3.2 Introduction

Hydraulic fracturing is the process of creating new fractures in a rock mass via injecting a pressurized fluid. This process can be utilized in geotechnical applications to create highly permeable pathways in shale oil and gas, mining, enhanced geothermal systems (EGS), carbon sequestration projects, wastewater injection plans etc [Peirce, 2015; Doetsch et al., 2018]. Generally, three different mechanisms can be activated by the fluid injection: initiation of new fractures, fracture propagation, and shear-reactivation of existing fractures [Amann et al., 2018; Krietsch et al., 2020a]. This communication investigates fracture initiation in anisotropic rocks, with a focus on tensile opening from an unnotched borehole with impermeable wall.

New fractures initiate once the fluid breaks down the formation, followed by the fracture propagation phase, where the initiated crack propagates in a stable manner within the medium [Shen et al., 2014]. Most studies have investigated fracture initiation from a wellbore by assuming that stress concentrators such as notches created by perforation or pre-existing natural fractures serve as the main initiation points of failure [Zhang et al., 2011; Li et al., 2015; Liu et al., 2015; Zhu et al., 2015; Sesetty and Ghassemi, 2018; Dong and Tang, 2019; Liu et al., 2020]. However, in practice, fractures may initiate from an unnotched wellbore wall, which has only been investigated in few studies, and these mostly focus on isotropic formations [Lecampion, 2012; Li et al., 2016; Li and Jia, 2018]. Rock anisotropy is often a significant characteristic of the formations where permeability enhancement is planned for [Nejati et al., 2020b] and very little quantitative knowledge about its role in fracture initiation from borehole walls is available.

A key aspect of modeling fracture initiation is that the initial breakdown is assumed to result in the instantaneous opening of a crack of a certain length, i.e., the initiation length

l_0. Accurate knowledge of the initiation length is a pre-requisite for correct modeling of the subsequent fracture propagation phase as strong gradients in the near-well stress field will result in different crack paths depending on the starting point of propagation. Very few studies have so far addressed this problem and most previous studies first assumed an arbitrary length for the initial crack and then analyzed the effects of this arbitrary size on the initiation pressure [Zhang et al., 2011; Li et al., 2015; Liu et al., 2015; Zhu et al., 2015; Sesetty and Ghassemi, 2018; Dong and Tang, 2019]. Observations described in Dong and Tang [2019] and Lecampion [2012] revealed that initiation from perforated and intact wellbores ceases to give consistent results concerning the effect of wellbore size in isotropic formations. According to Lecampion's results, the smaller the size of the wellbore, the higher the breakdown pressure. In contrast, Dong and Tang [2019] noted that an initially cracked wellbore with the larger radius faces higher well resistance to initiation, and thus a higher initiation pressure is required. While this inconsistency has remained as a research question for isotropic formations, the literature barely contains similar investigations in anisotropic formations.

Despite an important effect of wellbore size on the initiation pressure, the criteria for crack nucleation from an unnotched wellbore often ignore such size effects [Bazant, 2000; Carter et al., 1992; Carter, 1992; Lecampion, 2012]. In the framework of fracture initiation, one of the most notable criteria is the maximum tensile stress, which postulates that the onset of breakdown occurs when the maximum hoop stress reaches the material's tensile strength σ_{T} [Hubbert and Willis, 1957]. This strength-based criterion does not give any information on the length of the initiated crack which instantaneously appears in a previously unnotched body. Assuming the sole strength-based criterion, there is no condition to control that the tensile crack to what extent extends, and thus one must provide an estimate for the initiation length. Such an estimate can, for example, be based on linear elastic fracture mechanics (LEFM) theory, which would associate the length of the starter crack to Irwin's material lengthscale $l_{\mathrm{m}} = K_{\mathrm{Ic}}^2/\sigma_{\mathrm{T}}^2$, where K_{Ic} and σ_{T} respectively represent the material's mode I fracture toughness and tensile strength [Carter et al., 1992]. When a stress-based criterion is employed, the wellbore size effects on breakdown pressure cannot be captured, and this leads to unrealistically low initiation pressure predictions for large material lengthscales [Lecampion, 2012]. To reproduce the size effect, Lecampion [2012] and Zhou et al. [2021] proposed mixed criteria by combining the strength-based criterion with an auxiliary condition, respectively, introduced by the energy-based criterion and the toughness of the material. The proposed criteria, though only in the isotropic formations, provide measures for the breakdown pressures and initiated crack lengths that is shown to match well with experimental results [Lecampion, 2012].

In this study, we extend the mixed criterion to anisotropic media, and derive the formulation for a hydraulic fracture initiating from an intact wellbore in an anisotropic formation. We analyze a wellbore that is oriented along the isotropy plane of a formation with transversely isotropic behavior. This configuration represents an endmember case with the material anisotropy from the weakest to the strongest direction within the plane perpendicular to the wellbore. Such geometry along with the assumption on the stress configuration allows to consider a plane elasticity problem, with hydraulic fractures initiating radially under a biaxial stress state. We seek to explore how the initiation parameters, i.e. the dimensionless initiation pressure Π_{b0}, the dimensionless initiation length δ_0 and the initiation angle θ_0, are influenced by different configurations of material anisotropy, stress anisotropy, and the wellbore size.

3.3 Problem description

We aim at analyzing the instantaneous, radial initiation of a tensile crack at the wall of an unnotched wellbore into an anisotropic rock formation. In order to treat a case with maximum material anisotropy in the plane perpendicular to the well, we assume the wellbore lies within the isotropy plane of a transversely isotropic rock formation and we assume that both of material principal directions lie within the plane perpendicular to the wellbore, as schematically shown in Figure 3.1. The stress state must favor radial initiation while hampering formations of non-radial cracks. It should be noted that in some configurations such as the case of a wellbore aligned with the minimum in-situ stress, non-radial mechanism prevails radial initiation (following the geomechanics convention, compressive stresses are taken positive). For non-radial initiation to be suppressed, the stress configuration subjected to radial initiation condition must yield an initiation pressure less than that predicted by the non-radial condition. Assuming the plane-stress condition near the wellbore [Hubbert and Willis, 1957], the initiation of two symmetrically opposite radial

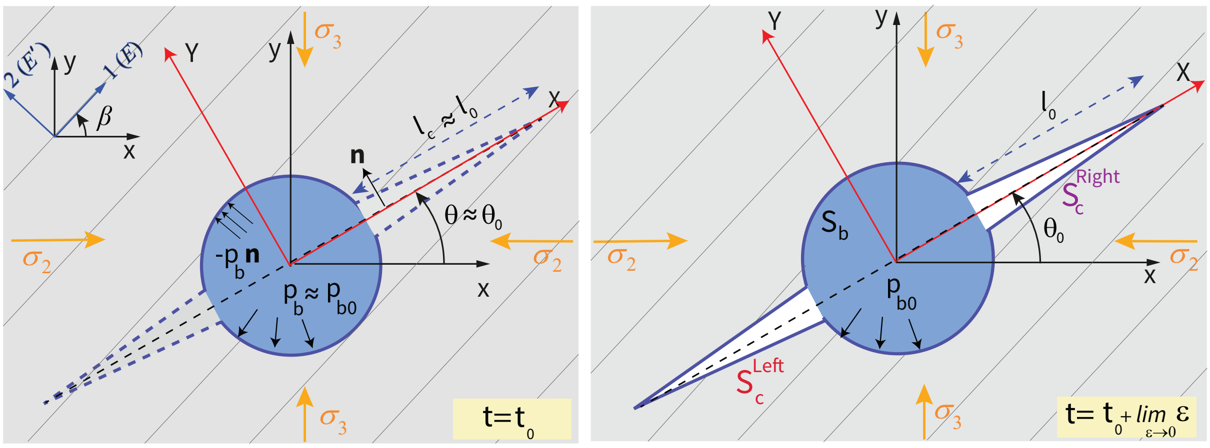

(a) (b)

Figure 3.1: A sketch of the configuration governing the initiation problem from an unnotched wellbore wall. (a) the potential crack at the instant before initiation (b) the instantaneous formation of the initial cracks when pressure reaches p_{b0}. Note that the parallel grey lines inclined at the angle β indicate the orientation of the isotropy planes of the formation and the direction 2 is aligned with the symmetry axis of the material.

cracks is guaranteed, and no additional condition on the stress states is necessary (see Figure 3.1).

To preclude the possibility of shear-reactivation, the stress states must be studied not to favor any types of faulting. In the framework of Mohr diagrams, the stress ratios whose Mohr's circles touch the failure line, can provoke shearing in rock. Assuming the Mohr-Coulomb envelop as the failure line, the first touch necessarily corresponds to the (σ_1, σ_3) Mohr's circle and thus only the ratio of σ_1/σ_3 needs to be taken care of. Once the Mohr-Coulomb condition determines the greatest ratio of σ_1/σ_3, the condition can also provide the extreme values of the intermediate stress σ_2 since it can neither surpass σ_1 nor fall below σ_3. Therefore, the stress anisotropy defined as $\lambda = \sigma_2/\sigma_3$ remains finite within a range varying from unity to the greatest ratio of σ_1/σ_3.

Figure 3.1 schematically depicts the problem of initiation around an initially notch-free cylindrical wellbore. The parallel lines inclined at the angle β indicate the orientation of the isotropy planes of the formation. As shown in this figure, the hydraulic fracture instantaneously initiates at a previously unnotched wellbore once the fluid is pressurized beyond the initiation pressure $p_{\mathrm{b}0}$. At the instant of initiation, the geometry of the initiated fracture is characterized by the initiation length l_0 as well as the initiation orientation θ_0. Therefore, in order to fully characterize hydraulic fracture initiation, the initiation criterion must capture the initiation parameters, i.e., the fluid pressure, the length and the orientation of the crack at initiation. It is important to bear in mind that the analysis ignores the poroelastic effect by assuming the rock formation impermeable.

3.4 Initiation criteria

The analysis of initiation requires the prediction of the initiation length as well as the initiation direction if anisotropy is present at the rock. We are therefore interested in a robust criterion that is able to fully capture the initiation parameters in an anisotropic medium.

3.4.1 Strength-based criterion

A purely strength-based model postulates that hydraulic fractures initiate once the wellbore pressure overcomes the tensile strength of the host rock. This implies that the hoop stress σ_θ [1] exceeds the material tensile strength σ_{T} along the initiation direction θ_0. This criterion was first introduced by Hubbert and Willis [1957] to predict longitudinal fracture initiation in isotropic solids, and has widely been adopted thereafter. This criterion for an anisotropic medium with direction-dependent tensile strength $\sigma_{\mathrm{T}}(\phi)$, is formulated as [Serajian and Ghassemi, 2011; Li and Weijermars, 2019]

$$\begin{cases} \dfrac{d\hat{\sigma}_\theta(p_{\mathrm{b}},\theta)}{d\theta}|_{(p_{\mathrm{b}0},\theta_0)} = 0, \quad \dfrac{d^2\hat{\sigma}_\theta(p_{\mathrm{b}},\theta)}{d\theta^2}|_{(p_{\mathrm{b}0},\theta_0)} < 0, \quad \left(\hat{\sigma}_\theta(p_{\mathrm{b}},\theta) = \dfrac{\sigma_\theta(p_{\mathrm{b}},\theta)}{\sigma_{\mathrm{T}}(\phi)}\right), \\ \\ \hat{\sigma}_\theta(p_{\mathrm{b}0},\theta_0) = 1, \end{cases} \tag{3.1}$$

---

[1] Following the approach used by Lecampion [2012], the stress distribution components around the wellbore is expressed with the convention of positive stresses in tension. It is important to keep in mind that this differs from the geomechanical convention used to express in-situ compressive stresses.

where ϕ is a function of θ as well as the material principal orientation β and will be defined later in Section 3.5.

Eq. 3.1 states that the crack initiates once the normalized hoop stress, $\hat{\sigma}_\theta$, reaches its maximum on the wellbore wall. In reality, however, a tensile crack with a finite extent instantaneously appears in the previously notch-free body. This abrupt jump from a crack-free to a cracked state as well as the corresponding crack length needs to be captured within the framework of initiation formulation. In this context, the crack may favor being extended to the full length of the fracture process zone (FPZ). However, the correct initiation length depends also on other parameters such as the stress anisotropy and the wellbore size [Lecampion, 2012]. As these are not included in the purely strength-based theory, the latter cannot therefore provide the initiation length, and the length of the potential crack at the instant of initiation remains unclear. To address this drawback, an energy condition must also be met.

3.4.2 Mixed criterion: strength and energy

An energy-based criterion for crack initiation requires that the cohesion in the rock material debonds once the energy release rate is large enough to create the starter crack surfaces. Although the strength-based and energy-based criteria are each necessary conditions for the problem, only the combination of these two allows to determine all parameters involved in the hydraulic fracture initiation. The mixed criterion therefore entails the two following conditions if the hydraulic fracture is to initiate: 1) the hoop stress at the tip of the yet to be initiated crack becomes maximum and exceeds the material strength; and 2) the incremental energy release rate between the cracked and crack-free states reaches the critical energy release rate (fracture energy) of the material $\mathcal{G}_{\mathrm{Ic}}$ [Lecampion, 2012]. One can therefore formulate the mixed criteria for the anisotropic formations as

$$\begin{cases} \dfrac{d\hat{\sigma}_\theta(p_{\mathrm{b}}, l_{\mathrm{c}}, \theta)}{d\theta}|_{(p_{\mathrm{b0}}, l_0, \theta_0)} = 0, \quad \dfrac{d^2\hat{\sigma}_\theta(p_{\mathrm{b}}, l_{\mathrm{c}}, \theta)}{d\theta^2}|_{(p_{\mathrm{b0}}, l_0, \theta_0)} < 0, \quad \left(\hat{\sigma}_\theta(p_{\mathrm{b}}, l_{\mathrm{c}}, \theta) = \dfrac{\sigma_\theta(p_{\mathrm{b}}, l_{\mathrm{c}}, \theta)}{\sigma_{\mathrm{T}}(\phi)}\right), \\ \hat{\sigma}_\theta(p_{\mathrm{b0}}, l_0, \theta_0) = 1, \\ \mathcal{G}_{\mathrm{inc}}(p_{\mathrm{b0}}, l_0, \theta_0) = \mathcal{G}_{\mathrm{Ic}}(\phi). \end{cases} \tag{3.2}$$

Again all the material properties incorporated in mixed criterion (i.e. the tensile strength $\sigma_{\mathrm{T}}(\phi)$ and the fracture energy $\mathcal{G}_{\mathrm{Ic}}$), are assumed to be direction-dependent. These three conditions must be fulfilled simultaneously to obtain the three unknowns of breakdown pressure p_{b0}, initiation length l_0, and initiation angle θ_0. The methodology applied to solve these coupled equations governing the mixed criterion, is described in Section 3.7.

3.5 Rock anisotropy

Anisotropy in mechanical properties is often introduced to the rock during the formation of features such as bedding or foliation. As a result, pores, micro-cracks and the constituent minerals are dominantly oriented along the foliation and bedding planes within which the material behaves isotropic. Therefore, transverse isotropy is often an appropriate material model to characterize the elasticity of many anisotropic rocks.

In this study, we adopt the following convention: the isotropy plane (direction 1) and the plane normal to it (direction 2) form two principal material directions. Let us define the direction-dependent mechanical properties as follows: I) E and E' are respectively the Young's moduli along direction 1 and direction 2; II) ν and ν' respectively denote the Poisson's ratios within and normal to the isotropy plane, while G' is the shear modulus within the plane; III) $K_{\mathrm{Ic,i}}$ is the mode I fracture toughness value along direction $\mathrm{i} = 1, 2$; IV) $\sigma_{\mathrm{T,i}}$ stands for the tensile strength along direction $\mathrm{i} = 1, 2$. To describe the degree of anisotropy, we also define the following ratios: I) $\xi = E/E'$ is the anisotropy ratio of Young's modulus; II) $\gamma_{\mathrm{t}} = \sigma_{\mathrm{T,2}}/\sigma_{\mathrm{T,1}}$ denote anisotropy in tensile strength; III) fracture toughness anisotropy read as $\gamma_{\mathrm{K}} = K_{\mathrm{Ic},2}/K_{\mathrm{Ic},1}$. The ratios ξ, γ_{t}, γ_{K} are usually taken greater than unity since in transversely isotropic rocks, the material is typically weaker along the isotropy plane. For the sake of simplicity, in this study the anisotropy ratio of apparent shear modulus defined as $\eta = G'/G'_{\mathrm{sv}}$ is taken as unity, where G'_{sv} is the transverse shear modulus approximated from the Saint-Venant relation [Nejati et al., 2019b]: $1/G'_{\mathrm{sv}} = 1/E + (1 + 2\nu')/E'$.

The mechanical properties of the rock material are assumed to be dependent on ϕ which is the angle between the initiated fracture and the principal direction 1: $\phi = \theta_0 - \beta$ (see Figure 3.1). Table 3.1 lists the directional dependence of the failure properties required for the mixed-criteria. Nejati et al. [2020b] showed through experimental data that the mode I fracture toughness K_{Ic} values follow a sinusoidal curve between the principal values $K_{\mathrm{Ic},1}$ and $K_{\mathrm{Ic},2}$. Similar to fracture toughness, the tensile strength $\sigma_{\mathrm{T}}(\phi)$ is also assumed to follow a sinusoidal variation between the two principal directions. To fully characterize the material behavior, the direction dependence of the critical mode I energy release rate, $\mathcal{G}_{\mathrm{Ic}}$, is also needed, which is presented in Table 3.1 Nejati et al. [2020b].

Tension-based material property	Variation against ϕ
Strength-σ_{T}	$\sigma_{\mathrm{T}}(\phi) = \sigma_{\mathrm{T},1}\cos^2\phi + \sigma_{\mathrm{T},2}\sin^2\phi$
Fracture toughness -Critical SIF-K_{Ic}	$K_{\mathrm{Ic}}(\phi) = K_{\mathrm{Ic},1}\cos^2\phi + K_{\mathrm{Ic},2}\sin^2\phi$
Fracture toughness -Critical ERR-$\mathcal{G}_{\mathrm{Ic}}$	$\mathcal{G}_{\mathrm{Ic}}(\phi) = \dfrac{K^2_{\mathrm{Ic}}(\phi)}{2E}\left(\kappa_2\left(\xi + \sqrt{\xi}\right)\cos^2\phi + \kappa_1\left(\sqrt{\xi} + 1\right)\sin^2\phi\right)$

Table 3.1: The directional dependence of the material tensile strength and the different measures of fracture toughness in tensile-based failure mechanisms, adopted from Nejati et al. [2020b, 2021b]. Here, $\xi = E/E'$ is the anisotropy ratio of Young's modulus, $\kappa_1 = \kappa_2 = 1$ for the plane-stress condition and $\kappa_1 = 1 - \nu^2$, $\kappa_2 = 1 - \xi\nu'^2$, for the plane-strain condition.

It should be noted that this study assumes that the material properties are stress independent and taken as constants, however, many studies have shown that the mechanical properties of rocks can be strongly dependent on the stress level, particularly at lower stress levels [Nejati et al., 2019b; David et al., 2012]. This is caused by the formation of micro-cracks and voids during the unloading process when rock samples are extracted from a well, unlike the in-situ conditions. At high stress levels, these micro-cracks and voids close, leading to stabilization moduli and stress-independence. However, the stress level in this current study is not high enough to make the elastic properties stress-independent, but rather in a range where linear stress dependency is more expected [Nejati et al., 2019b]. Additionally, the degree of rock anisotropy can be affected by higher confining stress, meaning that at higher stress anisotropy, the material behaves more isotropically [Thongprapha et al., 2022]. This study does not take into account such effects, which should be acknowledged as limitations in terms of its applicability to real-world scenarios.

3.6 Elasticity problem

We now turn our attention to describe the stress-deformation field in the vicinity of a wellbore. As shown in Figure 3.2a, the following boundary conditions govern the initiation of a potential crack driven by fluid pressure p_b:

$$\begin{aligned}
&\boldsymbol{\sigma}\cdot\mathbf{n} = -p_\mathrm{b}\mathbf{n}, \quad \text{on} \quad S_\mathrm{b} \\
&\boldsymbol{\sigma}\cdot\mathbf{n} = \mathbf{0}, \quad \text{on} \quad S_\mathrm{c}^\mathrm{Right} \;\&\; S_\mathrm{c}^\mathrm{Left} \\
&\mathbf{u}^+ - \mathbf{u}^- = \begin{pmatrix} \mathbf{u}_\mathrm{r}^+ - \mathbf{u}_\mathrm{r}^- \\ \mathbf{u}_\theta^+ - \mathbf{u}_\theta^- \end{pmatrix} = \begin{pmatrix} \psi \\ \omega \end{pmatrix} \\
&\lim_{r\to\infty} \boldsymbol{\sigma} = \begin{pmatrix} -\sigma_2 & 0 \\ 0 & -\sigma_3 \end{pmatrix},
\end{aligned} \tag{3.3}$$

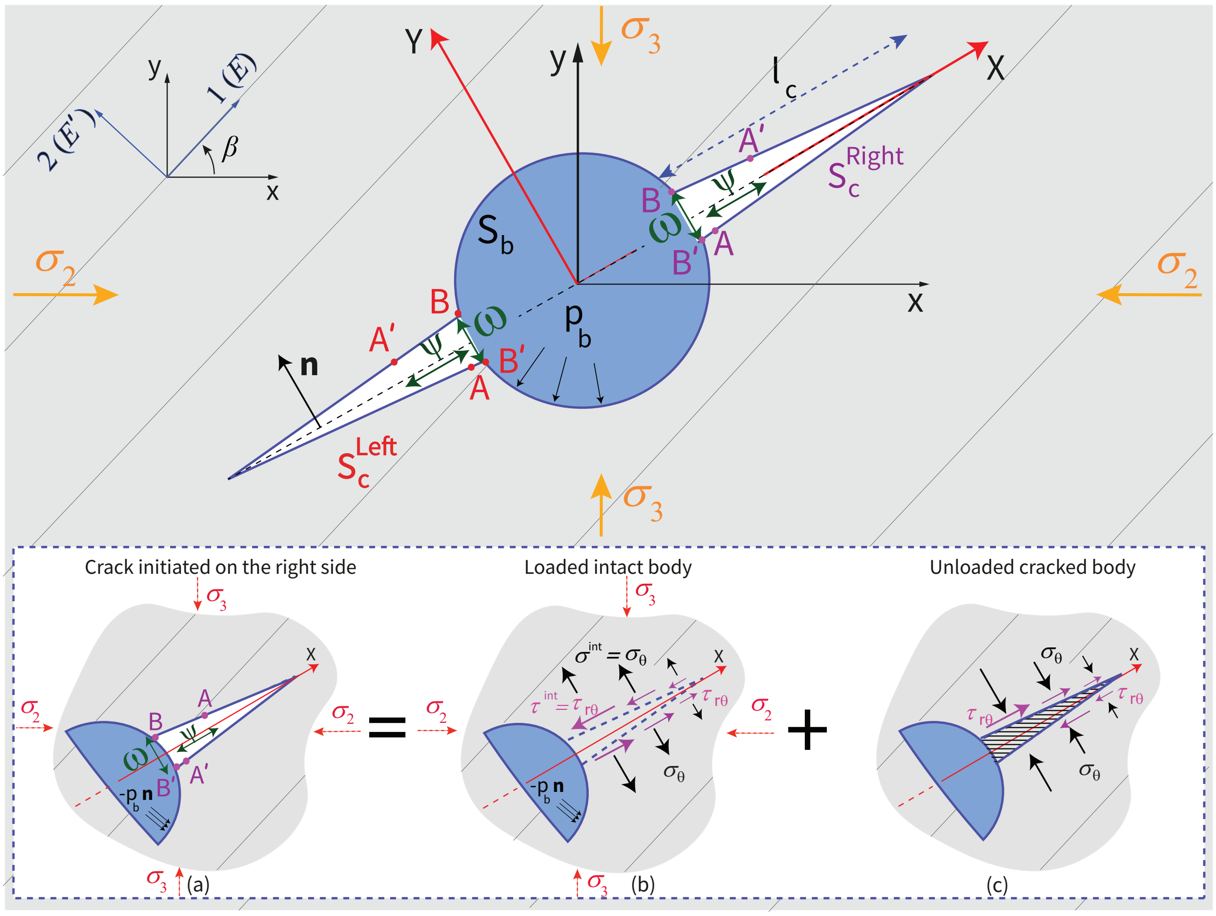

Figure 3.2: Two symmetrical cracks radially emanating from a cylindrical wellbore subjected to in-situ compressive stresses. (a) Implementation of Bueckner's theorem based on superposition of loaded intact body (b), and unloaded cracked body (c).

Here, S_{b} denotes the wellbore surface, while $S_{\mathrm{c}}^{\mathrm{Right}}$ and $S_{\mathrm{c}}^{\mathrm{Left}}$ refer to the crack surfaces formed on the right and left sides of the wellbore, respectively. On either side of the wellbore, adjacent points along the crack line experience a sudden jump in the displacement field $\mathbf{u}$ (see the point sets AA′ and BB′ in Figure 3.2a). The discontinuities arising along and across the crack line are respectively associated with the tangential displacement ψ and crack opening ω. Note that contrary to the geomechanics convention, Eq. 3.3 takes the tensile stresses as positive values.

Application of the mixed criterion requires the assumption of the process zone length to be traction-free. This clarifies why the cohesive force along the potential crack face is taken equal to zero in Eq. 3.3. Although this assumption is physically plausible in brittle materials, in which the size of the fracture process zone (FPZ) is negligible, the cohesive force cannot be neglected in quasi-brittle materials such as rocks. In rock materials, the cohesive force along the FPZ can be described by different softening models limited to the following extreme cases: I) the Dugdale cohesive zone model that assumes a constant traction with no softening behavior; II) the mixed criterion that employs the traction-free condition along the FPZ. Lecampion [2012] showed that initiation parameters predicted by these two limiting cases are in a good agreement for a specific range of Irwin's numbers. Taking Irwin's number as the ratio of the FPZ length to the wellbore size, Lecampion [2012] revealed that applicability of the mixed criterion to quasi-brittle materials is for Irwin's numbers ranging between $[0.1 - 10]$. In practice, this range is most likely to exist for many real-world applications, and thus we must restrict the analysis of initiation in rocks to this range.

To solve the crack problem, we now invoke the Bueckner's theorem which requires the superposition of the two following problems: 1) The stresses arising in the intact body (i.e. σ^{int} and τ^{int} along the crack line as shown in Figure 3.2b and given in detail in B.1); 2) The stresses induced by the distribution of dislocations along the crack in the unloaded body and described by opposite tractions $-\sigma^{\mathrm{int}}\mathbf{n}$ and $-\tau^{\mathrm{int}}\mathbf{n}$ to those produced by the applied loading (see Figure 3.2c) [Hills et al., 1996]. In the following, we discuss how the elasticity solution for the unloaded cracked body can be obtained.

At the moment of initiation, the pressurized fluid has not yet infiltrated in the starter crack. Therefore, the traction-free crack face condition requires the superposition of the loaded intact body together with an unknown distribution of dislocation in which the induced tractions (sometimes also referred to as corrective tractions) yield the traction-free condition along the crack [Hills et al., 1996]. Assuming unknown densities B_{X} and B_{Y}, respectively, for the glide and climb dislocations, the combination of unknown density vectors must recover the crack geometry described by the shear displacement ψ and the crack opening ω. For the unloaded body, one can read the elastic problem as

$$
\begin{aligned}
&\boldsymbol{\sigma}\cdot\mathbf{n}=\mathbf{0}, \quad \text{on} \quad S_{\mathrm{b}} \\
&\mathbf{t}=\begin{cases}\mathbf{t}_r=\tau_{r\theta}\mathbf{n} & =-\tau^{\mathrm{int}}\mathbf{n} \\ \mathbf{t}_\theta=\sigma_\theta\mathbf{n} & =-\sigma^{\mathrm{int}}\mathbf{n}\end{cases}, \qquad \text{on} \quad S_{\mathrm{c}}^{\mathrm{Right}} \;\&\; S_{\mathrm{c}}^{\mathrm{Left}} \\
&\mathbf{u}^{+}-\mathbf{u}^{-}=\begin{pmatrix}\mathbf{u}_{\mathrm{r}}^{+}-\mathbf{u}_{\mathrm{r}}^{-} \\ \mathbf{u}_\theta^{+}-\mathbf{u}_\theta^{-}\end{pmatrix}=\begin{pmatrix}\psi \\ \omega\end{pmatrix} \\
&\lim_{r\to\infty}\boldsymbol{\sigma}=\begin{pmatrix}0 & 0 \\ 0 & 0\end{pmatrix}.
\end{aligned}
\tag{3.4}
$$

To determine the unknown distribution of dislocation, we make use of the boundary integral equation which establishes the relationship between the corrective stresses and the unknown density components. In doing so, we incorporate the relationship between the geometry and dislocation components read as $B_{\mathrm{X}}=-\partial\psi/\partial\boldsymbol{X}_{01}$ and $B_{\mathrm{Y}}=-\partial\omega/\partial\boldsymbol{X}_{01}$. The negative sign in this definition implies that insertion of positive dislocation densities along the axis X decreases opening and shear displacements. Using the boundary integral equation, we have [Hills et al., 1996]

$$
-\begin{pmatrix}\tau_{r\theta}(X) \\ \sigma_\theta(X)\end{pmatrix}-\frac{E}{\pi}\int_{R-l_{\mathrm{c}}}^{R+l_{\mathrm{c}}}\boldsymbol{H}(X,\boldsymbol{X}_{01})\begin{pmatrix}-\dfrac{\partial\psi}{\partial\boldsymbol{X}_{01}} \\ -\dfrac{\partial\omega}{\partial\boldsymbol{X}_{01}}\end{pmatrix}\mathrm{d}\boldsymbol{X}_{01}=0\,. \tag{3.5}
$$

Here, the kernel matrix $\boldsymbol{H}(X,\boldsymbol{X}_{01})$ denotes the stresses induced by a unit edge dislocation vector located at the core $(\boldsymbol{X}_{01},\boldsymbol{X}_{02}=0)$. Nevertheless, due to the problem symmetry, the effect of the symmetric dislocations can be considered on each crack wing by introducing the matrix $\boldsymbol{J}(X,\boldsymbol{X}_{01})$ as $\boldsymbol{J}(X,\boldsymbol{X}_{01})=\boldsymbol{H}(X,\boldsymbol{X}_{01})-\boldsymbol{H}(X,-\boldsymbol{X}_{01})$. Using integration by parts and applying the condition of zero opening and shearing at the crack tip, Eq. 3.5 is re-written as

$$
\begin{pmatrix}\tau_{r\theta}(X) \\ \sigma_\theta(X)\end{pmatrix}+\frac{E}{\pi}\int_{R}^{R+l_{\mathrm{c}}}\frac{\partial\boldsymbol{J}(X,\boldsymbol{X}_{01})}{\partial\boldsymbol{X}_{01}}\begin{pmatrix}\psi \\ \omega\end{pmatrix}\mathrm{d}\boldsymbol{X}_{01}=0. \tag{3.6}
$$

where the definition of the matrix components $\boldsymbol{J}_{\mathrm{ij}}(z,z_0)$ on the plane $Y=0$ is given in detail in B.2. Adopting the stress distributions defined for the intact body in B.1, the shear and opening displacements can be determined numerically using the displacement discontinuity method (DDM) [Crouch and Starfield, 1983], and we are therefore able to measure the elastic potential energy due to the stresses induced along the crack. Recalling the relations given in Eq. 3.4, the elastic potential energy $\bar{P}$ along one of the crack wings in the unloaded body can be expressed as

$$\bar{P} = -\frac{1}{2}W = -\frac{1}{2}\int_{S'_{\mathrm{c,R}}} -\mathbf{t}\cdot(\mathbf{u}^{+}-\mathbf{u}^{-})\mathrm{d}S = -\int_{R}^{R+l_{\mathrm{c}}}(\sigma^{\mathrm{int}}(X)\omega(X)+\tau^{\mathrm{int}}(X)\psi(X))\mathrm{d}X. \tag{3.7}$$

The total elastic potential energy P, however, is composed of $\bar{P}$ plus the elastic potential energy of the intact body. Nevertheless, the identical elastic potential energies of the intact body between the two states cancel each other in the calculation of the incremental energy release rate $\mathcal{G}_{\mathrm{inc}}$. Excluding the contribution due to the release of the shear stress, one can therefore formulate the incremental energy release rate $\mathcal{G}_{\mathrm{inc}}$ as

$$\mathcal{G}_{\mathrm{inc}}(p_{\mathrm{b}}, l_{\mathrm{c}}, \theta) = \frac{1}{2l_{\mathrm{c}}}\int_{R}^{R+l_{\mathrm{c}}}\sigma^{\mathrm{int}}(X)\omega(X)\mathrm{d}X \tag{3.8}$$

3.7 Solution algorithm and non-dimensionalization

To ensure that our analysis does not represent a specific class of initiation problems, we now re-present the equations discussed before in non-dimensional form. To do so, the quantities are scaled as follows: 1) The lengthscales by the wellbore radius, $L^{*} = R$; 2) The stresses by the tensile strength of the material in principal direction 1, $P^{*} = \sigma_{\mathrm{T},1}$; 3) The crack opening and shearing by the expression $R\sigma_{\mathrm{T},1}/E$. According to this non-dimensionalization, the mixed criterion can be expressed as

$$\begin{cases} \dfrac{d\hat{\sigma}_\theta(\Pi_\mathrm{b},\delta,\theta)}{d\theta}|_{(\Pi_{\mathrm{b}0},\delta_0,\theta_0)}=0, \quad \dfrac{d^2\hat{\sigma}_\theta(\Pi_\mathrm{b},\delta,\theta)}{d\theta^2}|_{(\Pi_{\mathrm{b}0},\delta_0,\theta_0)}<0, \quad \left(\hat{\sigma}_\theta(\Pi_\mathrm{b},\delta,\theta)=\dfrac{\sigma_\theta(\Pi_\mathrm{b},\delta,\theta)}{\sigma_\mathrm{T}(\phi)}\right), \\ \hat{\sigma}_\theta(\Pi_{\mathrm{b}0},\delta_0,\theta_0)=1, \\ \hat{\mathcal{G}}_\mathrm{inc}(\Pi_{\mathrm{b}0},\delta_0,\theta_0)=\mathcal{I}f(\phi). \end{cases} \tag{3.9}$$

Here, $\Pi_{\mathrm{b}0}$ and δ_0 respectively denote the dimensionless initiation pressure and length, and $\mathcal{I}$ stands for Irwin's number defined by $\mathcal{I}=K_{\mathrm{Ic},1}^2/(R\sigma_{\mathrm{T},1}^2)$. Recalling the directional dependence of K_Ic and $\mathcal{G}_\mathrm{Ic}$ reported in Table 3.1, the function $f(\phi)$ is developed to the following form:

$$f(\phi)=\frac{1}{2}\left(\cos^2\phi+\gamma_\mathrm{K}\sin^2\phi\right)^2\left(\kappa_2(\xi+\sqrt{\xi})\cos^2\phi+\kappa_1(1+\sqrt{\xi})\sin^2\phi\right). \tag{3.10}$$

Moreover, the incremental energy release rate given by Eq. 3.8 is non-dimensionalized as

$$\hat{\mathcal{G}}_\mathrm{inc}(\Pi_\mathrm{b},\delta,\theta)=\frac{1}{2\delta}\int_1^{1+\delta}\tilde{\sigma}_\theta(\boldsymbol{\mathcal{X}}_1)\Omega(\boldsymbol{\mathcal{X}}_1)\mathrm{d}\boldsymbol{\mathcal{X}}_1, \tag{3.11}$$

where the unknown geometry factors Ψ (: dimensionless shear displacement) and Ω (: dimensionless crack opening) are simultaneously obtained by solving the boundary integral equation non-dimensionalized as

$$\begin{pmatrix} \tilde{\tau}_{\mathrm{r}\theta}(\boldsymbol{\mathcal{X}}_1) \\ \tilde{\sigma}_\theta(\boldsymbol{\mathcal{X}}_1) \end{pmatrix}+\frac{1}{\pi}\int_1^{1+\delta}\frac{\boldsymbol{J}(\boldsymbol{\mathcal{X}}_1,\boldsymbol{\mathcal{X}}_{01})}{\partial\boldsymbol{\mathcal{X}}_{01}}\begin{pmatrix}\Psi\\ \Omega\end{pmatrix}\mathrm{d}\boldsymbol{\mathcal{X}}_{01}=0. \tag{3.12}$$

Note that in Eqs. 3.11 and 3.12, both the dimensionless stresses $\tilde{\sigma}_\theta$ and $\tilde{\tau}_{\mathrm{r}\theta}$ are defined in the dimensionless coordinate system $\boldsymbol{\mathcal{X}}_1\boldsymbol{\mathcal{X}}_2$, and normalized by the material tensile strength along the weakest plane, or $\sigma_{\mathrm{T}1}$.

As mentioned in Section 3.4, the three conditions in 3.12 are coupled and must be solved simultaneously. Owing to the inherent nonlinearity of the resulting system of equations, a combination of the bisection method and the Newton–Raphson iterative algorithm is implemented to find the root (i.e. $\Pi_{\mathrm{b0}}, \delta_0$, and θ_0) in such a way that all the above conditions are met. In doing so, we first confine the initial interval to the bounds Π_{b1} and Π_{b2} ($\Pi_{\mathrm{b1}} < \Pi_{\mathrm{b2}}$) at which two types of inequality for the third condition are reached; while the lower bound reads the inequality as $\hat{\mathcal{G}}_{\mathrm{inc}}(\Pi_{\mathrm{b1}}, \delta, \theta) < \mathcal{I} f(\phi)$, the incremental energy release rate for the upper bound goes beyond the critical energy release rate $\mathcal{I} f(\phi)$. This ensures that by repeatedly bisecting the pressure interval, we approach the initiation pressure provided that other conditions are also met. Therefore, at each pressure, we apply the Newton–Raphson iterative algorithm to the first two conditions in order to obtain the corresponding initiation length and angle. To set the starting point Π_{b1}, one can choose the initiation pressure, predicted for a vanishingly small initiation length, which is very close to the pressure obtained by applying solely the strength-based criterion (i.e. the initiation pressure p_{b0} determined by Eq. 3.1 and known as $\Pi_{\mathrm{strength}} = p_{\mathrm{b0}}/\sigma_{\mathrm{T},1}$).

3.8 Results and discussion

To validate the correctness of the mixed criterion formulation in anisotropic formations, we compare the results in the isotropic limit $\mu_{\mathrm{j}} \to i$ ($\mathrm{j} = 1, 2$) to the results given by Lecampion [2012] under the plane-strain condition. Figure 3.3 illustrates the variations of the initiation pressure and initiation length as a function of Irwin's number when the stress anisotropy is absent (i.e. $\lambda = 1$). This figure includes two sets of results obtained as follows. 1) Lecampion: here, it is assumed that the formation is isotropic, and thus we adopt the stress field and the kernel function associated with the isotropic behaviour as given in Lecampion [2012]; 2) Present study: we adopt the stress field and the kernel matrix corresponding to the anisotropic case, where the isotropic case can be simply reached as the conjugate complex roots approach i. Figure 3.3 demonstrates that the stress-displacement field which governs fracture initiation in anisotropic solids approaches the results of the isotropic material behaviour in the limiting case.

It is important to note that the validity of the mixed criterion formulation in the

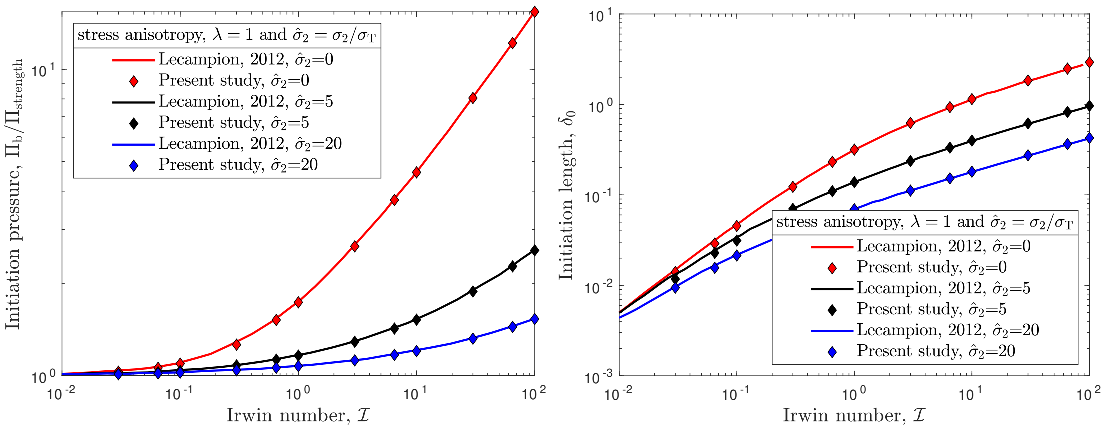

Figure 3.3: Comparison of the wellbore initiation pressure and length as a function of Irwin's number $\mathcal{I}$ estimated by the mixed criterion applied to the isotropic formation under different values for the dimensionless far-field compressive mean stress; isotropy is originally assumed by directly applying the isotropic relations [Lecampion, 2012] or approached by taking limit of the relations corresponding to anisotropic solids.

anisotropic case cannot be solely determined through comparison with the results of the isotropic case. This is because isotropic materials do not depend on β, and therefore, such a comparison cannot ensure that the adopted kernel matrix can accurately describe initiation at any level of material anisotropy. To address this, we have further strengthened the validation of the formulation by comparing the initiation parameters given in Section 3.8.1 with those obtained through finite element analysis [Sakha et al., 2023].

3.8.1 Anisotropy effect on the initiation parameters

To understand how anistropy in the material and the stress state can affect the initiation parameters (i.e. the initiation pressure, and the direction and the length of the initiated crack), we define three sets of loading λ at a fixed geometry and vary the material anisotropy ratios as well as the orientation β at each set. Adopting the perturbed stress states from Dutler et al. [2020], the loading ratio λ ranges from unity to the greatest ratio of $\sigma_1/\sigma_3 = 2$, as this meets the requirements of radial initiation and the Mohr-Coulomb condition (see Section 3.3). In compliance with this limited range, we assume that a wellbore with the constant radius of $R = 8$ cm is subjected to the three different sets of loading: $\lambda = 1, 1.5, 2$ under the plane stress condition. Besides the stress anisotropy, the

Loading state				Material properties					
				Fracture toughness		Strength		Elastic modulus $\times 10^3$	
σ_3	$\sigma_2 = \sigma_3$	$\sigma_2 = 1.5\sigma_3$	$\sigma_2 = \sigma_1 = 2\sigma_3$	$K_{\mathrm{Ic},1}$	$K_{\mathrm{Ic},2} = \gamma_{\mathrm{K}} K_{\mathrm{Ic},1}$	$\sigma_{\mathrm{T},1}$	$\sigma_{\mathrm{T},2} = \gamma_{\mathrm{t}} \sigma_{\mathrm{T},1}$	E'	$E = \xi E'$
6.5	6.5	9.75	13.1	1.56	[1.56 7.80]	5.619	[5.619 $\approx$28.10]	18	[18 90]

Table 3.2: The elastic modulus, strength, and fracture toughness values measured for Grimsel Granite [Nejati et al., 2020b, 2021b]. The strength, stress, and elastic modulus are given in MPa. This table reports size-independent values of fracture toughness in MPa$\sqrt{\mathrm{m}}$. The stress states is also taken from Dutler et al. [2020].

rock anisotropy influences the level of the pressure and the geometry of the crack at the instant of initiation. In transversely isotropic media, the anisotropy ratios ξ, γ_{t}, and γ_{K} along with the orientation of the isotropy plane, β, define the state of material anisotropy. As in most rocks, the ratio of the elastic moduli $\xi = E/E'$ falls in the range $1-5$ [Jaeger et al., 2007], we restrict our analysis to this range of ξ values. For our analysis, we assume that all the material anisotropy ratios can be taken equal, meaning that: $\xi = \gamma_{\mathrm{t}} = \gamma_{\mathrm{K}}$.

Figure 3.4 presents the variations of the initiation parameters as functions of the material anisotropy orientation β for different degrees of material anisotropy. The figure provides the results of the initiation parameters in three different sets of loading, starting with the stress isotropy $\lambda = 1$ in Figure 3.4*a*, and followed by the anisotropy in stress states in Figure 3.4*b* and Figure 3.4*c*. At each set of loading, the variations of the initiation parameters is plotted against the material anisotropy orientation β, and three sets of plots are given: I) Figure 3.4, the top row, depicts the initiation direction θ_0; II) The middle row of Figure 3.4 shows the fluid pressure at the instant of initiation; III) Figure 3.4, the bottom row, indicates the length of the initiated crack normalized by the wellbore radius R. The variable β, measured as the orientation of the weakest plane in a transversely isotropic material, reflects the material resistance against crack initiation along the direction perpendicular to the minimum in-situ stress (i.e. $\theta_0 = 0°$). Depending on the degree of material anisotropy ξ, either the material tendency or the loading anisotropy can control the initiation angle. In the absence of stress anistropy ($\lambda = 1$), however, the crack always initiates along the weakest plane (see the line $\theta_0 = \beta$ in the top plot of Figure 3.4a).

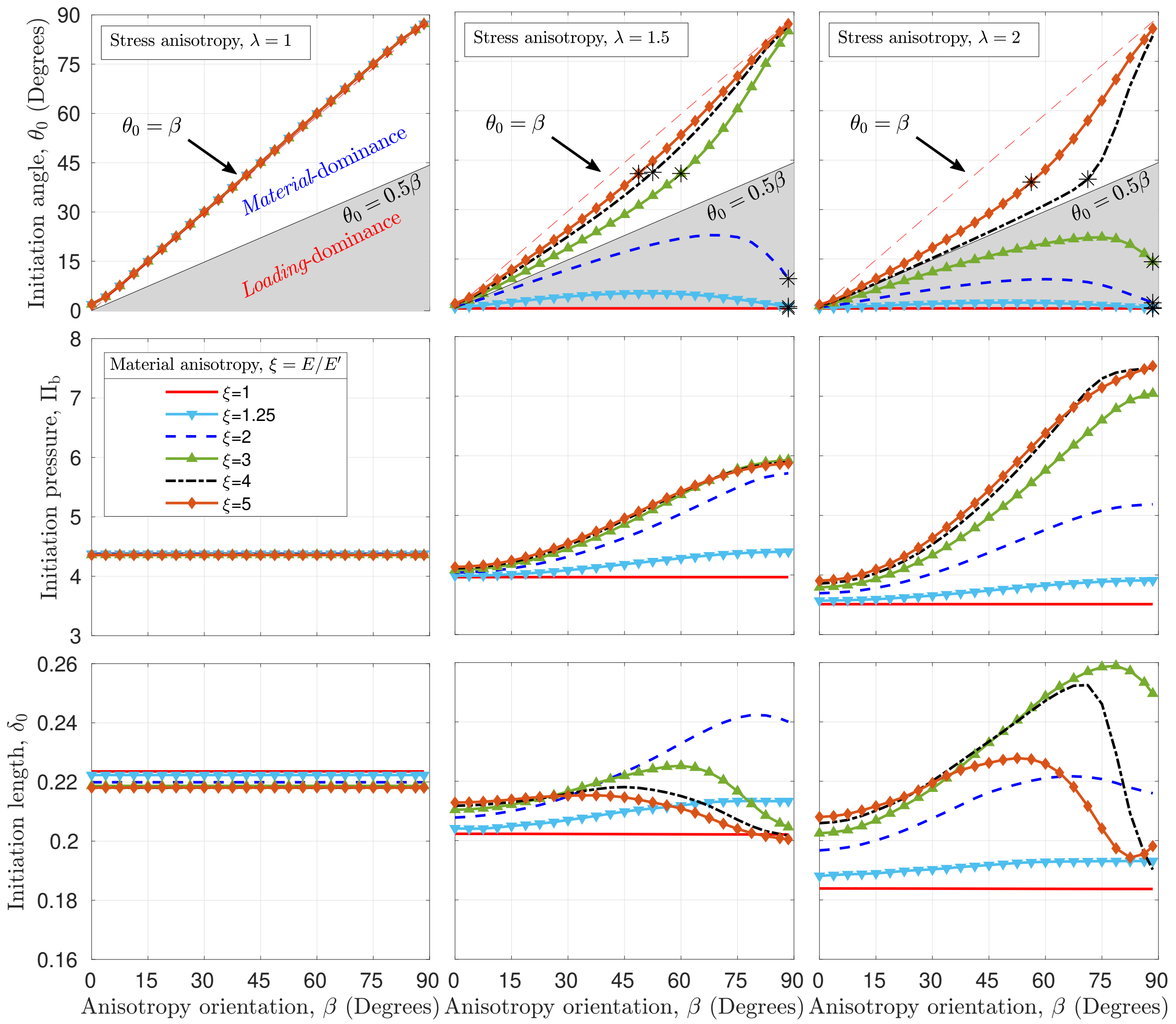

(a) (b) (c)

Figure 3.4: Variations of wellbore initiation parameters as functions of the orientation β for different material and stress anisotropy ratios. Here, Irwin's number $\mathcal{I}$ is kept to a constant value of 0.96. Note that the legend denoting the color code used for each material anisotropy, applies to all subsequent plots. The marker star shows the highest deviation, ϕ_0^* at each material anisotropy when $\lambda \geq 1$. In order to analyze the trend in the data, a Gaussian smoothing technique was applied. This method effectively smoothed the trend while preserving the overall shape of the original data.

Figure 3.4, the top row, illustrates how anistropy in the stress field and the material anisotropy interact to determine the angle of crack initiation. While the anisotropy in material properties tends to drive the initial crack toward the weakest plane (direction 1), the stress anisotropy competes with this tendency in favor of crack formation perpendicular to the minimum in-situ stress. As a result, the initiation angle deviates from the direction at which the crack would initiate in the absence of stress anisotropy, i.e. $\theta_0 = \beta$ (see the top plot of Figure 3.4a). The line $\theta_0 = 0.5\beta$, in Figure 3.4, the top row, marks the transition from the *Material*-dominance to the *Loading*-dominance. Once the deviation i.e., $\phi_0 = |\theta_0 - \beta|$, exceeds 50% of the orientation β (i.e. $\theta < 0.5\beta$), the θ_0-curve becomes concave downward, meaning that initiation direction tends to favor the loading condition, and thus the highest deviation, ϕ_0^*, is reached at $\beta = 90°$. The gray area bounded by the line $\theta_0 = 0.5\beta$, encloses materials with the considerable deviation (i.e. $\phi_0 = |\theta_0 - \beta| \geq 50\%\beta$ at each set of loading). As shown in the top plot of Figure 3.4b, the considerable deviation with the direction β is first observed only in materials with low to moderate anisotropy ratios in which $\xi < 3$. Nevertheless, the rise in the stress anisotropy can gradually overshadow greater material anisotropy ratios, and thus several highly anisotropic cases are also incorporated in the gray area at $\lambda = 2$. Under such circumstances, the material with the least anisotropy ratio in the *Material*-dominance region (i.e. $\xi = 4$), indicates the highest deviation ϕ_0^* at the anisotropy orientation considerably close to $\beta = 90°$ (i.e. $\phi_0^* = \phi_0\ (\theta_0,\ \beta = 75°)$), meaning that small perturbations of β from 90° have significant impact on the initiation angle. Such significant variability in the initiation angle for small perturbations of the anisotropy orientations should be carefully considered in practical applications as it may give rise to potential problems.

Figure 3.4, the top row, revealed that unlike the isotropic case, the initiation direction in anisotropic rocks results from the interplay between the material anisotropy as well as the loading condition. Considering this interplay, the observations on the variations of the initiation pressure and length can be better understood. We now turn our attention to the *Material*-dominance region in which the θ_0-curve sustains the material tendency over increase in the stress anisotropy. As long as the deviation is not considerable, the function f given in Eq. 3.10, and consequently the apparent Irwin's number, remain roughly constant. In such cases, the rise in stress anisotropy assists initiation when θ_0 is nearly zero. For the nearly vertical initiation angle, however, the higher values of λ hinder initiation, and thus the initiation pressure rises in response to increase in λ. Figure 3.4 illustrates that once a considerable deviation appears in the *Material*-dominance region, a longer starter crack can be foreseen. Indeed, the greater the deviation, the higher the apparent Irwin's number. This means that more energy is dissipated at the instant of initiation, and clarifies why a longer crack is created for higher deviation values.

The increasing trend of δ_0 is reversed once the material undergoes the transition between *Material*-dominance and *Loading*-dominance, where the highest deviation provokes a surge in apparent Irwin's number. Thereafter, initiation length and pressure follow opposite trends with decrease in material anisotropy, meaning that the highest initiation pressure and length at a constant stress anistropy is reached at the so-called transitional material (e.g. the material anisotropy $\xi = 2$ at $\lambda = 1.5$). Indeed, low material anisotropy counteracts the effects of higher deviation, and thus the function f remains unchanged. On the other hand, due to the considerable deviation and penetration into the strong material direction, the initiation faces a higher resistance. In such cases, shorter cracks form and this explains why the increasing trend of δ stops as the transitional metrical is reached. Any further deviation in response to the increase in stress anisotropy drives initiation in a more tensile stress field region, and thus the initiation pressure decreases as the crack is more horizontally inclined. The decrease in initiation pressure in response to increasing stress anisotropy is also observed for isotropic formations with $\xi = 1$. In the isotropic case, however, the material is no longer direction-dependent, meaning that the initiation parameters versus the material anisotropy orientation β remain unchanged at each set of loading. Comparing the initiation pressure for different stress anisotropy reveals that a higher stress anisotropy promotes initiation by reducing the pressure required to break down an initially intact rock (see the top row of Figure 3.4). This conclusion can be reached simply by adopting the Hubbert-Willis approach, where the crack necessarily initiates along the intermediate stress σ_2.

The interaction between material anisotropy and stress anisotropy is crucial in the near-wellbore region, however, as the fracture propagates into the far-field, the impact of material anisotropy on fracture propagation diminishes [Sakha et al., 2022]. Numerical studies have demonstrated that oblique hydraulic fractures tend to reorient towards the plane perpendicular to the minimum in-situ stress [Dong and Tang, 2019; Sesetty and Ghassemi, 2018]. The degree of reorientation, or tortuosity, in the near-wellbore region serves as an indicator of this reorientation and increases as the initial crack becomes either shorter or more oblique relative to the plane perpendicular to the minimum in-situ stress [Dong and Tang, 2019]. Herein, the geometry of the initial crack is fully unknown, and both the length and initiation angle play a role in determining the tortuosity of propagation. As observed in Figure 3.4, in the *Material*-dominance region, the more *Material*-dominant the initiation is, the more oblique and shorter the crack forms at initiation, resulting in more tortuous crack propagation. This trend remains consistent up to the transitional material at each stress anisotropy (e.g. the material anisotropy $\xi = 3$ at $\lambda = 2$). However, as the material becomes more isotropic, the trend of increasing initial length is reversed, and shorter initial cracks are expected; while shorter cracks may increase tortuosity, in the *Loading*-dominance region, the initial crack forms almost perpendicular to the minimum in-situ stress, resulting in least tortuous hydraulic fracture propagation.

3.8.2 Size effect on the initiation parameters

Figure 3.5 shows the variations of the initiation pressure and length against the wellbore size for three different anisotropy orientations, when the formation is subjected to a constant stress anisotropy $\lambda = 1.5$. Regardless of the degree of anisotropy, the variations of the initiation parameters follow the same trend in response to the wellbore size. The material with the anistropy ratio $\xi = 2$, however, exhibits a slightly different trend especially when the anistoropy orientation is 75°. As illustrated in Figure 3.4b, the top plot, the material with the anisotropy ratio $\xi = 2$ can be considered as the transitional material for the wellbore size $R = 8$ cm. This means that the sensitivity of anisotropic materials in response to the size effect is similar to an isotropic formation provided that the anistropic formation does not undergo the transition between the *Material*- and *Loading*-dominance regions.

Figure 3.5 (the bottom plots) provides the results of the initiation length normalized by two following different lengthscales. I) the left-hand y-axis, represented by lines, identifies initiation length normalized by the wellbore radius R; II) the right-hand y-axis, indicated by the purple markers, measures the initiation length scaled by Irwin's material lengthscale defined along the principal direction 1 (i.e. $l_\mathrm{m} = K_{\mathrm{Ic},1}^2/\sigma_{\mathrm{T},1}^2$). Following the left-hand y-axis, Figure 3.5 clearly illustrates that the initiation length l_0 extends from 15 to 50 percent of the wellbore size for the different Irwin's numbers. Such large values exceed the much shorter initial length assumed as small percentage of the wellbore radius [Zhang et al., 2011; Sesetty and Ghassemi, 2018]. On the other hand, on the scale of the right-hand y-axis, the initiation length does not exceed 40% of the material lengthscale even when the wellbore size is unrealistically large (i.e. $R = 16$ cm which corresponds to $\mathcal{I} \approx 0.5$). This also contradicts the assumption that the starter crack extends as large as the material lengthscale.

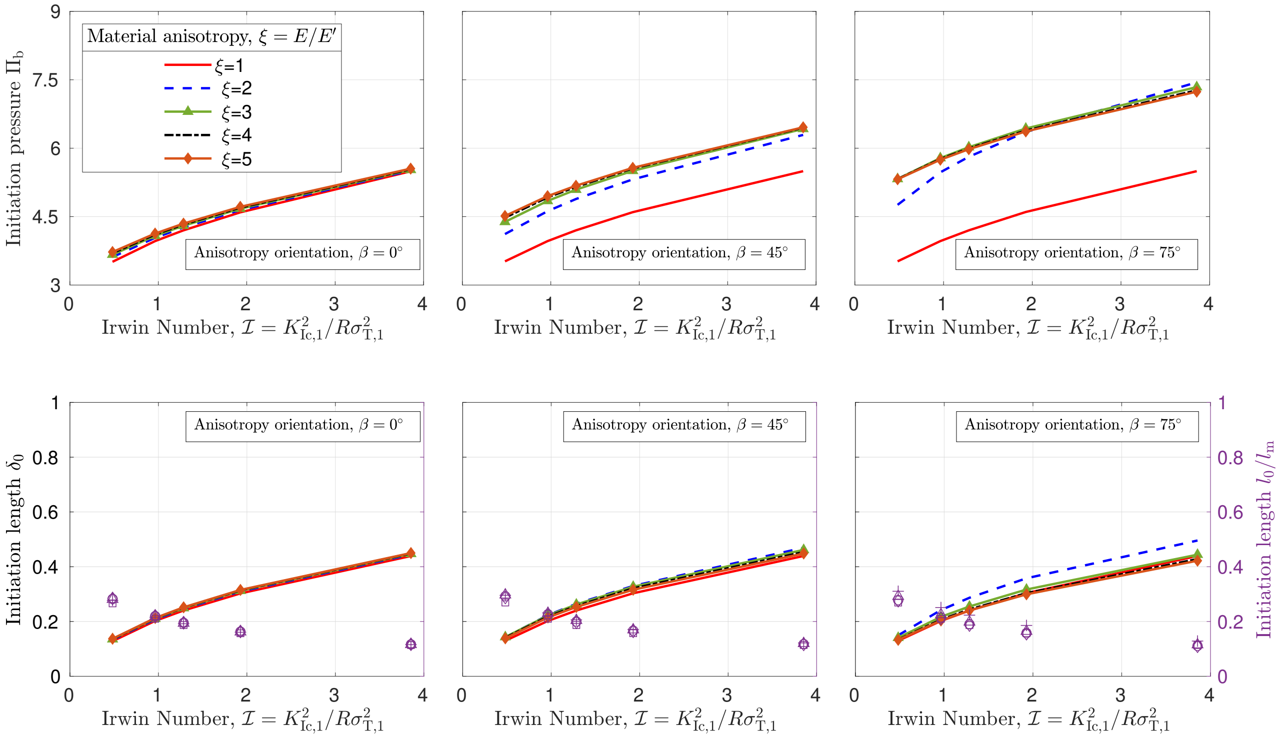

Figure 3.5: Variation of wellbore initiation parameters (pressure and length) with Irwin's number for different material anisotropy ratios under a constant stress anisotropy ($\lambda = 1.5$). Here, the results are provided for the following three different anisotropy orientations: $\beta = 0°, 45°, 75°$. Note that the legend denoting the color code used for each material anisotropy, applies to all subsequent plots.

Figure 3.5 also provides us with insights for developing strategies to reduce tortuosity in cases where the initial crack is highly oblique. As previously discussed, a highly oblique initial crack forms when the initiation mechanism is more material-dominant (i.e. $\xi \geq 3$ at $\lambda = 1.5$). As shown in Figure 3.5, in such cases, increasing the Irwin number (or decreasing the wellbore size) can result in a longer initial length δ_0 at the same initiation angle, leading to less tortuous crack propagation [Dong and Tang, 2019]. Therefore, the findings of this study support use of a smaller wellbore as an effective method to reduce tortuosity in hydraulic fracturing, particularly for relatively high material anisotropy in *Material*-dominance region.

3.8.3 Comparison of strength-based and mixed criteria

Irwin's number introduced by Lecampion [2012], characterizes two distinct failure mechanisms at the instant of initiation: while initiation is mostly strength-driven for vanishingly small FPZ, any increase in the fracture process size requires more energy to be dissipated to create new crack surfaces, and thus the failure mechanism is dominated by fracture energy for larger Irwin's numbers. Lecampion [2012] captured the size effect by plotting the initiation pressure with respect to Π_{strength} obtained by solely applying the strength-based criterion given by Eq. 3.1. His observations indicated that the initiation pressure $\Pi_{\text{b}}/\Pi_{\text{strength}}$ asymptotically approaches unity for $\mathcal{I} < 0.1$, whereas for $\mathcal{I} > 10$, the initiation pressure is mainly governed by the energy requirements and increases nearly linearly with Irwin's number. Figure 3.6 confirms Lecampion's observations in anisotropic case in the sense that a higher Irwin's number (or smaller wellbore size) evidently results in a higher deviation of the initiation pressure from the Π_{strength}, and thus favors energy-dominated failure. Nevertheless, in this case, the material anisotropy also plays a critical role in characterizing the failure mechanism which dominates tensile initiation.

Figure 3.6 reveals that higher anisotropy ratios ξ tend to make initiation more strength-dominated. On the other hand, as observed in Figure 3.4 for the same stress anisotropy $\lambda = 1.5$, the deviation in materials with anisotropy ratios greater than 3 is attributed to the *Material*-dominance region, where the material tendency is still decisive, and thus the strength-based equation predominates over the fracture energy included in Eq. 3.2. Therefore, the failure mechanism in materials with $\xi \geq 3$ favors strength-dominated initiation. Once the material tendency is overcome, the *Loading*-dominance region emerges, and thus the failure mechanism is mainly governed by the energy requirements. In this context, more energy is required for initiation when the apparent Irwin's number becomes large. This clarifies why the highest deviation of the initiation pressure from the Π_{strength}

is observed in the transitional material (i.e. $\xi = 2$ at $\lambda = 1.5$ at the maximum elongation).

We now turn our attention to the effect of the wellbore size on the sensitivity of the failure mechanism in response to any small changes in either the anisotropy orientation β or anisotropy ratio ξ. As illustrated in Figure 3.6, the variation of the initiation pressure $\Pi_\mathrm{b}/\Pi_\mathrm{strength}$ in the set $R = 8$ cm is more gradual than that wellbore with the half radius. Therefore, the failure mechanism described by $\Pi_\mathrm{b}/\Pi_\mathrm{strength}$ is more sensitive in response to any uncertainties in either β or ξ values when the wellbore size is smaller.

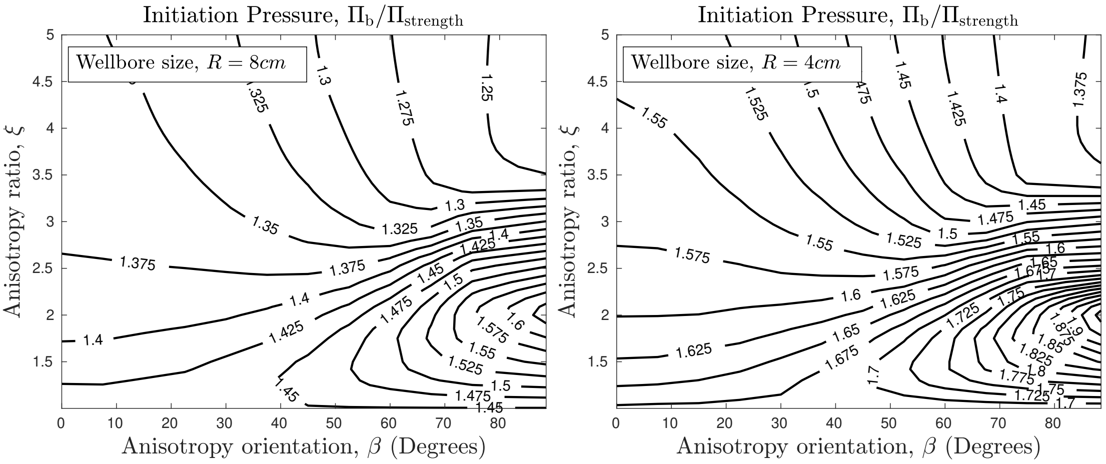

Figure 3.6: Variation of wellbore initiation pressure with the material anisotropy at different Irwin's number $\mathcal{I}$. Here, the stress anisotropy is kept constant at $\lambda = 1.5$.

3.9 Conclusions

The main findings of this article are as follows.

- The mixed criterion incorporates the fracture energy perspective to fully characterize hydraulic fracture initiation from an unnotched wellbore. Among the existing initiation criteria, the mixed criterion appears the most comprehensive as it also includes the effect of the wellbore size on the initiation parameters.
- The results predicted by the mixed criterion confirm the strong interplay between the stress and material anisotropy to determine the initiation angle in transversely isotropic rocks; while the material tends to derive the fracture toward the weak plane ($\theta_0 \to \beta$), the loading condition favors initiation perpendicular to the minimum in-situ stress ($\theta_0 \to 0$). Depending on the initiation angle, initiation may be described by either *Material*-dominance or *Loading*-dominance mechanisms.
- Depending on the loading anisotropy, the transition between *Material*-dominance and *Loading*-dominance arises at a specific material anisotropy ratio which yields the highest initiation pressure and length among other anisotropic materials.
- According to the mixed criterion predictions, neither LEFM nor assuming a fixed $\delta_0 := l_0/R$ can accurately address hydraulic fracture initiation. The initiation length strongly depends on the wellbore size.
- Excluding the fracture energy condition from the mixed criterion may lead to underestimation in the initiation pressure predictions especially when the wellbores are small. This can highlight the importance of the mixed criterion in the presence of the small wellbores.

Chapter 4

Phase-field model with orthotropy-based energy decomposition

M. Sakha[a], L. De Lorenzis[b], T. Driesner[a]

[a] *Department of Earth Sciences, ETH Zurich, Switzerland*
[b] *Department of Mechanical and Process Engineering, ETH Zurich, Switzerland*

2023, Prepared for submission to the journal of *Computer Methods in Applied Mechanics and Engineering.*

4.1 Abstract

This study employs the phase-field model with the generalized spectral decomposition proposed in the literature for orthotropic materials to predict the fracture trajectories in transversely isotropic rocks under fixed mixed-mode loading ratios. While the model has been primarily used for modelling an orthotropic plate under simple tensile and shearing loading conditions, we extend its utility to assess its accuracy through comparison with experimental data, where the notched semi-circular specimens of Grimsel Granite undergo complex mixed-mode loading. Among the experimental data available in previous studies, we focused on two mode-mixity ratios, which are small enough to avoid the need for a more complex decomposition, but they may lead to interpenetration if a model allowing physically impossible fracturing under compression is applied. Therefore, the adoption of a generalized decomposition phase-field model is crucial. Despite the material exhibiting transverse isotropy in terms of both elasticity and fracture toughness, it is shown that the

model is able to capture the fracture trajectory quite accurately even when assuming a direction-independent fracture toughness.

4.2 Introduction

The future of geo-engineered structures and hydraulic fracturing within geological applications is closely tied to our knowledge of fracturing in the rock formations [Shen and Shi, 2016; Chertov, 2012; Fink et al., 2022]. While experimental studies have demonstrated the presence of complexity both in material properties and loading conditions within underground laboratories [Gischig et al., 2018; Shen and Shi, 2016], there remains an imperative for the development of a cost-efficient, sophisticated numerical model able to capture different fracturing mechanisms in rock formations.

To better describe the mechanism of fracturing is solids, numerical simulations play an indispensable role. Many studies have so far employed various numerical techniques such as discrete element method (DEM) [Fakhimi et al., 2002; Tan et al., 2009; Chong et al., 2017], boundary element method (BEM) [Chen et al., 1998; Ke et al., 2009; Lecampion, 2012; Shen and Shi, 2016; Sakha et al., 2023] and finite element method (FEM/XFEM) [Ingraffea and Heuze, 1980; Zi and Belytschko, 2003; Richardson et al., 2009; Nejati et al., 2015a,b; Shi et al., 2017; Mehraban et al., 2023] to model fracturing process. Depending on the characteristics of the problem and advantages/disadvantages associated with each technique, one or two of these methods are more favorable. Most of these techniques, however, fail to capture fracturing in cases where more complex mechanisms such as bifurcation, merging, kinking are expected [Lorenzis and Düster, 2020]. In such cases, phase-field modelling is strongly recommended in the literature [Wu et al., 2020a]. This technique, unlike other methods, has no need to any crack tracking algorithm or any additional criteria to describe complex fracturing process [Ziaei-rad et al., 2023]. It simply seeks a trajectory of the smeared crack on a continuum with a pre-defined mesh, which minimizes the energy functional [Wu et al., 2020a]. That's why the technique is currently garnering significant attention in the field of subsurface fracturing, where a complex loading regime along with material complexity can potentially yield intricate fracturing.

The main concept of the phase-field model can be attributed to the seminal development of Bourdin et al. [2008] who regularized the original energy functional of quasi-static brittle fracture [Francfort and Marigo, 1998]. The method perceives the sharp crack discontinuity as a phase variable smoothly smeared across the fully damaged and undamaged phases. The phase-field, representing the crack path, ultimately crawls along the direction where the potential energy of the whole system reaches a minimum [Wu et al., 2020a]. In this regard, the formulation should distinguish between tension and compression in fracturing, meaning that the contribution of the tensile loading has to be only considered in minimization of the potential energy [Lorenzis and Düster, 2020]. Depending on the physics of the problem, the tension-compression asymmetry has been interpreted in different ways in isotropic solids. In anisotropic material, however, these various interpretations of the persistent compression and crack-driving tension need to be extended in such a manner that preservers the orthogonality condition between the transformed stress and strain spaces [Ziaei-rad et al., 2023].

This paper adopts the generalized spectral decomposition of the phase-field proposed by Dijk et al. [2020] for orthotropic materials, to model fracturing in transversely isotropic solids. For the validation purpose, we first reproduce the results observed by Ziaei-rad et al. [2023] for the fracture propagation of an initial edge notch in a rectangular plate under simple tensile and shear loading conditions. Once implementation of the formulation is verified, we assess the robustness of the decomposition through comparison with experimental data given by Sakha et al. [2022] on fracture trajectory and the effective fracture toughness where the semi-circular specimens of Grimsel Granite are under fixed mixed-mode loading ratios. As it is discussed in Sakha et al. [2022], there is a strong interplay between the loading and material anisotropy in determining the angle at which the crack propagates. Additionally, Sakha et al. [2022] employed a direction-dependent fit for the fracture toughness, assuming a sinusoidal variation between the two principal directions of the material. In contrast, the material in this study is assumed to have a direction-independent resistance against fracturing, resulting in a constant fracture toughness value for the entire domain surrounding the crack tip. By exclusively assuming anisotropy in material elasticity, the actual effect of material anisotropy can be overshadowed. This means that in this study, the effect of loading is somehow amplified in comparison with the physical reality of the problem. Nevertheless, the robustness of the decomposition enables us to capture the fracture behavior quite accurately, particularly in cases where the mixed-mode ratios are not significantly high.

4.3 Model Formulation: Phase-field

Assuming the domain $\Omega \subset \mathbb{R}^d$, represents a d-dimensional linear elastic body, the regularized form of the energy functional of quasi-static brittle fracture reads as [Francfort and Marigo, 1998; Bourdin et al., 2008; Lorenzis and Düster, 2020]:

$$E[\mathbf{u}, \alpha] = \int_{\Omega} g(\alpha)\Psi(\boldsymbol{\epsilon}(\mathbf{u}))\, d\Omega + \frac{\mathcal{G}_{\mathrm{c}}}{c_w} \int_{\Omega} \left(\frac{w(\alpha)}{\ell} + \ell \left|\nabla\alpha\right|^2 \right) d\Omega - \int_{\Gamma_{\mathrm{N}}} \bar{\mathbf{t}}_{\mathbf{n}}.\mathbf{u}\, ds. \qquad (4.1)$$

Here, the traction $\bar{\mathbf{t}}_{\mathbf{n}}$ is prescribed on the Neumann boundary Γ_{N}. Under quasi-static loading, the energy functional is minimized incrementally to track the evolution of the scalar α and the displacement vector at each loading steps. In this regard, the kinematically admissible displacement field $\mathbf{u} : \Omega \to \mathbb{R}^d$ must satisfy the homogeneous/non-homogeneous Dirichlet conditions prescribed on the boundary Γ_{D}. The phase-field $\alpha : \Omega \to [0, 1]$ represents the smeared counterpart of the discontinuity across the crack Γ_{c}, taking $\alpha = 0$ and $\alpha = 1$ for the undamaged and the fully broken material phases, respectively.

In Eq. 4.1, the term $\Psi(\boldsymbol{\epsilon}(\mathbf{u}))$ denotes the strain energy density function stored in the elastic body, which can be dissipated by the phase-field evolution provided that it can overcome the fracture toughness of the material, $\mathcal{G}_{\mathrm{c}}$. The fracturing process, however, is controlled by the interplay between the elastic energy degradation function $g(\alpha)$, the function $w(\alpha)$.

In the literature, there exists a vast range of choices for the functions $g(\alpha)$ and $w(\alpha)$, each supported by various arguments and discussions [Pham et al., 2011; Kuhn et al., 2015]. Among these choices, the quadratic degradation function (i.e. $g(\alpha) = (1-\alpha)^2$) and the linear function $w(\alpha)$ (i.e. $w(\alpha) = \alpha$, known as AT-1[1]) hold greater physical meaning and are consequently more widely accepted. While the AT-1 model retains the elastic stage in the absence of crack, the quadratic degradation function encapsulates the essential features required for describing the evolution of the phase-field and its impacts

---

[1] AT is named after Ambrosio-Tortorelli [Ambrosio and Tortorelli, 1990]

on the material stiffness [Kuhn et al., 2015]. By adopting these two functions, one can achieve a comprehensive and physically meaningful model capable of capturing a wide range of fracturing phenomena. In this framework, the normalization constant c_w defined as $c_w := 4\int_0^1 \sqrt{w(t)}\,dt$ takes the value of $\frac{8}{3}$.

In Eq. 4.1, the strain energy density $\Psi(\boldsymbol{\epsilon}(\mathbf{u}))$ is symmetric with respect to the compressive and tensile principal strains (i.e. $\langle\epsilon\rangle_-$ and $\langle\epsilon\rangle_+$ [2]), lacking the ability to distinguish between compression and tension. This means that a phase-field can evolve even if the fracture surfaces are under compression, leading to interpenetration and unphysical crack propagation. To address this issue, it is essential to decompose the contributions of tension and compression within the strain energy density, where the tensile and compressive strain energy densities are respectively defined as $\Psi^+(\boldsymbol{\epsilon}(\mathbf{u}))$ and $\Psi^-(\boldsymbol{\epsilon}(\mathbf{u}))$. By doing so, the contribution of the function $\Psi^+(\boldsymbol{\epsilon}(\mathbf{u}))$ can be solely degraded, ensuring realistic fracture evolution against interpenetration of fracture surface. Figure 4.1 shows the evolution of the phase-field when an isotropic square plate with an edge initial crack undergoing shearing along the x direction. As shown in this figure, without applying any decomposition to the phase-field model (or equivalently using a symmetric compression-tension phase-field model), the crack fails to differentiate between the compressive and tensile regions, resulting in a symmetrically bifurcated crack propagation. The propagation along the compressive region is, however, effectively suppressed provided that a simple decomposition model such as the volumetric-deviatoric decomposition (is independently laid out by Amor et al. [2009] and Freddi and Royer-Carfagni [2009]) is employed. Note that while the term anisotropic model is usually used in the literature to address such decomposition [Wu et al., 2020b; Ziaei-rad et al., 2023], this article reserves the term "anisotropy" to specifically refer to the directional dependency of the material's mechanical properties.

---

[2] The angle brackets $\langle\rangle$ represents Macaulay or singularity functions. Therefore,

$$\langle x\rangle_+ = \begin{cases} x & \text{if} \quad x \geq 0 \\ 0 & \text{if} \quad x < 0 \end{cases} \quad \langle x\rangle_- = \begin{cases} 0 & \text{if} \quad x > 0 \\ x & \text{if} \quad x \leq 0 \end{cases} \tag{4.2}$$

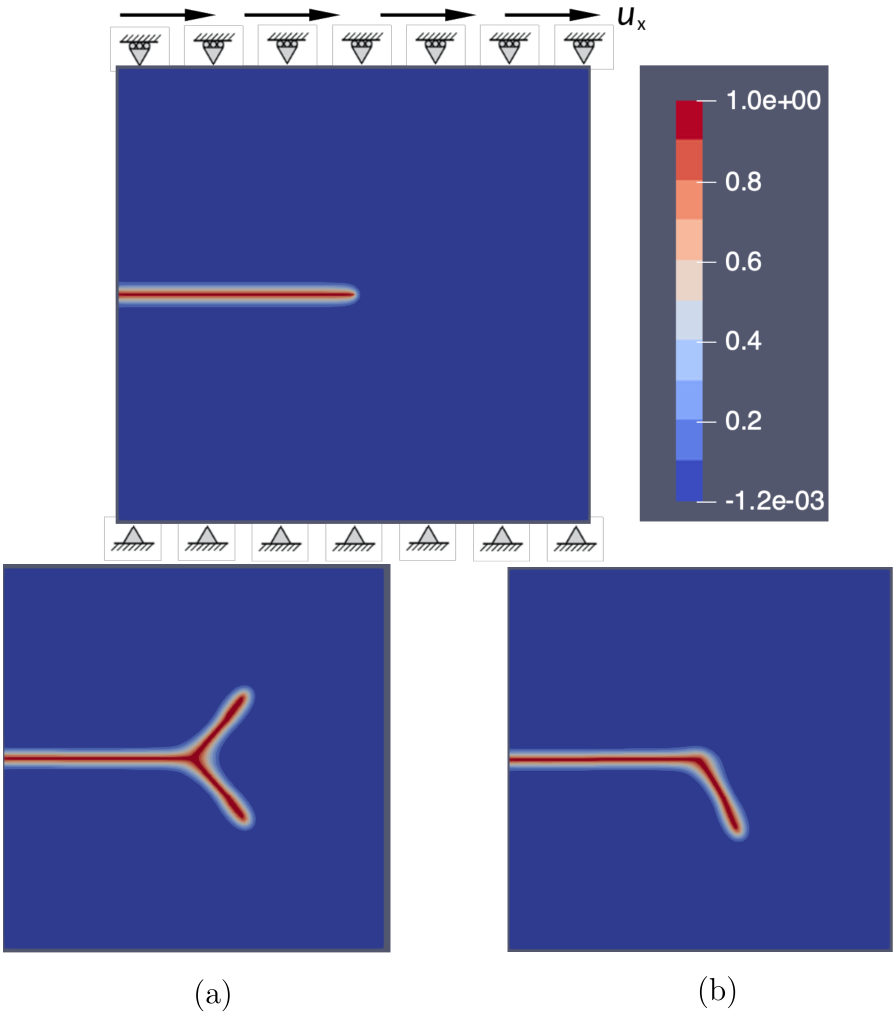

(a) (b)

Figure 4.1: Phase-field evolution of an initial edge crack within an isotropic square plate subjected to shearing. (a) Symmetric bifurcated crack propagation using a symmetric compression-tension phase-field model. (b) Singular crack kinking in the tensile region using an asymmetric compression-tension phase-field modeling.

Minimization of the energy functional is a constrained problem that requires addressing the irreversibility condition $\dot{\alpha} \geq 0$. To enforce compliance with this condition, we incorporate the history field, which guarantees irreversibility by taking the maximum accumulated value of Ψ^+ in the loading history as the driving force. Therefore, the loading history can be defined as [De Lorenzis and Gerasimov, 2020]:

$$\mathcal{H}_n(\mathbf{x}) := \max\{\mathcal{H}_{n-1}(\mathbf{x}), \Psi^+(\boldsymbol{\epsilon}(\mathbf{u}))\} \quad \mathcal{H}_0(\mathbf{x}) = 0. \tag{4.3}$$

To solve a phase-field minimization problem, we opt for the staggered approach over the monolithic solvers. As explained by De Lorenzis and Gerasimov [2020], in this approach, we alternate between minimizing the energy functional while freezing the damage and subsequently freezing the displacement, all in a sequential manner, until the convergence is attained. While monolithic solvers are typically more efficient [Agrawal and Runnels, 2021], we have found that the staggered method is sufficiently robust and straightforward to be implemented in phase-field modeling of anisotropic solids.

4.3.1 Miehe decomposition for isotropic materials

Spectral decomposition (also known as the Miehe technique) is a commonly used method for separating the tensile and compressive components of the strain energy density. This technique assigns $\Psi^+(\boldsymbol{\epsilon}(\mathbf{u}))$ to the tensile principal strains while preserving the compressive principal strains for $\Psi^-(\boldsymbol{\epsilon}(\mathbf{u}))$. Assuming λ and μ represent the Lamé constants, the strain energy density for the isotropic materials can be defined as [De Lorenzis and Gerasimov, 2020; Dijk et al., 2020]:

$$\Psi = \frac{1}{2}\left(\lambda \operatorname{Tr}(\boldsymbol{\epsilon})^2 + 2\mu \operatorname{Tr}\left(\boldsymbol{\epsilon}^2\right)\right). \tag{4.4}$$

It can be easily shown that the terms $\operatorname{Tr}\boldsymbol{\epsilon}$ and $\operatorname{Tr}\boldsymbol{\epsilon}^{\mathbf{2}}$ are invariants of the strain tensor, meaning that they remain unchanged regardless of the coordinate system used to represent the strain tensor. In this regard, while we represent the term $\operatorname{Tr}\boldsymbol{\epsilon}$ in the original coordinate system xyz, the compact form of the term $\operatorname{Tr}\boldsymbol{\epsilon}^{\mathbf{2}}$ is achieved when expressed in the principal coordinate system (see Figure 4.2a). Therefore, we have:

$$\Psi = \frac{1}{2}\left(\lambda\left(\epsilon_{\mathrm{xx}} + \epsilon_{\mathrm{yy}} + \epsilon_{\mathrm{zz}}\right)^2 + 2\mu\left(\epsilon_1^2 + \epsilon_2^2 + \epsilon_3^2\right)\right). \tag{4.5}$$

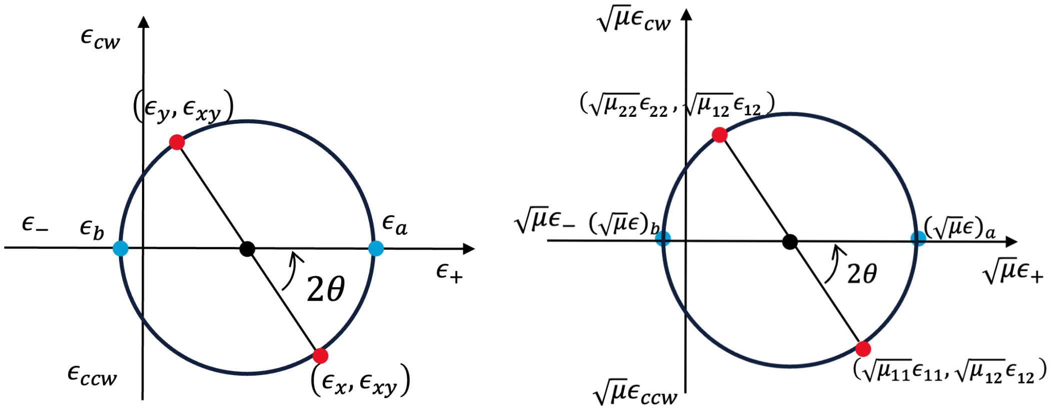

(a) (b)

Figure 4.2: (a) The Mohr circle of $\boldsymbol{\epsilon}$ showing the eigenvalues/vectors of the strain tensor. (b) the Mohr circle of $(\sqrt{\boldsymbol{\mu}}\boldsymbol{\epsilon})$ showing the eigenvalues/vectors of the tensor $\boldsymbol{\Psi}_\mu$.

Eq. 4.5 can now be decomposed into the tensile and compressive components of the strain energy density as [Dijk et al., 2020]:

$$\Psi_\pm = \frac{1}{2}\left(\lambda\langle\epsilon_{\text{xx}} + \epsilon_{\text{yy}} + \epsilon_{\text{zz}}\rangle_\pm{}^2 + 2\mu\langle\epsilon_1\rangle_\pm^2 + 2\mu\langle\epsilon_2\rangle_\pm^2 + 2\mu\langle\epsilon_3\rangle_\pm^2\right). \tag{4.6}$$

Within the finite element (FE) framework, the definition of the Cauchy stress tensor $\boldsymbol{\sigma}$ and the tangent stiffness tensor $\boldsymbol{C}$ is essential. These tensors are employed in the FE quantities $f^u_{\text{int},e}$ and K^u_e, respectively representing the internal forces and stiffness of the system at each element. Assuming the definition of the strain energy density function is known, one can define the tensors $\boldsymbol{\sigma}$ and $\boldsymbol{C}$ as:

$$\boldsymbol{\sigma}_\pm = \frac{d\Psi_\pm}{d\boldsymbol{\epsilon}}, \quad \boldsymbol{C}_\pm = \frac{d^2\Psi_\pm}{d\boldsymbol{\epsilon}^2}. \tag{4.7}$$

Following Miehe's decomposition model in Eq. 4.6, the tensors $\boldsymbol{\sigma}$ and $\boldsymbol{C}$ for the isotropic materials can be expressed as [Ambati, 2017]:

$$\begin{aligned} \boldsymbol{\sigma}_\pm &= \lambda\langle\text{Tr}(\boldsymbol{\epsilon})\rangle_\pm \boldsymbol{I} + 2\mu\langle\boldsymbol{\epsilon}\rangle_\pm, \\ \boldsymbol{C}_\pm &= \lambda\mathcal{H}_{\text{Tr}(\langle\boldsymbol{\epsilon}\rangle_\pm)}\boldsymbol{I}\otimes\boldsymbol{I} + 2\mu\mathbb{P}_\pm, \quad \mathcal{H}_{\text{Tr}(\boldsymbol{\epsilon})_\pm} = \frac{\langle\text{Tr}(\boldsymbol{\epsilon})\rangle_\pm}{\text{Tr}(\boldsymbol{\epsilon})} \end{aligned} \tag{4.8}$$

By comparing Eq. 4.6 with Eq. 4.8, one can observe that that the projection tensor $\mathbb{P}_{\pm}$ is derived as the result of [Ambati, 2017]

$$\mathbb{P}_{\pm} = \frac{1}{2}\sum_{a=1}^{3} \frac{\partial^2 \langle \epsilon^a \rangle_{\pm}^2}{\partial \epsilon_{ij} \partial \epsilon_{kl}} = \sum_{a=1}^{3} \frac{\partial}{\partial \epsilon_{ij}} (\langle \epsilon^a \rangle_{\pm} \frac{\partial \langle \epsilon^a \rangle_{\pm}}{\partial \epsilon_{kl}}) = \sum_{a=1}^{3} \frac{\partial \langle \epsilon^a \rangle_{\pm}}{\partial \epsilon_{ij}} \frac{\partial \langle \epsilon^a \rangle_{\pm}}{\partial \epsilon_{kl}} + \langle \epsilon^a \rangle_{\pm} \frac{\partial^2 \langle \epsilon^a \rangle_{\pm}}{\partial \epsilon_{ij} \partial \epsilon_{kl}}. \quad (4.9)$$

The tensor $\mathbb{P}_{\pm}$ is therefore defined as [Ambati, 2017]:

$$\mathbb{P}_{\pm} = \sum_{a=1}^{3} \mathcal{H}_{\epsilon^a_{\pm}} \mathbb{H}^a + \sum_{a=1}^{3} \sum_{b \neq a}^{3} \frac{\langle \epsilon^a \rangle_{\pm}}{2(\epsilon^a - \epsilon^b)} (\mathbb{G}^{ab} + \mathbb{G}^{ba}), \quad \mathcal{H}_{\epsilon^a_{\pm}} = \frac{\langle \epsilon^a \rangle_{\pm}}{\epsilon^a} \quad (4.10)$$

with

$$\begin{aligned} \mathbb{H}^a_{ijkl} &= M^a_{ij} M^a_{kl} = n^a_i n^a_j n^a_k n^a_l \\ \mathbb{G}^a_{ijkl} &= M^a_{ik} M^a_{jl} + M^a_{il} M^a_{jk} \end{aligned} \quad (4.11)$$

Note that in derivation of the tensors $\boldsymbol{\sigma}$ and $\boldsymbol{C}$, the orthogonality condition must hold in such a way that $\boldsymbol{C}_{\pm}\boldsymbol{\epsilon}.\boldsymbol{\epsilon}_{\mp} = 0$ [Dijk et al., 2020]. By considering the relation $\boldsymbol{\sigma}_{\pm} = \boldsymbol{C}_{\pm}\boldsymbol{\epsilon} = \boldsymbol{C}\boldsymbol{\epsilon}_{\pm}$, it becomes evident that in isotropic materials, the $\boldsymbol{\sigma}_{\pm}$ terms correspond to the principal stresses that align with the principal strains. This observation is particularly applicable to isotropic materials, where the material properties are symmetric in all directions. In orthotropic materials, however, one needs to enforce the orthogonality condition in a transformed strain-stress space, meaning that in such materials the tensile and compressive portions of the strain energy density must be modified [Ziaei-rad et al., 2023].

4.3.2 Generalized Miehe decomposition for orthotropic materials

Assuming the coordinate system x′y′ is oriented along the material principal axes of an orthotropic material, the stiffness matrix following the Voigt notation is expressed as:

$$\boldsymbol{C} = \begin{pmatrix} \alpha_{11} & \lambda_{12} & \lambda_{31} & 0 & 0 & 0 \\ \lambda_{12} & \alpha_{22} & \lambda_{23} & 0 & 0 & 0 \\ \lambda_{31} & \lambda_{23} & \alpha_{33} & 0 & 0 & 0 \\ 0 & 0 & 0 & \mu_{12} & 0 & 0 \\ 0 & 0 & 0 & 0 & \mu_{23} & 0 \\ 0 & 0 & 0 & 0 & 0 & \mu_{31} \end{pmatrix}, \tag{4.12}$$

where μ_{ij} are the shear moduli, and α_{ii} denote the constrained moduli (also known as p-wave moduli). Here, using the components of the stiffness matrix, we introduce the tensors $\boldsymbol{\Psi}_\lambda$ and $\boldsymbol{\Psi}_\mu$ as [Dijk et al., 2020]:

$$\boldsymbol{\Psi}_\lambda = \begin{pmatrix} \sqrt{\lambda_{11}}\epsilon_{11} & \sqrt{\lambda_{12}}\epsilon_{12} & \sqrt{\lambda_{31}}\epsilon_{31} \\ \sqrt{\lambda_{12}}\epsilon_{12} & \sqrt{\lambda_{22}}\epsilon_{22} & \sqrt{\lambda_{23}}\epsilon_{23} \\ \sqrt{\lambda_{31}}\epsilon_{31} & \sqrt{\lambda_{23}}\epsilon_{23} & \sqrt{\lambda_{33}}\epsilon_{33} \end{pmatrix}, \quad \boldsymbol{\Psi}_\mu = \begin{pmatrix} \sqrt{\mu_{11}}\epsilon_{11} & \sqrt{\mu_{12}}\epsilon_{12} & \sqrt{\mu_{31}}\epsilon_{31} \\ \sqrt{\mu_{12}}\epsilon_{12} & \sqrt{\mu_{22}}\epsilon_{22} & \sqrt{\mu_{23}}\epsilon_{23} \\ \sqrt{\mu_{31}}\epsilon_{31} & \sqrt{\mu_{23}}\epsilon_{23} & \sqrt{\mu_{33}}\epsilon_{33} \end{pmatrix}. \tag{4.13}$$

where considering no summation over the repeated indices, the components λ_{ii} and μ_{ii} are defined as

$$\begin{aligned} \lambda_{\mathrm{ii}} &= \frac{\lambda_{\mathrm{ij}}\lambda_{\mathrm{ki}}}{\lambda_{\mathrm{jk}}}, \\ \mu_{\mathrm{ii}} &= \frac{1}{2}(\alpha_{\mathrm{ii}} - \lambda_{\mathrm{ii}}). \end{aligned} \tag{4.14}$$

Given the definition of the tensors $\boldsymbol{\Psi}_\lambda$ and $\boldsymbol{\Psi}_\mu$, the applicability of the Miehe decomposition can be extended to the orthotropic materials using the following relation for the strain energy density function Dijk et al. [2020]:

$$\Psi_\pm = \frac{1}{2}\langle \psi_{\lambda,11} + \psi_{\lambda,22} + \psi_{\lambda,33}\rangle_\pm{}^2 + \langle \psi_{\mu,1}\rangle_\pm^2 + \langle \psi_{\mu,2}\rangle_\pm^2 + \langle \psi_{\mu,3}\rangle_\pm^2. \tag{4.15}$$

This relation preserves the orthogonality condition for $\boldsymbol{C}_\pm^{\frac{1}{2}}\boldsymbol{\epsilon}.\boldsymbol{C}_\mp^{\frac{1}{2}}\boldsymbol{\epsilon} = 0$. Unlike Eq. 4.6, where the contribution of shearing was determined solely based on the eigenvalues of the strain field, the current formulation incorporates the contribution of shearing based on the eigenvalues of the tensor $\boldsymbol{\Psi}_\mu$. By considering the Mohr circle of $(\sqrt{\boldsymbol{\mu}}\boldsymbol{\epsilon})$ as an analogy to the Mohr circle of $\boldsymbol{\epsilon}$, one can derive the Cauchy stress tensor $\boldsymbol{\sigma}$ and the tangent stiffness tensor $\boldsymbol{C}$ using a similar approach as described in Eq. 4.8, provided that the strain components ϵ_{ij} is expressed in the material coordinate system (see Figure 4.2b). We therefore have

$$
\begin{aligned}
\boldsymbol{\sigma}_\pm &= \langle \mathrm{Tr}(\boldsymbol{\Psi}_\lambda) \rangle_\pm \bar{\boldsymbol{I}} + 2\langle \boldsymbol{\mu}\boldsymbol{\epsilon} \rangle_\pm \bar{\boldsymbol{M}}^\pm, \\
\boldsymbol{C}_\pm &= \bar{\boldsymbol{I}} \otimes \bar{\boldsymbol{I}} + 2\bar{\mathbb{P}}_\pm, \quad \mathcal{H}_{\mathrm{Tr}(\boldsymbol{\epsilon})_\pm} = \frac{\langle \mathrm{Tr}(\boldsymbol{\epsilon}) \rangle_\pm}{\mathrm{Tr}(\boldsymbol{\epsilon})}
\end{aligned}
\tag{4.16}
$$

where the tensors $\bar{\boldsymbol{I}}$ and $\bar{\boldsymbol{M}}^\pm$ are given by:

$$
\begin{aligned}
\bar{\boldsymbol{I}}_{ij} &= \sqrt{\lambda_{kl}}\delta_{kl}\delta_{ij} \\
\bar{M}^\pm_{ij} &= \sqrt{\mu_{kl}}\delta_{ki} n^\pm_i \delta_{lj} n^\pm_j
\end{aligned}
\tag{4.17}
$$

and the orthotropic projection tensor $\bar{\mathbb{P}}_\pm$ is derived as:

$$
\begin{aligned}
\bar{\mathbb{P}}_\pm = \frac{1}{2}\sum_{a=1}^{3} \frac{\partial^2 \langle (\mu\epsilon)^a \rangle^2_\pm}{\partial\epsilon_{ij}\partial\epsilon_{kl}} = \sum_{a=1}^{3} \frac{\partial}{\partial\epsilon_{ij}} (\langle (\mu\epsilon)^a \rangle_\pm \frac{\partial \langle (\mu\epsilon)^a \rangle_\pm}{\partial\epsilon_{kl}}) = \sum_{a=1}^{3} \Bigg(\frac{\partial \langle (\mu\epsilon)^a \rangle_\pm}{\partial\epsilon_{ij}} \frac{\partial \langle (\mu\epsilon)^a \rangle_\pm}{\partial\epsilon_{kl}} \\
+ \langle (\mu\epsilon)^a \rangle_\pm \frac{\partial^2 \langle (\mu\epsilon)^a \rangle_\pm}{\partial\epsilon_{ij}\partial\epsilon_{kl}} \Bigg).
\end{aligned}
\tag{4.18}
$$

Considering, the tensor $\bar{\mathbb{P}}_\pm$ is defined as,

$$
\bar{\mathbb{P}}_\pm = \sum_{a=1}^{3} \mathcal{H}_{(\mu\epsilon)^{\mathrm{a}}_\pm} \bar{\mathbb{H}}^a + \sum_{a=1}^{3}\sum_{b\neq a}^{3} \frac{\langle (\mu\epsilon)^a \rangle_\pm}{2((\mu\epsilon)^a - (\mu\epsilon)^b)} (\bar{\mathbb{G}}^{ab} + \bar{\mathbb{G}}^{ba}), \quad \mathcal{H}_{(\mu\epsilon)^{\mathrm{a}}_\pm} = \frac{\langle (\mu\epsilon)^a \rangle_\pm}{(\mu\epsilon)^a}
\tag{4.19}
$$

with

$$\begin{aligned}\bar{\mathbb{H}}^a_{ijkl} &= \bar{M}^a_{ij}\bar{M}^a_{kl}\\ \bar{\mathbb{G}}^a_{ijkl} &= \bar{M}^a_{ik}\bar{M}^a_{jl} + \bar{M}^a_{il}\bar{M}^a_{jk}\\ \bar{M}^a_{ij} &= \sqrt{\mu_{kl}}\delta_{ki}n^a_i\delta_{lj}n^a_j\end{aligned} \tag{4.20}$$

To obtain the tensors $\boldsymbol{\sigma}$ and $\boldsymbol{C}$ in the original coordinate system, transformation rules need to be applied considering the Voigt notation. Assuming the material coordinate system x′y′ results from rotating the original coordinate xy along the axis z by β, the tensors $\boldsymbol{\sigma}$ and $\boldsymbol{C}$ in the original coordinate system are as follows [Ting, 1996]:

$$\begin{aligned}&\boldsymbol{\sigma}_{\text{original}} = \boldsymbol{K}_\sigma^{-1}\boldsymbol{\sigma}\\ &\boldsymbol{C}_{\text{original}} = \boldsymbol{K}_\sigma^{-1}\boldsymbol{C}\boldsymbol{K}_\epsilon\\ &\boldsymbol{K}_\sigma = \begin{pmatrix} c^2 & s^2 & 0 & 2cs & 0 & 0\\ s^2 & c^2 & 0 & -2cs & 0 & 0\\ 0 & 0 & 1 & 0 & 0 & 0\\ -cs & cs & 0 & c^2-s^2 & 0 & 0\\ 0 & 0 & 0 & 0 & c & -s\\ 0 & 0 & 0 & 0 & s & c \end{pmatrix}, \quad \boldsymbol{K}_\epsilon = \begin{pmatrix} c^2 & s^2 & 0 & cs & 0 & 0\\ s^2 & c^2 & 0 & -cs & 0 & 0\\ 0 & 0 & 1 & 0 & 0 & 0\\ -2cs & 2cs & 0 & c^2-s^2 & 0 & 0\\ 0 & 0 & 0 & 0 & c & -s\\ 0 & 0 & 0 & 0 & s & c \end{pmatrix},\end{aligned} \tag{4.21}$$

4.4 Results and discussions

The validity of the generalized Miehe decomposition and its implementation are assessed in Section 4.4.1 through comparison of the fracture path, and the load-displacement relationships. The results simulated in the present study are compared with those reported by Ziaei-rad et al. [2023] for the cracked square plate under tensile and shear loading. Once the reliability of the model implementation is confirmed, Section 4.4.2 further investigates the model's robustness by comparing experimental data with phase-field model predictions for fracture trajectory and the effective fracture toughness of semi-circular samples of Grimsel Granite under a fixed mode-mixity ratio. Sakha et al. [2022] showed that the stress distribution of the compressive loading ahead of the crack tip in these samples can counterbalance the tensile driving forces, provided that the compressive regions are considered within the interval of validity. That's why the authors are motivated to investigate the robustness of the decomposition model by applying it to predict of the kink cracks in the modified SCB tests.

4.4.1 Validation with numerical studies

To apply the generalized Miehe decomposition to the phase-field model, a square plate with dimensions of $L \times L \times H$ is considered under tensile and shear loading conditions (see Figure 4.3). In this case, the plate has a length $L = 1$ mm with a thickness $H = 1$ mm, and contains an initial horizontal notch extending from $[0, L/2]$ to $[L/2, L/2]$, which is modeled as a sharp notch. This implies that the elements on the two opposite sides of the notch do not share nodes, and the nodes are duplicated for both sides of the notch. While the plane-strain condition is assumed in these cases, it is necessary to know the thickness of the material in order to measure the forces along the directions at which the nodes are constrained. Considering the lowest mesh size of $h = 4.7 \times 10^{-4}$ mm for the region close to the fracture trajectory, the specimen is discretized by 45K and 94K linear quadrilateral elements for the tensile and shear tests, respectively.

Table 4.1 provides the mechanical properties of the cracked plate for an orthotropic material, as given by Ziaei-rad et al. [2023]. In this analysis, it is assumed that the resistance of the material against fracturing is direction-independent, resulting in a constant fracture toughness value for each orientation. The bottom side of the plate is fixed, while the top side is displaced in the y-direction for the tensile case and in the x-direction for the shear case. In each case, contrary to the boundary conditions assumed by Hirshikesh et al. [2021], we followed the assumptions proposed by Ziaei-rad et al. [2023]; Dijk et al. [2020], wherein the top side of the plate is constrained along the transverse direction of the applied displacement. This condition is crucial for the situations where the crack is likely to kink from the initial path.

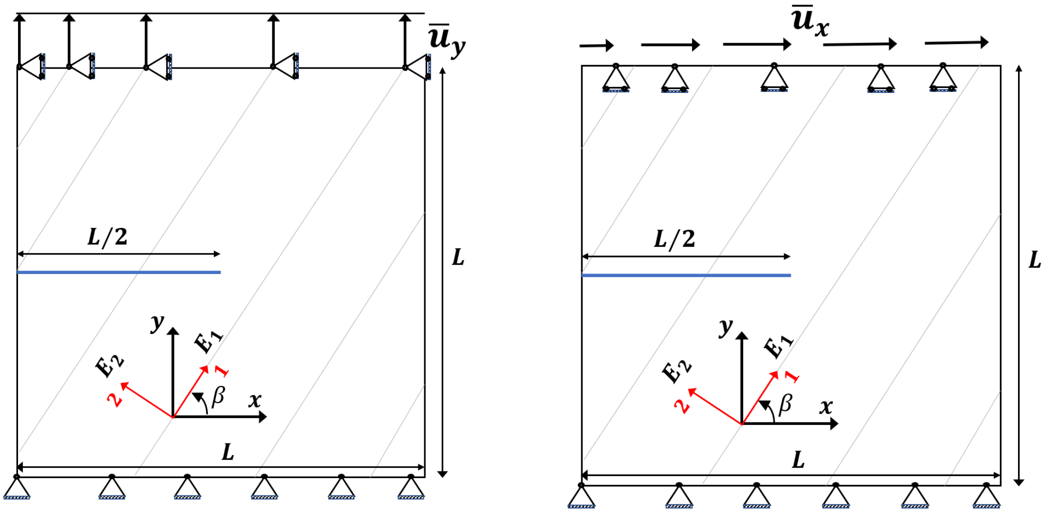

(a) (b)

Figure 4.3: Schematics of the square plate with an initial edge crack under (a) the tensile loading, and (b) the shear loading. The material coordinate system is rotated by the angle β with respect to the original coordinate system xy.

Material properties	Values	Unit
ν_{21}, ν_{13}, ν_{12}	0.17, 0.3, 0.51	-
E_1, E_2 E_3	210, 70, 210	GPa
G_{23}, G_{13} G_{12}	46.02, 80.77, 46.02	GPa
$\mathcal{G}_c$	2.7	N/mm

Table 4.1: Material properties for the orthotropic material studied for validation with numerical results given by Ziaei-rad et al. [2023].

In the tensile case, a sufficiently small value for the characteristic length $l = 0.01$ mm is considered. The displacement controlled loading is monotonically increased with a constant displacement increment $\Delta\bar{u}_y = 0.\bar{1} \times 10^{-2}$ mm until the ultimate step at $\bar{u}_y = 0.\bar{1} \times 10^{-1}$ mm. In the following, the results of the fracture path and the load-displacement relationship are given for three sets of material orientation: $\beta = 0, -\pi/4, \pi/2$.

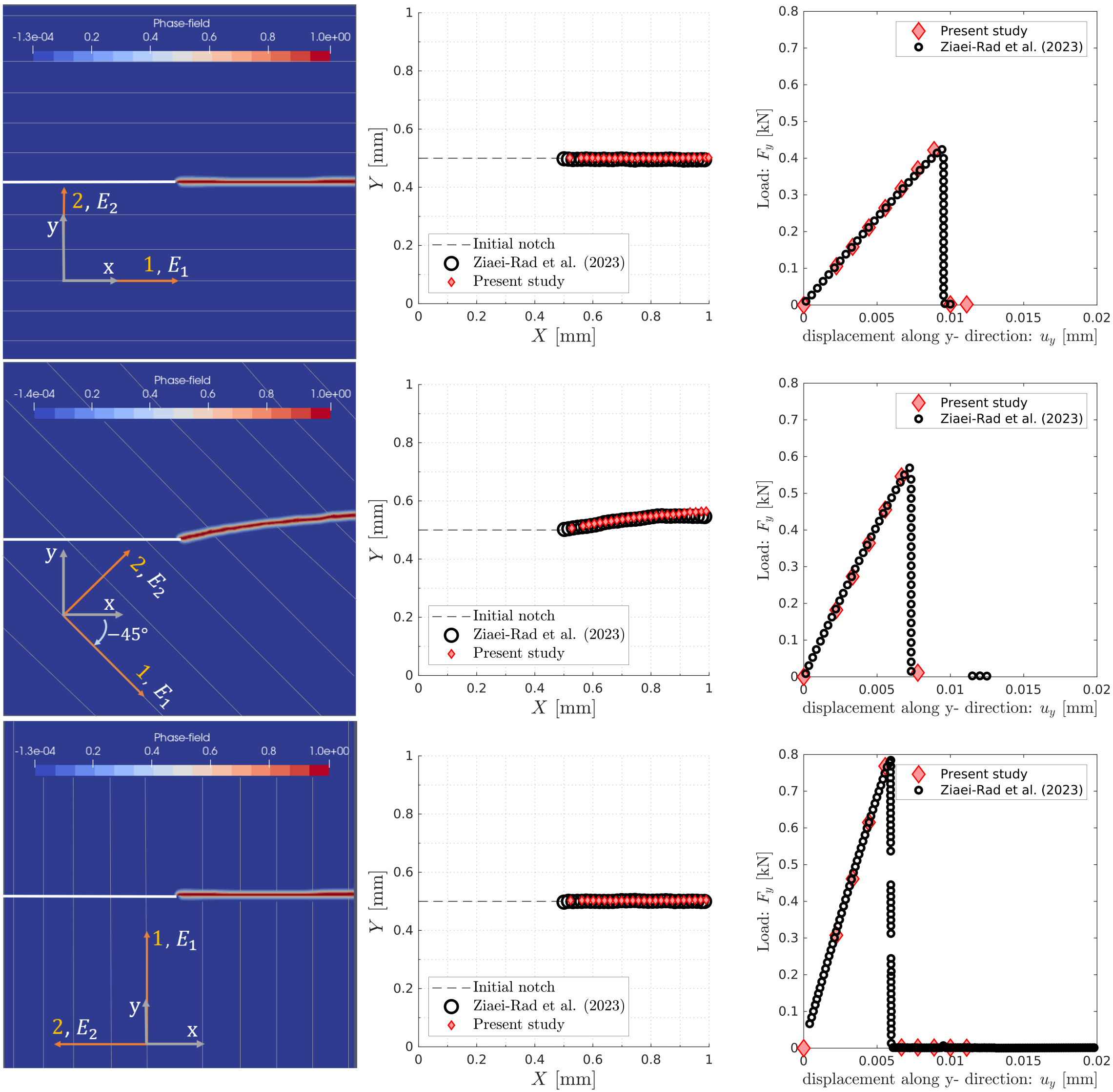

(a) (b) (c)

Figure 4.4: (a) Phase-field evolution, and comparison of (b) the fracture path, and (c) the load-displacement relationship for the cracked square plate under tensile loading: present study vs. Ziaei-rad et al. [2023].

As shown in Figure 4.4, the results simulated in our study illustrate a remarkable agreement with the findings reported by Ziaei-rad et al. [2023]. Notably, when the fracture deviates or kinks from the initial notch (i.e. at the material orientation $\beta = -\pi/4$), the propagation follows the weaker direction of the material in terms of elasticity. However, an intriguingly different fracture pattern is observed when the top side is unconstrained along the x-direction: in such cases, the propagation occurs on the strong direction of the material in elasticity as (see Figure 4.5). This seemingly insignificant difference in the boundary condition has a profound impact on the fracturing behavior, resulting in distinct fracture patterns observed in Ziaei-rad et al. [2023]; Dijk et al. [2020]; Hirshikesh et al. [2021].

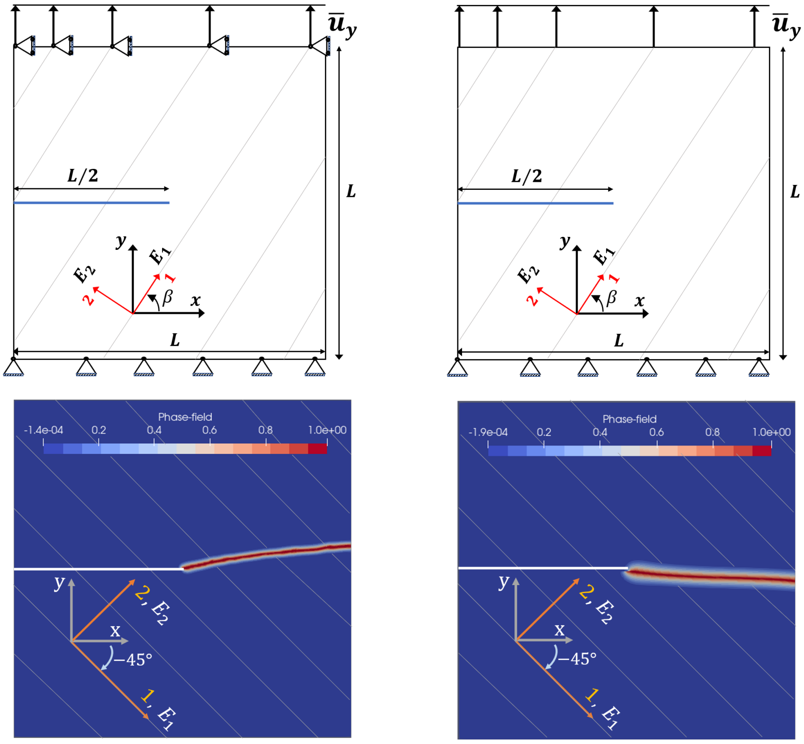

(a) (b)

Figure 4.5: The effect of boundary conditions on the phase-field trajectory of a square plate with a material orientation of $\beta = -\pi/4$. (a) the top side of the plate is constrained along the x-direction, leading to the propagation on the weaker direction of the material in elasticity [Dijk et al., 2020; Ziaei-rad et al., 2023]. (b) the top side is free to move along the x-direction, leading to the propagation on the strong direction of the material in elasticity [Hirshikesh et al., 2021].

In the shearing, a sufficiently small value for the characteristic length $l = 0.02$ mm is considered. The displacement controlled loading is monotonically increased with a constant displacement increment $\Delta\bar{u}_{\mathrm{x}} = 0.\bar{4} \times 10^{-3}$ mm until the last step at $\bar{u}_{\mathrm{x}} = 0.\bar{2} \times 10^{-1}$ mm. The results of the fracture path and the load-displacement relationship are given for four sets of material orientation: $\beta = 0, \pm\pi/4, \pi/2$. While these two simulations show good agreement in predicting the fracture path, there is a considerable discrepancy in the load-displacement relationship between the two studies.

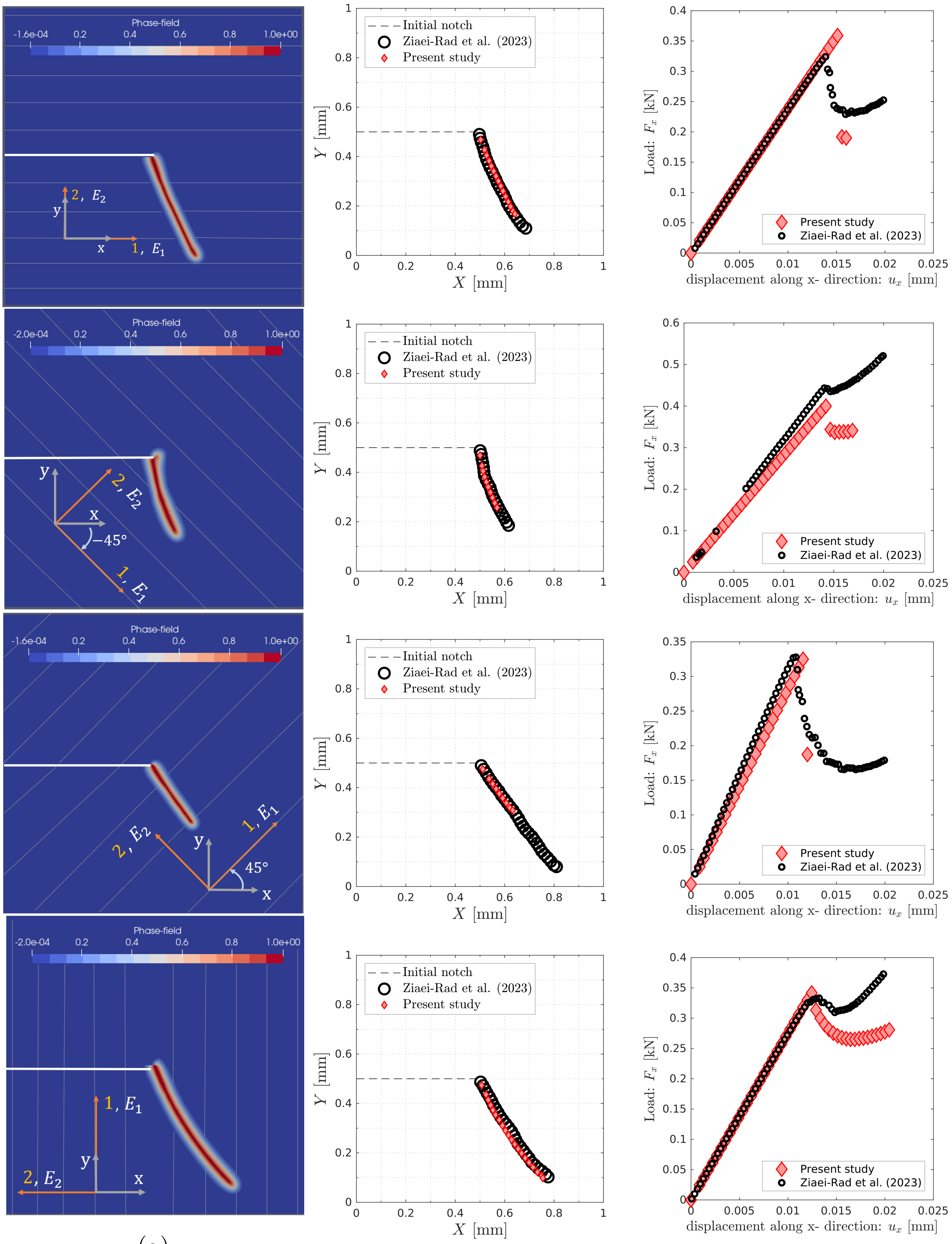

(a) (b) (c)

Figure 4.6: Phase-field evolution, and comparison of (b) the fracture path, and (c) the load-displacement relationship for the cracked square plate under shear loading: present study vs. Ziaei-rad et al. [2023].

The discrepancy observed in the load-displacement relationship for the shearing case can be attributed to the differences between the models and characteristic lengths employed in the simulations; while Ziaei-rad et al. [2023] employed AT-2 with a characteristic length of $l = 0.008$ mm, the present study utilized the combination of AT-1 with a characteristic length almost twice as large particularly for the shearing. We, therefore observer a sharper drop in the loading of the AT-1 model upon reaching the onset of cracking, similar to the findings in the homogeneous 1D problem studied by Kristensen et al. [2021]. Nevertheless, this inconsistency between the models is expected to diminish gradually as the characteristic length approaches zero, and a sharp crack emerges. Under such conditions, both models converge towards the principles of linear elastic fracture mechanics with an infinite material strength.

It is worth noting that in both cases, a region next to the top side of the plate tends to exhibit phase-field evolution, which needs to be hindered. Indeed, the evolution of the phase field near the boundaries precedes the development of cracks along the primary notch. This phenomenon can be primarily attributed to the Dirichlet boundary conditions, which constrain all the top nodes in the transverse direction of the applied displacement, leading to singularities in the stress-strain fields. To counteract the undesired evolution of the phase field near these boundaries, an additional Dirichlet boundary condition is applied on the phase field, specifically setting $\alpha = 0$ in this region. While this approach effectively facilitates the intended propagation of fractures, it is necessary to investigate how a decomposition model can independently address the singularity without applying additional conditions on the model, necessitating subsequent modifications. However, such analysis is beyond the scope of this study, as long as it does not affect the phase-field evolution originating from the initial crack tip.

4.4.2 Validation with experimental data

To the best of our knowledge, the robustness of the proposed generalized Miehe decomposition has not been thoroughly examined through direct comparison with experimental results. Therefore, this study aims to adopt the model and investigate its performance in simulating fracture propagating from an initial notch with a length of a in a semi-circular specimen subjected to an asymmetrical bending setup, as described by Sakha et al. [2022].

In the classical semi-cicular bend (SCB) test, the mode-mixity λ, defined as $\lambda = K_{\mathrm{II}}/(K_{\mathrm{I}}^2 + K_{\mathrm{II}}^2)^{1/2}$, varies as the material orientation changes relative to the initial notch (shown as β in Figure 4.7). Therefore, Nejati et al. [2019a] proposed the asymmetrical SCB configuration for orthotropic materials, which allows us to control the mixed-mode I/II loading at each material orientation, by simply varying the span ratios S_2/S_1 while keeping the ratio $S_1/R = 0.8$ constant (see Figure 4.7). Following this setup, the results of 37 fracture toughness tests on the metamorphic Grimsel Granite, which exhibits transversely isotropic behavior with the isotropy plane coinciding with its foliation plane, under two different mixed-mode loading are compared with the generalized Miehe phase-field simulations. By doing so, we can assess the model's predictive capability and its ability to capture the fracture behavior of orthotropic materials under complex mixed-mode loading conditions.

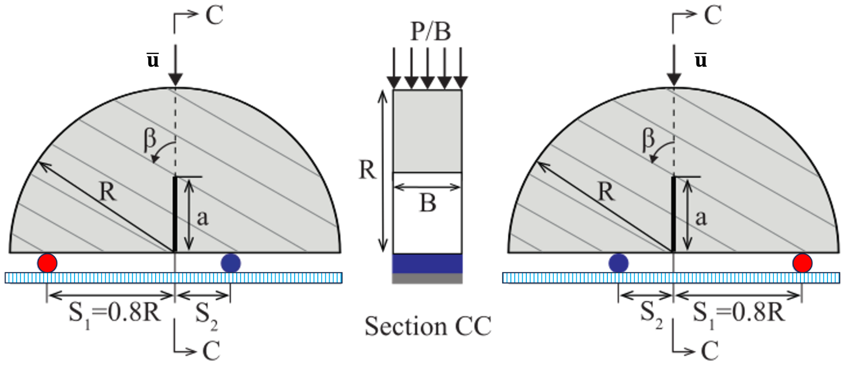

(a) $K_{II}/K_I \leq 0$ **(b)** $K_{II}/K_I > 0$

Figure 4.7: Schematics of the SCB test setup for two types of mixed-mode loading (a) $K_{\mathrm{II}}/K_{\mathrm{I}} \leq 0$, and (b) $K_{\mathrm{II}}/K_{\mathrm{I}} > 0$.

In this analysis, two mode-mixity ratios, namely $\lambda = \pm 0.37$, are applied. Using finite element analysis in ABAQUS, the corresponding span ratios required to achieve the desired mode-mixity ratio at each material orientation can be calculated, as shown in Figure 4.8. Following the calculated span ratios, the lower supports of the specimen are constrained in the y-direction, while a specific support (marked in red in Figure 4.7) is also constrained in the x-direction. As shown in this figure, the red support corresponds to the right lower support when $K_{\mathrm{II}}/K_{\mathrm{I}} > 0$, and to the left lower support when $K_{\mathrm{II}}/K_{\mathrm{I}} \leq 0$. The displacement controlled loading is applied downward to the sample, and monotonically increased with a constant displacement increment $\Delta\bar{u} = -0.\bar{1}0 \times 10^{-2}$ mm.

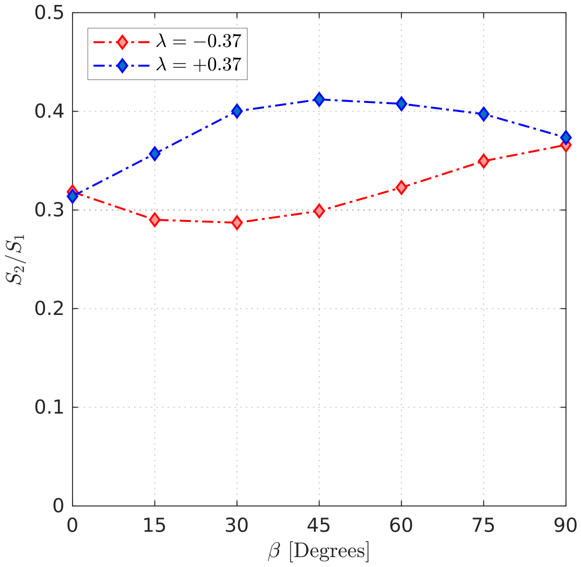

Figure 4.8: The variation of span ratios for different material orientations and mode-mixity ratios.

To apply the modified SCB test condition to the phase-field model, the radius of the semi-circular plate is taken as $R = 43.45$ mm with an initial vertical notch extending to the length of $a = 0.41R$. Assuming the plate undergoes the plane-strain condition, the thickness has no effect on the the critical stress intensity factors, K_{If} and K_{IIf}, calculated at the peak load P_{cr} as [Ayatollahi et al., 2006]

$$\begin{aligned} K_{\mathrm{If}} &= Y_{\mathrm{I}} \frac{P_{\mathrm{cr}}}{2Rt} \sqrt{\pi a} \\ K_{\mathrm{IIf}} &= Y_{\mathrm{II}} \frac{P_{\mathrm{cr}}}{2Rt} \sqrt{\pi a} \end{aligned} \tag{4.22}$$

where the coefficients Y_{I} and Y_{II} depend on both the geometrical factors and the material anisotropy. In other words, due to the proportional relationship of the peak load and sample thickness, the effect of thickness is nullified in Eq. 4.22. Therefore, one can calculate the effective fracture toughness $K^{\mathrm{c}}_{\mathrm{eff}}$, defined as $K^{\mathrm{c}}_{\mathrm{eff}} = (K^2_{\mathrm{If}} + K^2_{\mathrm{IIf}})^{1/2}$, in a model with a unity thickness. Considering these dimensions, the specimen is discretized by 40K linear quadrilateral elements, with the smallest mesh size of $h = 1.1 \times 10^{-2}$ mm for the region around the initial notch.

Table 4.2 provides the mechanical properties of Grimsel Granite, as given in Sakha et al. [2022]. The experimental study on Grimsel Granite has shown that the mode I fracture toughness $K_{\mathrm{Ic}}(\phi)$ of this material follows a sinusoidal variation of the fracture toughness values in the principal directions 1 (along the foliation) and 2 (normal to the foliation) [Nejati et al., 2020b]. Assuming ϕ as the direction of fracture growth with respect to the principal direction 1, the directional dependency of the fracture toughness $\mathcal{G}_{\mathrm{c}}(\phi)$ is governed by the function defined in Table 4.3. Given the mechanical properties of Grimsel Granite, the polar plot of its fracture toughness is shown in Figure 4.9. Despite the considerable directional dependency of the fracture toughness $\mathcal{G}_{\mathrm{c}}(\phi)$ observed in this figure, we only treat Grimsel Granite as a transversly isotropic material in terms of elasticity, and thus the direction-independent circular polar plot in Figure 4.9 represents the fracture toughness across all directions. This flaw unquestionably leads to inaccuracy in the model predictions, and emphasizing the necessity of addressing it in future developments.

Material properties	Values	Unit
ν_{21}, ν_{13}, ν_{12}	0.15, 0.3, 0.3	-
E_1, E_2 E_3	36, 18, 36	GPa
G_{23}, G_{13} G_{12}	10, 13.85, 10	GPa
$K_{\mathrm{Ic},1}$, $K_{\mathrm{Ic},2}$	0.78, 1.35	MPa$\sqrt{\mathrm{m}}$
L_{c}	10	mm

Table 4.2: Material properties for the Grimsel Granite taken from Sakha et al. [2022].

Variation of fracture toughness
$K_{\mathrm{Ic}}(\phi) = K_{\mathrm{Ic},1}\cos^2\phi + K_{\mathrm{Ic},2}\sin^2\phi$
$\mathcal{G}_{\mathrm{c}}(\phi) = \dfrac{K_{\mathrm{Ic}}^2(\phi)}{2E_1}\left(\kappa_2\left(\xi + \sqrt{\xi}\right)\cos^2\phi + \kappa_1\left(\sqrt{\xi}+1\right)\sin^2\phi\right)$

Table 4.3: The directional dependency of the different measures of fracture toughness adopted from Nejati et al. [2020b, 2021a]. The parameters ξ, and κ_{i}s are related to the elastic constants through the definition given by Sakha et al. [2022].

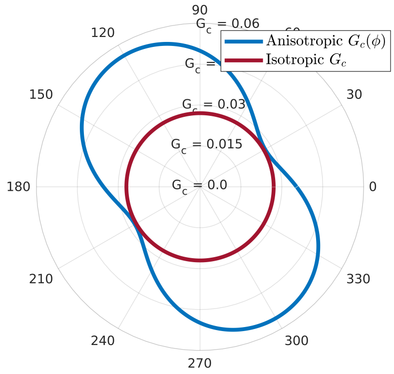

Figure 4.9: Polar plot of the fracture toughness for Grimsel Granite (a) as a transversely isotropic material under plane-strain condition, and (b) assumed as an isotropic solid. The fracture toughness is given in N/mm

To accurately capture the phase-field evolution, a sufficiently small characteristic length is employed in this study. Considering the dimension of the sample, the characteristic length is chosen as $0.02R$. The choice of a small characteristic length is motivated by the significant size of the fracture process zone in Grimsel Granite compared to the sample size. As indicated in Table 4.2, the ratio of L_{c}/R (fracture process zone length to the sample radius) is approximately 0.23. This highlights the relatively large extent of the fracture process zone in relation to the specimen dimensions. Indeed, using the actual size of the fracture process zone as the characteristic length would lead to inaccuracies in the phase-field evolution. It should be noted that the chosen small characteristic length may result in underestimation of the load-displacement relationship in our modelling.

In this study, it is observed that the phase-field may initially evolve in the vicinity of the lower supports and the loading zone, again preceding the development of crack along the primary notch. This preceding evolution, caused by the abrupt change of constraints exclusively applied to a subset of nodes on the supports and loading zone, as opposed to their freely constrained neighbors, should ideally have been controlled by the decomposition model. However, the decomposition model used in our study was apparently unable to address this issue. To suppress this undesired evolution in the potential region, one can apply a Dirichlet condition to the phase-field variable, provided that the ultimate phase-field evolution is not affected.

Figure 4.10 and 4.11 illustrate the results simulated by the generalized Miehe decomposition phase-field model, depicting the effective fracture toughness $K_{\mathrm{eff}}^{\mathrm{c}}$ and corresponding kink angles θ_0 for two mixed-mode loading ratios $\lambda = \pm 0.37$. The results are compared alongside the scatter of the experimental data, as well as predictions from three different fracture growth criteria utilized in Sakha et al. [2022]. Note that, in the phase-field simulation, we measure the kink angle by considering the slope of the tangent line to the fracture path within the region corresponding to the fracture process zone size of Grimsel Granite, as given in Table 4.2. The subfigures labeled as (b) and (c) within these figures, respectively, indicate the displacement magnitude and the y-displacement associated with a particular material orientation, reaffirming the positioning of the fixed and moving supports in Figure 4.7 for each set of mixed-mode loading conditions.

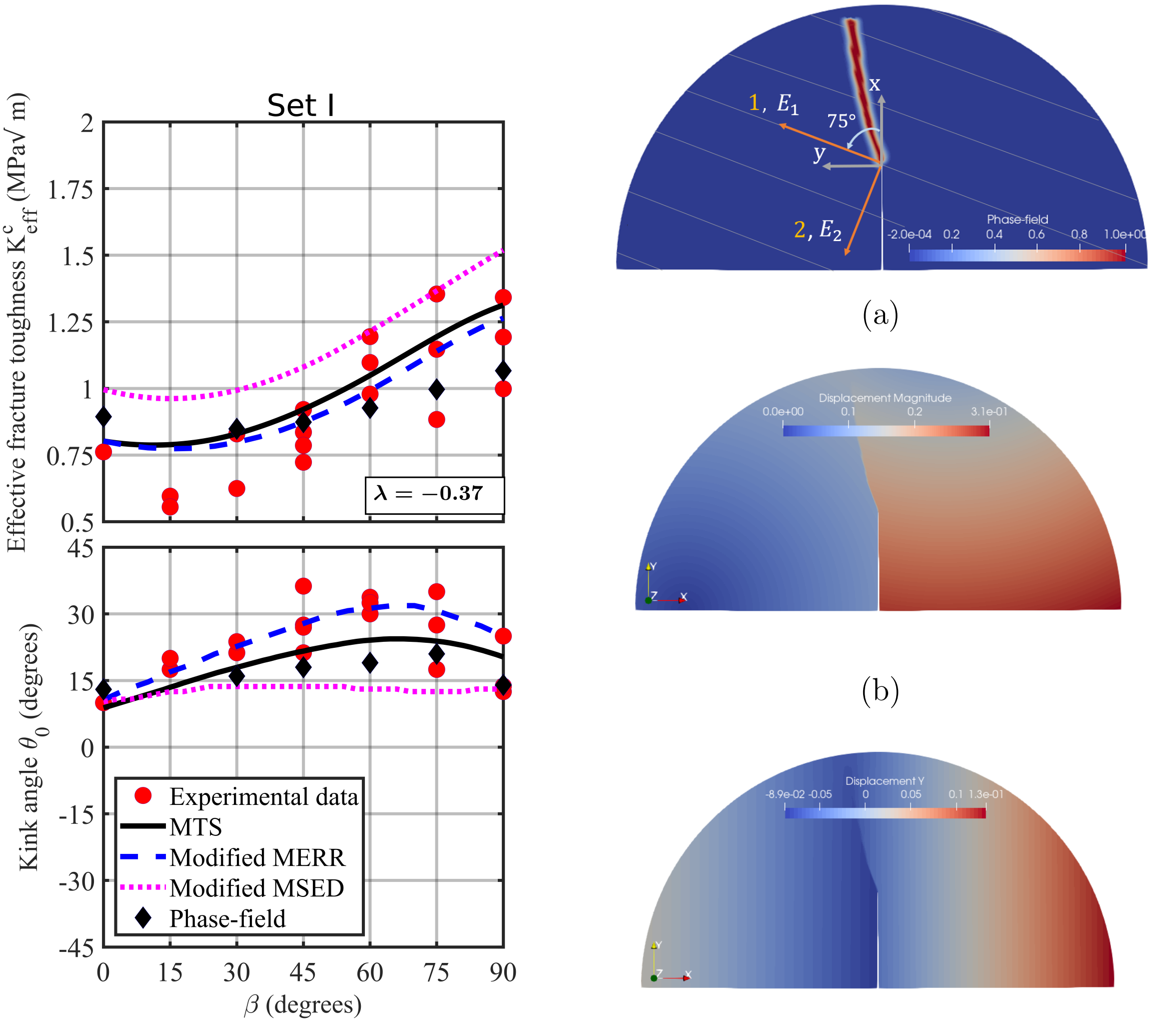

(a)

(b)

(c)

Figure 4.10: Comparison of the experimental data on the kink angle, θ_0, and the effective fracture toughness, $K^{\mathrm{c}}_{\mathrm{eff}}$, with the phase-field simulations and the predictions reported by Sakha et al. [2022] based on the MTS, modified MERR, and modified MSED criteria for the mode-mixity $\lambda = -0.37$. (a) Evolution of phase-field, (b) displacement magnitude (in mm), and (c) y-displacement (in mm) for material orientation $\beta = 75°$.

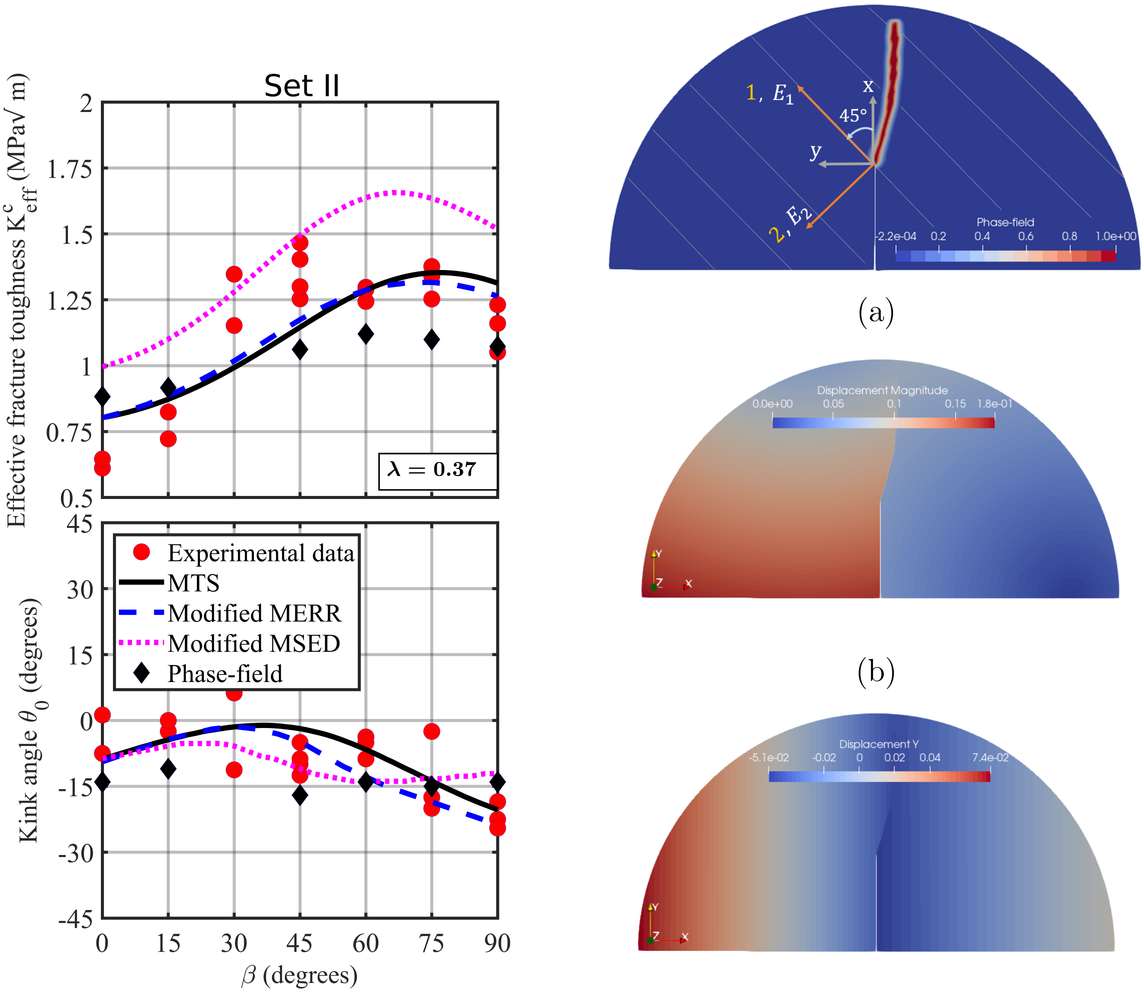

(a)

(b)

(c)

Figure 4.11: Comparison of the experimental data on the kink angle, θ_0, and the effective fracture toughness, $K^{\mathrm{c}}_{\mathrm{eff}}$, with the phase-field simulations and the predictions reported by Sakha et al. [2022] based on the MTS, modified MERR, and modified MSED criteria for the mode-mixity $\lambda = 0.37$. (a) Evolution of phase-field, (b) displacement magnitude (in mm), and (c) y-displacement (in mm) for material orientation $\beta = 45°$.

Figure 4.10 and 4.11 reveal that how well the generalized Miehe decomposition model was capable to capture the fracture behavior in all the samples of transversely isotropic Grimsel Granite under mixed-mode loading conditions. It is noteworthy that the model successfully achieved these acceptable predictions despite lacking any knowledge of the material's directional dependency on fracture toughness. Based on the observations reported in Sakha et al. [2022], in the two mixed-mode loading ratios, the compressive stress distribution ahead the initial notch may dominate over the tensile driving forces when the material orientation is at high values (i.e. when the $\beta \geq 45°$), resulting in propagation within the compressive region if compression is allowed to drive fracture propagation. The current decomposition model, however, tracks the fracture path in regions located away from the compressive zones highlighted in Sakha et al. [2022].

Sakha et al. [2022] highlighted a drawback in the classical formulations of the energy-based criteria, necessitating decomposition of shearing and opening contributions, especially under significantly high mode-mixity ratios. In response to this drawback, the modified maximum energy release rate (MERR) and the modified maximum strain energy density (MSED) were introduced to address this drawback, effectively enhancing the predictions of energy-based criteria. While this drawback can be tolerable for sets with low mode-mixity ratios ($\lambda = \pm 0.37$) without compromising prediction accuracy, one need to decompose the shearing and opening contributions in sets where the fracture kinks under a high mixed-mode loading. In the framework of phase-field modeling, this decomposition can be introduced only to the strong form of governing equations, resulting in a variationally inconsistent approach for which a robust argument has yet to be established [Zhuang et al., 2022]. The other obstacle to decomposing shearing and opening, particularly lies in the definition of the Generalized Miehe driving force Ψ_+, which cannot practically differentiate the opening and shearing driving terms [Zhuang et al., 2022]. Hence, to improve phase-field predictions and extend its applicability to scenarios with higher mode-mixity ratios, these two limitations need to be understood in further studies.

Similar to the present study, Mehraban et al. [2023] utilized a non-local XFEM-based method to reproduce the experimental data presented in Sakha et al. [2022]. Apart from addressing the directional dependency of fracture toughness in Grimsel Granite, Mehraban et al. [2023] incorporated rigid body models for the supports, which exerted hard contact interactions while assuming frictionless conditions at the interfaces. This difference in the modeling approaches reveals another source of inaccuracy in our modeling methodology. Indeed, in our current approach, only one node is constrained at the interface, which may not fully represent the complex conditions governing the experimental setup. Deformation of the sample at the contact points can lead to interactions with more than one node at the interface, which must be addressed in future enhancements of our modeling methodology.

4.5 Conclusion

In this paper, we have adopted the generalized Miehe decomposition model to effectively simulate fracturing in orthotropic solids. We validated the accuracy of our implementation by comparing our results with existing numerical studies in the literature. Furthermore, we have successfully demonstrated the reliability and robustness of the decomposition model by reproducing experimental data pertaining to fracture trajectory and the effective fracture toughness of transversely isotropic rock samples subjected to mixed-mode loading.

While the previous study illustrated the potential of interpenetration in cases where no treatment is incorporated, our model is capable of accurately capturing the fracturing phenomenon even in the presence of inherent flaws in the modeling process. One of the significant limitations we have identified is the exclusion of the directional dependency of fracture toughness. This omission can overshadow the impact of material tendency interacting with the loading conditions, which ultimately determines the trajectory of the fracture. Considering a material with a suppressed tendency, the applied loading can exert a dominant influence and facilitate the propagation of the fracture, leading to an underestimation of the effective fracture toughness.

Chapter 5

Conclusions and outlook

This thesis culminates with a comprehensive analysis of complex fracturing of anisotropic rocks, encompassing its main discoveries and outlining future directions for further research. Up to this point, the introduction focused on unraveling the fundamental physical concepts that underlie rock fracture mechanics. In addition, we identified existing knowledge gaps, and proposed a coherent framework to unite these disparate aspects. Throughout each chapter, we followed a structured methodology, using simplifying assumptions to gain deeper insights into fracture mechanics. Consequently, every chapter concluded with specific key findings tailored to its section. In this concluding chapter, we will not repeat all individual findings but instead focus on elucidating the correlations between these discoveries, creating a holistic view of the physics we have grasped. Nonetheless, this meaningful picture forms only a portion of a broader puzzle, requiring further development in subsequent stages. The outlook section of this thesis will offer a roadmap for future research, identifying potential challenges and outlining strategies to overcome them. In conclusion, while this thesis has made significant strides in establishing reliable theories and models for capturing fracture in anisotropic rock under complex loading, there remain untaken steps towards achieving a comprehensive rock fracture modeling. Hence, the insightful findings presented here serve as a foundation for further advancements in this field.

5.1 Unveiling the role of material anisotropy

Material anisotropy in fracture mechanics manifests itself in various mechanical aspects, including elasticity, fracture toughness, and strength. Throughout this research, our focus was on unveiling the influence of material anisotropy on fracture initiation and propagation, especially when the loading conditions are not in favor of the material's natural fracture tendency. We have now gained a clear understanding that in such cases, fracture initiation and propagation are governed by a prevailing interplay between these factors. The level of material anisotropy plays a crucial role, as lower anisotropy allows the loading condition to dominate more easily. However, when the loading condition overcomes the material's inherent tendencies, rock heterogeneity comes into play, resulting in transgranular dominance micro-cracking, which leads to scattered experimental observations.

Beyond loading conditions, the presence of material anisotropy may heighten the importance of other factors in determining fracturing behavior. For example, the influence of T-stress within the fracture process zone becomes more pronounced when material anisotropy is in play. In Chapter 4, we have also discussed the impact of minor changes in boundary conditions, especially when fractures kink due to material anisotropy. Interestingly, the structure size effect in hydraulic fracture initiation could not be linked to the degree of material anisotropy, as elaborated in Chapter 3.

By deciphering the strong impact of material anisotropy, we unlocked valuable insights into fracturing within direction-dependent formations. These insights, however, still fall short of fully capturing brittle fracturing in anisotropic rocks, given the uncertainties associated with using deterministic homogeneous-based models. Addressing these uncertainties is a prospect for future studies.

5.2 Fracture path: not a priori assumption

The fracture path, during initiation and propagation, remains a complex unknown until the fracture extends beyond the region where it is driven by either material's tendency or loading conditions. In contrast to many previous studies that make a priori assumption about fracture paths, our research sought to investigate the degree of tortuosity near the wellbore. This tortuosity is a unwanted outcome in hydraulic fracturing that requires strategies to either mitigate the degree of fracture reorientation or confine it to a smaller zone.

Through an analysis of hydraulic fracture initiation and propagation in anisotropic rock formations, our findings underscore the critical importance of considering anisotropy in rock formations. Neglecting this aspect can lead to a significant divergence between our theoretical predictions of fracture paths and the reality of their behavior. The hazards associated with wellbore region tortuosity can be effectively minimized through a comprehensive comprehension of the dynamic interplay between material properties and loading conditions, leading to configurations that promote less winding fracture path. Now, one can easily leverage from the data set we have provided for hydraulic fracture initiation, come up with an optimized configuration for the initial conditions which enables the hydraulic fracture to be driven in a less tortuous manner.

5.3 Toward a sophisticated fracture model

Throughout this research, we have tried to convey a crucial message: a comprehensive model in fracture mechanics must have the capability to capture brittle fracturing, accounting for size effects under complex loading and different degrees of material anisotropy. Such a model should prevent fracturing under interpenetration while understanding the contributions of shearing and opening in driving brittle fractures in rock-type materials. Irrespective of the fracture mechanism, materials with sufficiently large fracture process zones should consider the effect of the material's lengthscale, in addition to the sample's lengthscale. We have learned that neglecting any of these physical concepts distorts the real understanding of fracture behavior. Another key finding of this study is that while numerous models have been suggested for quasi-brittle materials, one can still employ brittle fracture models with minor modifications, as long as certain requirements of brittle fracturing are met. By enhancing the simplicity of brittle fracture models and incorporating additional physical concepts, this paper extends the applicability of these models to more complex materials, such as quasi-brittle anisotropic rocks under complex loading conditions.

In addition to modifying fracturing models and theories, this thesis also encompasses the developing of computational codes and finite element models, which is immensely valuable for future research. Among these indispensable tools is the Generalized Miehe Decomposition module (GMIEHE) developed for orthotropic materials, which has been incorporated into the phase-field code known as GRIPHFiTH [1]. This aspect of the thesis marks a significant stride toward the establishment of a robust computational tool capable of accurately simulating hydraulic fracture growth in anisotropic rock-type formations. By incorporating direction-dependent fracture toughness into the GMIEHE module, we are equipped with a powerful tool for comprehending the extent to which hydraulic fractures can reorient around the wellbore. This advancement provides a practical framework for addressing and mitigating the tortuosity of hydraulic fractures, offering novel solutions for real-world geo-engineering applications.

---

[1] `https://gitlab.ethz.ch/compmech/GRIPHFiTH`

5.4 Outlook

With all the necessary groundwork laid for the next steps, our focus now lies in outlining future research towards a more comprehensive model for capturing fracture initiation and propagation in rock-like materials. Let's begin by addressing the flaws that need attention in phase-field modeling. An initial attempt towards a more comprehensive phase-field model involves incorporating direction-dependent fracture toughness and evaluating its reliability in predicting fracture paths under higher mode-mixities. As seen in Chapter 2, the model may encounter challenges when not decomposing the contribution of shearing and opening, potentially leading to inaccuracies in fracturing predictions. Another area of interest is studying whether the solely tension-compression decomposition suffices in capturing the evolution of wing and secondary cracks when the central crack experiences compressive loading. As per the conclusions drawn in Chapter 2, introducing an additional decomposition in such loading scenarios might be necessary, making the development of the phase-field model a prerequisite for further progress.

Shifting our attention to Chapter 3, substantial data has been presented on the initiation parameters crucial for hydraulic fracture initiation. As highlighted earlier, precise determination of these initiation parameters is essential, as arbitrary assumptions can significantly influence the subsequent fracture growth trajectory, leading to deviation from the actual fracture growth behavior. However, this thesis has yet to explore the potential effects of realistic conditions that may deviate from the underlying assumptions made in this study. Notably, during drilling, defects can be introduced around the wellbore, contradicting our assumption of an initially notch-free wellbore. If the extent of these defects proves significant in comparison to the initiation length, it could have a notable impact. Furthermore, this thesis now prompts another question of whether transitioning from the plane-stress to the plane-strain condition could indeed influence the initiation parameters. Such inquiries must be addressed in future studies.

Once the initial condition of hydraulic fracture growth is well-established, the modified phase-field model, tailored for hydraulic fracturing, can be leveraged to track the trajectory of hydraulic fracture propagation. However, up to this point, our primary question revolving around understanding the tortuosity around the wellbore and how it is influenced by the interplay of material and stress anisotropy remains unresolved.

In addition to this question, we also have concerns about seismic hazards induced by hydraulic fracturing, necessitating a clearer understanding of the stability of hydraulic fracture propagation within the subsurface. The complexities arising from the material and loading conditions within the subsurface introduce uncertainties that blur the long-term certainty in geo-engineering applications. Addressing these challenges requires the gradual development of a more sophisticated model through scientific research endeavors. Only with such advancements we can hope to provide reliable answers to the complexities and uncertainties in geo-engineering applications.

Bibliography

Agrawal, V., Runnels, B., 2021. Block structured adaptive mesh refinement and strong form elasticity approach to phase field fracture with applications to delamination, crack branching and crack deflection. Computer Methods in Applied Mechanics and Engineering 385, 114011.

Akbardoost, J., Ayatollahi, M.R., 2014. Experimental analysis of mixed mode crack propagation in brittle rocks: The effect of non-singular terms. Engineering Fracture Mechanics 129, 77–89.

Amadei, B., 1983. Rock Anisotropy and the Theory of Stress Measurements. 1 ed., Springer-Verlag Berlin Heidelberg.

Amann, F., Gischig, V., Evans, K., Doetsch, J., Jalali, R., Valley, B., Krietsch, H., Dutler, N., Villiger, L., Brixel, B., Klepikova, M., Kittilä, A., Madonna, C., Wiemer, S., Saar, M.O., Loew, S., Driesner, T., Maurer, H., Giardini, D., 2018. The seismo-hydromechanical behaviour during deep geothermal reservoir stimulations: open questions tackled in a decameter-scale in-situ stimulation experiment. Solid Earth 9, 115–137.

Ambati, M., 2017. Phase-field modeling and computations of brittle and ductile fracture for solids and shells. Ph.D. thesis. Technische Universität Carolo-Wilhelmina zu Braunschweig.

Ambrosio, L., Tortorelli, V.M., 1990. Approximation of functional depending on jumps by elliptic functional via t-convergence. Communications on Pure and Applied Mathematics 43, 999–1036.

Amor, H., Marigo, J.J., Maurini, C., 2009. Regularized formulation of the variational brittle fracture with unilateral contact: Numerical experiments. Journal of the Mechanics and Physics of Solids 57, 1209–1229.

Arakere, N.K., Knudsen, E., Wells, D., McGill, P., Swanson, G.R., 2008. Determination of mixed-mode stress intensity factors, fracture toughness, and crack turning angle for anisotropic foam material. International Journal of Solids and Structures 45, 4936–4951.

Argatov, I.I., Nazarov, S.A., 2002. Energy release caused by the kinking of a crack in a plane anisotropic solid. Journal of Applied Mathematics and Mechanics 66, 491–503.

Atkinson, C., Thiercelin, M., 1993. The interaction between the wellbore and pressure-induced fractures. International Journal of Fracture 59, 23–40.

Ayatollahi, M.R., Aliha, M.R., 2006. On determination of mode II fracture toughness using semi-circular bend specimen. International Journal of Solids and Structures 43, 5217–5227.

Ayatollahi, M.R., Aliha, M.R., 2008. On the use of Brazilian disc specimen for calculating mixed mode I-II fracture toughness of rock materials. Engineering Fracture Mechanics 75, 4631–4641.

Ayatollahi, M.R., Aliha, M.R., Hassani, M.M., 2006. Mixed mode brittle fracture in PMMA - An experimental study using SCB specimens. Materials Science and Engineering A 417, 348–356.

Ayatollahi, M.R., Aliha, M.R.M., Saghafi, H., 2011. An improved semi-circular bend specimen for investigating mixed mode brittle fracture. Engineering Fracture Mechanics 78, 110–123.

Ayatollahi, M.R., Nejati, M., Ghouli, S., 2020. The finite element over-deterministic method to calculate the coefficients of crack tip asymptotic fields in anisotropic planes. Engineering Fracture Mechanics 231, 106982.

Ayatollahi, M.R., Rashidi Moghaddam, M., Berto, F., 2015. A generalized strain energy density criterion for mixed mode fracture analysis in brittle and quasi-brittle materials. Theoretical and Applied Fracture Mechanics 79, 70–76.

Azhdari, A., Nemat-Nasser, S., 1996. Energy-release rate and crack kinking in anisotropic brittle solids. Journal of the Mechanics and Physics of Solids 44, 929–951.

Azhdari, A., Nemat-Nasser, S., 1998. Experimental and computational study of fracturing in an anisotropic brittle solid. Mechanics of Materials 28, 247–262.

Bahrami, B., Nejati, M., Ayatollahi, M.R., Driesner, T., 2020. Theory and experiment on true mode II fracturing of rocks. Engineering Fracture Mechanics 240, 107314.

Bazant, Z.P., 2000. Size effect. International Journal of Solids and Structures 37, 69–80.

Bazant, Z.P., Kazemi, M.T., 1990. Determination of fracture energy , process zone length and brittleness number from size effect. International Journal of Fracture 44, 111–131.

Bažant, Z.P., Le, J.L., Salviato, M., 2022. Quasibrittle Fracture Mechanics and Size Effect. Oxford University Press.

Berryman, J.G., 2016. Role of fluid injection in the evolution of fractured reservoirs. International Journal of Engineering Science 103, 45–58.

Bobet, A., Einstein, H.H., 1998. Fracture coalescence in rock-type materials under uniaxial and biaxial compression. International Journal of Rock Mechanics and Mining Sciences 35, 863–888.

de Borst, R., Remmers, J.J., Needleman, A., Abellan, M.A., 2004. Discrete vs smeared crack models for concrete fracture: Bridging the gap. International Journal for Numerical and Analytical Methods in Geomechanics 28, 583–607.

Bourdin, B., Chukwudozie, C., Yoshioka, K., 2012. A variational approach to the numerical simulation of hydraulic fracturing, in: the 2012 SPE Annual Technical Conference and Exhibition (ATCE), San Antonio, Texas.

Bourdin, B., Francfort, G.A., Marigo, J.J., 2008. The Variational Approach to Fracture. Journal of Elasticity 91, 5–148.

Bryant, E.C., Sun, W.C., 2018. A mixed-mode phase field fracture model in anisotropic rocks with consistent kinematics. Computer Methods in Applied Mechanics and Engineering 342, 561–584.

Buczek, M.B., Herakovich, C.T., 1985. A Normal Stress Criterion for Crack Extension Direction in Orthotropic Composite Materials. Journal of Composite Materials 19, 544–553.

Cahill, L.M., Natarajan, S., Bordas, S.P., O'Higgins, R.M., McCarthy, C.T., 2014. An experimental/numerical investigation into the main driving force for crack propagation in uni-directional fibre-reinforced composite laminae. Composite Structures 107, 119–130.

Carloni, C., Nobile, L., 2002. Crack initiation behaviour of orthotropic solids as predicted by the strain energy density theory. Theoretical and Applied Fracture Mechanics 38, 109–119.

Carloni, C., Nobile, L., 2005. Maximum circumferential stress criterion applied to orthotropic materials. Fatigue and Fracture of Engineering Materials and Structures 28, 825–833.

Carter, B.J., 1992. Size and stress gradient effects on fracture around cavities. Rock Mechanics and Rock Engineering 25, 167–186.

Carter, B.J., Lajtai, E.Z., Yuan, Y., 1992. Tensile fracture from circular cavities loaded in compression. International Journal of Fracture 57, 221–236.

Chang, J.H., Pu, L.P., 1996. Finite element calculation of energy release rate prior to crack kinking in 2-D solids. International Journal for Numerical Methods in Engineering 39, 3033–3046.

Chen, C.S., Pan, E., Amadei, B., 1998. Fracture Mechanics Analysis of Cracked Discs of Anisotropic Rock Using the Boundary Element Method. International Journal of Rock Mechanics and Mining Sciences 35, 195–218.

Chengyong, W., Peide, L., Rongsheng, H., Xiutang, S., 1990. Study of the fracture process zone in rock by laser speckle interferometry. International Journal of Rock Mechanics and Mining Sciences and 27, 65–69.

Chertov, M., 2012. Closed-form solution for vertical fracture width in anisotropic elastic formations. International Journal of Rock Mechanics and Mining Sciences 53, 70–75.

Chong, Z., Karekal, S., Li, X., Hou, P., Yang, G., Liang, S., 2017. Numerical investigation of hydraulic fracturing in transversely isotropic shale reservoirs based on the discrete element method. Journal of Natural Gas Science and Engineering 46, 398–420.

Chukwudozie, C., Bourdin, B., Yoshioka, K., 2013. A Variational Approach to the Modeling and Numerical Simulation of Hydraulic Fracturing Under In-situ Stresses, in: Proceedings of 38th Stanford Geothermal Workshop.

Chukwudozie, C., Bourdin, B., Yoshioka, K., 2019. A variational phase-field model for hydraulic fracturing in porous media. Computer Methods in Applied Mechanics and Engineering 347, 957–982.

Cornetti, P., Muñoz-Reja, M., Mantič, V., 2022. Cohesive Crack Models and Finite Fracture Mechanics analytical solutions for FRP-concrete single-lap shear test: An overview. Theoretical and Applied Fracture Mechanics 122, 103529.

Cornetti, P., Pugno, N., Carpinteri, A., Taylor, D., 2006. Finite fracture mechanics: A coupled stress and energy failure criterion. Engineering Fracture Mechanics 73, 2021–2033.

Cotterell, B., Rice, J., 1980. Slightly curved or kinked cracks. International Journal of Fracture 16, 155–169.

Crouch, S., Starfield, A., 1983. Boundary element methods in solid mechanics: with applications in rock mechanics and geological engineering. Allen & Unwin.

Cuenot, N., Frogneux, M., Dorbath, C., Calo, M., 2011. Induced Microseismic Activity During Recent Circulation Tests At the Egs Site of Soultz-Sous-Forêts (France).

Dambly, M.L.T., Nejati, M., Vogler, D., Saar, M.O., 2019. On the direct measurement of the shear moduli in transversely isotropic rocks using the uniaxial compression test. International Journal of Rock Mechanics and Mining Sciences 113, 220–240.

David, E.C., Brantut, N., Schubnel, A., Zimmerman, R.W., 2012. Sliding crack model for nonlinearity and hysteresis in the uniaxial stress-strain curve of rock. International Journal of Rock Mechanics and Mining Sciences 52, 9–17.

De Lorenzis, L., Gerasimov, T., 2020. Numerical Implementation of Phase-Field Models of Brittle Fracture, in: Modeling in Engineering Using Innovative Numerical Methods for Solids and Fluids. Springer Cham. volume 599, pp. 75–101.

Dijk, N.P., Espadas-Escalante, J.J., Isaksson, P., 2020. Strain energy density decompositions in phase-field fracture theories for orthotropy and anisotropy. International Journal of Solids and Structures 196-197, 140–153.

Doetsch, J., Gischig, V.S., Villiger, L., Krietsch, H., Nejati, M., Amann, F., Jalali, M., Madonna, C., Maurer, H., Wiemer, S., Driesner, T., Giardini, D., 2018. Subsurface Fluid Pressure and Rock Deformation Monitoring Using Seismic Velocity Observations. Geophysical Research Letters 45, 10,389–10,397.

Doitrand, A., Sapora, A., 2020. Nonlinear implementation of Finite Fracture Mechanics: A case study on notched Brazilian disk samples. International Journal of Non-Linear Mechanics 119, 103245.

Dong, Z., Tang, S., 2019. Numerical study of near-wellbore hydraulic fracture propagation. Theoretical and Applied Fracture Mechanics 103.

Dutler, N., Nejati, M., Valley, B., Amann, F., Molinari, G., 2018. On the link between fracture toughness, tensile strength, and fracture process zone in anisotropic rocks. Engineering Fracture Mechanics 201, 56–79.

Dutler, N., Valley, B., Gischig, V., Jalali, M., Brixel, B., Krietsch, H., Roques, C., Amann, F., 2020. Hydromechanical insight of fracture opening and closure during in-situ hydraulic fracturing in crystalline rock. International Journal of Rock Mechanics and Mining Sciences 135, 104450.

Eftekhari, M., Baghbanan, A., Hashemolhosseini, H., Amrollahi, H., 2015. Mechanism of fracture in macro- and micro-scales in hollow centre cracked disc specimen. Journal of Central South University 22, 4426–4433.

Elices, M., Guinea, G.V., Gómez, J., Planas, J., 2002. The cohesive zone model: Advantages, limitations and challenges. Engineering Fracture Mechanics 69, 137–163.

Erdogan, F., Gupta, G.D., Cook, T.S., 1973. Numerical solution of singular integral equations. Springer, Dordrecht. pp. 368–425.

Erdogan, F., Sih, G.C., 1963. On the crack extension in plates under plane loading and transverse shear. Journal of Basic Engineering 85, 519–525.

Fakhimi, A., Carvalho, F., Ishida, T., Labuz, J., 2002. Simulation of failure around a circular opening using CWFS model. International Journal of Rock Mechanics and Mining Sciences 39, 507–515.

Fakoor, M., Khezri, M.S., 2020. A micromechanical approach for mixed mode I/II failure assessment of cracked highly orthotropic materials such as wood. Theoretical and Applied Fracture Mechanics 109.

Fink, J., Heim, E., Klitzsch, N., 2022. State of the Art in Deep Geothermal Energy in Europe.

Francfort, G.A., Marigo, J.J., 1998. Revisiting brittle fracture as an energy minimization problem. Journal of the Mechanics and Physics of Solids 46, 1319–1342.

Freddi, F., Royer-Carfagni, G., 2009. Variational Models for Cleavage and Shear Fractures, in: In Proceedings ofthe XIXAIMETA Symposium.

Fu, P., Johnson, S.M., Carrigan, Charles, R., 2013. An explicitly coupled hydro-geomechanical model for simulating hydraulic fracturing in arbitrary discrete fracture networks. International Journal for Numerical and Analytical Methods in Geomechanics 37, 2278–2300.

Gao, H., Chiu, C.H., 1992. Slightly curved or kinked cracks in anisotropic elastic solids. International Journal of Solids and Structures 29, 947–972.

Gehne, S., 2018. A laboratory study of fluid-driven tensile fracturing in anisotropic rocks. Ph.D. thesis. University of Portsmouth.

Ghouli, S., Ayatollahi, M.R., Nejati, M., 2020. On higher order parameters in cracked composite plates under far-field pure shear. Fatigue and Fracture of Engineering Materials and Structures 43, 568–585.

Gischig, V.S., Doetsch, J., Maurer, H., Krietsch, H., Amann, F., Frederick Evans, K., Nejati, M., Jalali, M., Valley, B., Christine Obermann, A., Wiemer, S., Giardini, D., 2018. On the link between stress field and small-scale hydraulic fracture growth in anisotropic rock derived from microseismicity. Solid Earth 9, 39–61.

Gischig, V.S., Giardini, D., Amann, F., Hertrich, M., Krietsch, H., Loew, S., Maurer, H., Villiger, L., Wiemer, S., Bethmann, F., Brixel, B., Doetsch, J., Doonechaly, N.G., Driesner, T., Dutler, N., Evans, K.F., Jalali, M., Jordan, D., Kittilä, A., Ma, X., Meier, P., Nejati, M., Obermann, A., Plenkers, K., Saar, M.O., Shakas, A., Valley, B., 2020. Hydraulic stimulation and fluid circulation experiments in underground laboratories: Stepping up the scale towards engineered geothermal systems. Geomechanics for Energy and the Environment 24, 100175.

Goldstein, R.V., Shifrin, E.I., 2012. Conditions for Mode i crack deviation in orthotropic plane subjected to biaxial loading. International Journal of Engineering Science 61, 36–47.

Griffith, A.A., 1921. The phenomena of rupture and flow in solids. Philosophical Transactions of the Royal Society of London. Series A, Containing Papers of a Mathematical or Physical Character 221, 163—198.

Haimson, B., Fairhurst, C., 1967. Initiation and Extension of Hydraulic Fractures in Rocks. Society of Petroleum Engineers Journal 7, 310–318.

Hillerborg, A., Modeer, M., Petersson, P.E., 1976. Analysis of crack formation and crack growth in concrete by means of fracture mechanics and finite elements. Cement and Concrete Research 6, 773–782.

Hills, D., Kelly, P., Dai, D., Korsunsky, A., 1996. Solution of Crack Problems: The Distributed Dislocation Technique. 1 ed., Springer, Dordrecht.

Hirshikesh, Martínez-Pañeda, E., Natarajan, S., 2021. Adaptive phase field modelling of crack propagation in orthotropic functionally graded materials. Defence Technology 17, 185–195.

Hou, C., Jin, X., Fan, X., Xu, R., Wang, Z., 2019. A generalized maximum energy release rate criterion for mixed mode fracture analysis of brittle and quasi-brittle materials. Theoretical and Applied Fracture Mechanics 100, 78–85.

Hubbert, M.K., Willis, D.G., 1957. Mechanics of Hydraulic Fracturing. Transactions of the AIME 210, 153–168.

Hussain, Pu, S.L., Underwood, J.H., 1974. Strain energy release rate for a crack under combined mode i and mode ii.

Ingraffea, A.R., Heuze, F.E., 1980. Finite element models for rock fracture mechanics. International Journal for Numerical and Analytical Methods in Geomechanics 4, 25–43.

Ito, T., 2008. Effect of pore pressure gradient on fracture initiation in fluid saturated porous media: Rock. Engineering Fracture Mechanics 75, 1753–1762.

Ito, T., Hayashi, K., 1991. Physical background to the breakdown pressure in hydraulic fracturing tectonic stress measurements. International Journal of Rock Mechanics and Mining Sciences and 28, 285–293. doi:`10.1016/0148-9062(91)90595-D`.

Jaeger, J., Cook, G., Zimmerman, R., 2007. Fundamentals of Rock Mechanics. 4th ed., Blackwell Publishing, Oxford.

Jernkvist, L.O., 2001. Fracture of wood under mixed model loading I. Derivation of fracture criteria. Engineering Fracture Mechanics 68, 549–563.

Jirasek, M., Zimmermann, T., 1998. ANALYSIS OF ROTATING CRACK MODEL. Journal of Engineering Mechanics 124, 842–851.

Jolfaei, S., Lakirouhani, A., 2023. Initiation Pressure and Location of Fracture Initiation in Elliptical Wellbores. Geotechnical and Geological Engineering .

Judt, P.O., Ricoeur, A., Linek, G., 2015. Crack path prediction in rolled aluminum plates with fracture toughness orthotropy and experimental validation. Engineering Fracture Mechanics 138, 33–48.

Judt, P.O., Zarges, J.C., Feldmann, M., Ricoeur, A., Heim, H.P., 2019. Deflecting mode-I cracks in anisotropic materials. Mechanics of Materials 136, 103060.

Ke, C.C., Chen, C.S., Ku, C.Y., Chen, C.H., 2009. Modeling crack propagation path of anisotropic rocks using boundary element method. International Journal for Numerical and Analytical Methods in Geomechanics 33, 1227–1253.

Kiener, D., Han, S.M., 2022. 100 years after Griffith: From brittle bulk fracture to failure in 2D materials. MRS Bulletin 47, 792–799.

Krietsch, H., S. Gischig, V., Doetsch, J., F. Evans, K., Villiger, L., Jalali, M., Valley, B., Löw, S., Amann, F., 2020a. Hydromechanical processes and their influence on the stimulation effected volume: Observations from a decameter-scale hydraulic stimulation project. Solid Earth 11, 1699–1729.

Krietsch, H., Villiger, L., Doetsch, J., Gischig, V., Evans, K.F., Brixel, B., Jalali, M.R., Loew, S., Giardini, D., Amann, F., 2020b. Changing Flow Paths Caused by Simultaneous Shearing and Fracturing Observed During Hydraulic Stimulation. Geophysical Research Letters 47, 1–10.

Kristensen, P.K., Niordson, C.F., Martínez-Pañeda, E., 2021. An assessment of phase field fracture: crack initiation and growth. Philosophical Transactions of the Royal Society A 379, 20210021.

Kuhn, C., Schlüter, A., Müller, R., 2015. On degradation functions in phase field fracture models. Computational Materials Science 108, 374–384.

Kumar, D., Ghassemi, A., 2016. 3D poroelastic simulation and analysis of multiple fracture propagation and refracturing of closely-spaced horizontal wells, in: 50th US Rock Mechanics / Geomechanics Symposium 2016, pp. 1997–2008.

Lecampion, B., 2012. Modeling size effects associated with tensile fracture initiation from a wellbore. International Journal of Rock Mechanics and Mining Sciences 56, 67–76.

Lecampion, B., Bunger, A., Zhang, X., 2018. Numerical methods for hydraulic fracture propagation: A review of recent trends. Journal of Natural Gas Science and Engineering 49, 66–83.

Leguillon, D., 2002. Strength or toughness? A criterion for crack onset at a notch. European Journal of Mechanics, A/Solids 21, 61–72.

Lekhnitskii, S.G., 1968. Anisotropic plates. 2 ed., Gordon and Breach.

Li, H., Wang, W., Cao, Y., Liu, S., 2021. Phase-Field Modeling Fracture in Anisotropic Materials. Advances in Civil Engineering 2021.

Li, X.F., Xu, L.R., 2007. T-stresses across static crack kinking. Journal of Applied Mechanics 74, 181–190.

Li, Y., Jia, D., 2018. Fracture Initiation Model of Shale Fracturing Based on Effective Stress Theory of Porous Media. Geofluids 2018.

Li, Y., Jia, D., Liu, J., Fu, C., Ai, C., 2016. The calculation method based on the equivalent continuum for the fracture initiation pressure of fracturing of coalbed methane well. Journal of Petroleum Science and Engineering 146, 909–920.

Li, Y., Liu, G., Li, J., Yu, L., Zhang, T., Lu, J., 2015. Improving fracture initiation predictions of a horizontal wellbore in laminated anisotropy shales. Journal of Natural Gas Science and Engineering 24, 390–399.

Li, Y., Weijermars, R., 2019. Wellbore stability analysis in transverse isotropic shales with anisotropic failure criteria. Journal of Petroleum Science and Engineering 176, 982–993.

Lim, W.K., Choi, S.Y., Sankar, B.V., 2001. Biaxial load effects on crack extension in anisotropic solids. Engineering Fracture Mechanics 68, 403–416.

Liu, H., Lan, Z., Wang, S., Xu, J., Zhao, C., 2015. Hydraulic fracture initiation mechanism in the definite plane perforating technology of horizontal well. Petroleum Exploration and Development 42, 869–875.

Liu, Y., Chen, P., Wu, B., Ma, T., Wu, B., Zhang, X., Jeffrey, R.G., 2020. Mechanics of hydraulic-fracture growth from a wellbore intersecting natural fractures. Society of Petroleum Engineers Journal 25, 646–661.

Lorenzis, L.D., Düster, A., 2020. Modeling in Engineering Using Innovative Numerical Methods for Solids and Fluids. Springer Cham, Cham.

Ma, L., Korsunsky, A.M., 2005. On the use of vector J-integral in crack growth criteria for brittle solids. International Journal of Fracture 133, 39–46.

Manafi Farid, H., Fakoor, M., 2019. Mixed mode I/II fracture criterion for arbitrary cracks in orthotropic materials considering T-stress effects. Theoretical and Applied Fracture Mechanics 99, 147–160.

McClure, M.W., Horne, R.N., 2014. An investigation of stimulation mechanisms in Enhanced Geothermal Systems. International Journal of Rock Mechanics and Mining Sciences 72, 242–260.

Mehraban, M.R., Bahrami, B., Ayatollahi, M.R., Nejati, M., 2023. A Non-local XFEM-Based Methodology for Modeling Mixed-mode Fracturing of Anisotropic Rocks. Rock Mechanics and Rock Engineering 56, 895–909.

Moës, N., Belytschko, T., 2002. Extended finite element method for cohesive crack growth. Engineering Fracture Mechanics 69, 813–833.

Mohammadnejad, T., Andrade, J., 2016. Numerical modeling of hydraulic fracture propagation, closure and reopening using XFEM with application to in-situ stress estimation. International Journal for Numerical and Analytical Methods in Geomechanics 40, 2033–2060.

Mohtarami, E., Baghbanan, A., Hashemolhosseini, H., 2017. Prediction of fracture trajectory in anisotropic rocks using modified maximum tangential stress criterion. Computers and Geotechnics 92, 108–120.

Motamedi, D., Mohammadi, S., 2010. Dynamic crack propagation analysis of orthotropic media by the extended finite element method. International Journal of Fracture 161, 21–39.

Moukhtari, F.E., Lecampion, B., Zia, H., 2019. Propagation of a planar hydraulic fracture perpendicular to the isotropy plane of a transversely isotropic material, in: Propagation of a planar hydraulic fracture perpendicular to the isotropy plane of a transversely isotropic material.

Moukhtari, F.E., Lecampion, B., Zia, H., 2020. Planar hydraulic fracture growth perpendicular to the isotropy plane in a transversely isotropic material. Journal of the Mechanics and Physics of Solids 137, 103878.

Nejati, M., 2015. Finite element modelling of frictional contact and stress intensity factors in three-dimensional fractured media using unstructured tetrahedral meshes. Ph.D. thesis. Imperial College London Department.

Nejati, M., Aminzadeh, A., Amann, F., Saar, M.O., Driesner, T., 2020a. Mode I fracture growth in anisotropic rocks: Theory and experiment. International Journal of Solids and Structures 195, 74–90.

Nejati, M., Aminzadeh, A., Driesner, T., Saar, M.O., 2020b. On the directional dependency of Mode I fracture toughness in anisotropic rocks. Theoretical and Applied Fracture Mechanics 107, 102494.

Nejati, M., Aminzadeh, A., Saar, M.O., Driesner, T., 2019a. Modified semi-circular bend test to determine the fracture toughness of anisotropic rocks. Engineering Fracture Mechanics 213, 153–171.

Nejati, M., Bahrami, B., Ayatollahi, M.R., Driesner, T., 2021a. On the anisotropy of shear fracture toughness in rocks. Theoretical and Applied Fracture Mechanics 113, 102946.

Nejati, M., Bahrami, B., Ayatollahi, M.R., Driesner, T., 2021b. On the anisotropy of shear fracture toughness in rocks. Theoretical and Applied Fracture Mechanics 113, 102946.

Nejati, M., Dambly, M.L.T., Saar, M.O., 2019b. A methodology to determine the elastic properties of anisotropic rocks from a single uniaxial compression test. Journal of Rock Mechanics and Geotechnical Engineering 11, 1166–1183.

Nejati, M., Ghouli, S., Ayatollahi, M.R., 2021c. Crack tip asymptotic fields in anisotropic planes: Importance of higher order terms. Applied Mathematical Modelling 91, 837–862.

Nejati, M., Paluszny, A., Zimmerman, R.W., 2015a. A disk-shaped domain integral method for the computation of stress intensity factors using tetrahedral meshes. International Journal of Solids and Structures 69-70, 230–251.

Nejati, M., Paluszny, A., Zimmerman, R.W., 2015b. On the use of quarter-point tetrahedral finite elements in linear elastic fracture mechanics. Engineering Fracture Mechanics 144, 194–221.

Obata, M., Nemat-Nasser, S., Goto, Y., 1989. Branched Cracks in Anisotropic Elastic Solids. Journal of Applied Mechanics 56, 858–864.

Peirce, A., 2015. Modeling multi-scale processes in hydraulic fracture propagation using the implicit level set algorithm. Computer Methods in Applied Mechanics and Engineering 283, 881–908.

Pham, K., Amor, H., Marigo, J.J., Maurini, C., 2011. Gradient Damage Models and Their Use to Approximate Brittle Fracture. International Journal of Damage Mechanics 20, 618–652.

Profit, M.L., Dutko, M., Yu, J., 2015. Developing a framework to simulate the hydraulic fracturing of tight gas reservoirs based on integrative adaptive remeshing and combined finite/discrete element approach.

Randolph, J.B., Saar, M.O., 2011. Coupling carbon dioxide sequestration with geothermal energy capture in naturally permeable, porous geologic formations: Implications for CO2 sequestration. Energy Procedia 4, 2206–2213.

Rezaei, S., Mianroodi, J.R., Brepols, T., Reese, S., 2021. Direction-dependent fracture in solids: Atomistically calibrated phase-field and cohesive zone model. Journal of the Mechanics and Physics of Solids 147, 104253.

Richardson, C.L., Hegemann, J., Sifakis, E., Hellrung, J., Teran, J.M., 2009. An XFEM method for modelling geometrically elaborate crack.pdf. INTERNATIONAL JOURNAL FOR NUMERICAL METHODS IN ENGINEERING Int. .

Romanowicz, M., 2019. A non-local stress fracture criterion accounting for the anisotropy of the fracture toughness. Engineering Fracture Mechanics 214, 544–557.

Romanowicz, M., Seweryn, A., 2008. Verification of a non-local stress criterion for mixed mode fracture in wood. Engineering Fracture Mechanics 75, 3141–3160.

Sadd, M., 2014. Elasticity: Theory, Applications, and Numerics. 3 ed., Academic Press.

Sakha, M., Nejati, M., Aminzadeh, A., Ghouli, S., Saar, M.O., Driesner, T., 2022. On the validation of mixed-mode I/II crack growth theories for anisotropic rocks. International Journal of Solids and Structures 241, 111484.

Sakha, M., Nejati, M., De Lorenzis, L., Driesner, T., 2023. Modeling hydraulic fracture initiation of a notch-free wellbore in anisotropic rocks, in: 15th International Conference on Fracture (ICF15), Atlanta, GA USA.

Saouma, V.E., Ayari, M.L., Leavell, D.A., 1987. Mixed mode crack propagation in homogeneous anisotropic solids. Engineering Fracture Mechanics 27, 171–184.

Sapora, A., Cornetti, P., Carpinteri, A., Firrao, D., 2015. An improved Finite Fracture Mechanics approach to blunt V-notch brittle fracture mechanics: Experimental verification on ceramic, metallic, and plastic materials. Theoretical and Applied Fracture Mechanics 78, 20–24.

Sapora, A., Spagnoli, A., Susmel, L., Cornetti, P., 2023. A simplified approach to hydraulic fracturing of rocks based on Finite Fracture Mechanics. Fatigue and Fracture of Engineering Materials and Structures , 3029–3042.

Savin, G.N., 1961. Stress concentration around holes. Oxford : Pergamon Press.

Schmidt, R.A., 1980. A MICROCRACK MODEL AND ITS SIGNIFICANCE TO HYDRAULIC FRACTURING AND FRACTURE TOUGHNESS TESTING, in: Proc 21st US symp on rock mech, pp. 581–590.

Serajian, V., Ghassemi, A., 2011. Hydraulic fracture initiation from a wellbore in transversely isotropic rock.

Sesetty, V., Ghassemi, A., 2018. Effect of rock anisotropy on wellbore stresses and hydraulic fracture propagation. International Journal of Rock Mechanics and Mining Sciences 112, 369–384.

Shah, P.D., Tan, C.L., Wang, X., 2006. T-stress solutions for two-dimensional crack problems in anisotropic elasticity using the boundary element method. Fatigue and Fracture of Engineering Materials and Structures 29, 343–356.

Shen, B., Shi, J., 2016. Fracturing-hydraulic coupling in transversely isotropic rocks and a case study on CO2 sequestration. International Journal of Rock Mechanics and Mining Sciences 88, 206–220.

Shen, B., Stephansson, O., 1994. Modification of the G-criterion for crack propagation subjected to compression. Engineering Fracture Mechanics 47, 177–189.

Shen, B., Stephansson, O., Rinne, M., 2014. Modelling Rock Fracturing Processes: A Fracture Mechanics Approach Using FRACOD. 1 ed., Springer Netherlands.

Shi, F., Wang, X., Liu, C., Liu, H., Wu, H., 2017. An XFEM-based method with reduction technique for modeling hydraulic fracture propagation in formations containing frictional natural fractures. Engineering Fracture Mechanics 173, 64–90.

Siebrits, E., Peirce, A.P., 2002. A efficient multi-layer planar 3D fracture growth algorithm using a fixed mesh approach. International Journal for Numerical Methods in Engineering 53, 691–717.

Sih, G.C., 1973. Energy-density concept in fracture mechanics. Engineering Fracture Mechanics 5, 1037–1040.

Sih, G.C., 1974. Strain-energy-density factor applied to mixed mode crack problems. International Journal of Fracture 10, 305–321.

Sih, G.C., Paris, P.C., Irwin, G.R., 1965. On cracks in rectilinearly anisotropic bodies. International Journal of Fracture Mechanics , 189–203.

Smith, D.J., Ayatollahi, M.R., Pavier, M.J., 2001. The role of T-stress in brittle fracture for linear elastic materials under mixed-mode loading. Fatigue and Fracture of Engineering Materials and Structures 24, 137–150.

Stober, I., Bucher, K., 2021. Enhanced-Geothermal-Systems (EGS), Hot-Dry-Rock Systems (HDR), Deep-Heat-Mining (DHM). Springer International Publishing, Cham.

Tan, Y., Yang, D., Sheng, Y., 2009. Discrete element method (DEM) modeling of fracture and damage in the machining process of polycrystalline SiC. Journal of the European Ceramic Society 29, 1029–1037.

Thongprapha, T., Tengpakwaen, K., Daemen, J.J., Fuenkajorn, K., 2022. Effect of confining pressures on transverse isotropy of Maha Sarakham salt. International Journal of Rock Mechanics and Mining Sciences 152, 105077.

Ting, T., 1996. Anisotropic Elasticity: Theory and Applications. Oxford University Press.

Torabi, A.R., Etesam, S., Sapora, A., Cornetti, P., 2017. Size effects on brittle fracture of Brazilian disk samples containing a circular hole. Engineering Fracture Mechanics 186, 496–503.

Valliappan, V., Remmers, J.J., Barnhoorn, A., Smeulders, D.M., 2019. A Numerical Study on the Effect of Anisotropy on Hydraulic Fractures. Rock Mechanics and Rock Engineering 52, 591–609.

Wang, H., Li, Y., Cao, S., Fantuzzi, N., Pan, R., Tian, M., Liu, Y., Yang, H., 2020. Fracture toughness analysis of HCCD specimens of Longmaxi shale subjected to mixed mode I-II loading. Engineering Fracture Mechanics 239.

Wheeler, M.F., Wick, T., Wollner, W., 2014. An augmented-Lagrangian method for the phase-field approach for pressurized fractures. Computer Methods in Applied Mechanics and Engineering 271, 69–85.

Williams, J.G., Ewing, P.D., 1984. Fracture under complex stress - The angled crack problem. International Journal of Fracture 26, 346–351.

Wong, L.N., Einstein, H.H., 2009. Systematic evaluation of cracking behavior in specimens containing single flaws under uniaxial compression. International Journal of Rock Mechanics and Mining Sciences 46, 239–249.

Wu, J.Y., Nguyen, V.P., Nguyen, C.T., Sutula, D., Sinaie, S., Bordas, S.P., 2020a. Phase-field modeling of fracture. Advances in Applied Mechanics 53, 1–183.

Wu, J.Y., Nguyen, V.P., Zhou, H., Huang, Y., 2020b. A variationally consistent phase-field anisotropic damage model for fracture. Computer Methods in Applied Mechanics and Engineering 358, 112629.

Wu, K.C., 1992. Interaction of a dislocation with an elliptic hole or rigid inclusion in an anisotropic material. Journal of Applied Physics 72, 2156–2163.

Xi, X., Yang, S., Shipton, Z., Cai, M., 2022. Modelling the near-wellbore rock fracture tortuosity: Role of casing-cement-rock well system, perforation and in-situ stress. International Journal of Rock Mechanics and Mining Sciences 157, 105182.

Yang, S., Yuan, F.G., 2000. Kinked crack in anisotropic bodies. International Journal of Solids and Structures 37, 6635–6682.

Ye, Z., Ayari, M.L., 1994. Prediction of crack propagation in anisotropic solids. Engineering Fracture Mechanics 49, 797–808.

Yoon, J.S., Zang, A., Stephansson, O., 2014. Numerical investigation on optimized stimulation of intact and naturally fractured deep geothermal reservoirs using hydro-mechanical coupled discrete particles joints model. Geothermics 52, 165–184.

Yoon, J.S., Zimmermann, G., Zang, A., 2015a. Numerical Investigation on Stress Shadowing in Fluid Injection-Induced Fracture Propagation in Naturally Fractured Geothermal Reservoirs. Rock Mechanics and Rock Engineering 48, 1439–1454.

Yoon, J.S., Zimmermann, G., Zang, A., Stephansson, O., 2015b. Discrete element modeling of fluid injection–induced seismicity and activation of nearby fault. Canadian Geotechnical Journal 52, 1457–1465.

Zeng, Q., Liu, W., Yao, J., 2018. Numerical modeling of multiple fractures propagation in anisotropic formation. Journal of Natural Gas Science and Engineering 53, 337–346.

Zhang, S.Q., Jang, B.Z., Valaire, B.T., Suhling, J.C., 1989. A new criterion for composite material mixed mode fracture analysis. Engineering Fracture Mechanics 34, 749–769.

Zhang, X., Jeffrey, R.G., Bunger, A.P., Thiercelin, M., 2011. Initiation and growth of a hydraulic fracture from a circular wellbore. International Journal of Rock Mechanics and Mining Sciences 48, 984–995.

Zhang, X., Lu, Y., Tang, J., Zhou, Z., Liao, Y., 2017a. Experimental study on fracture initiation and propagation in shale using supercritical carbon dioxide fracturing. Fuel 190, 370–378.

Zhang, X., Sloan, S.W., Vignes, C., Sheng, D., 2017b. A modification of the phase-field model for mixed mode crack propagation in rock-like materials. Computer Methods in Applied Mechanics and Engineering 322, 123–136.

Zhao, X., Paul Young, R., 2011. Numerical modeling of seismicity induced by fluid injection in naturally fractured reservoirs. Geophysics 76, 169–182.

Zhi Kai Guo, Kobayashi, A.S., Hawkins, N.M., 1993. Further studies on fracture process zone for mode I concrete fracture. Engineering Fracture Mechanics 46, 1041–1049.

Zhou, Z.L., Yang, D.S., Chen, W.Z., Zhang, X., Wu, B.L., Zhang, F.S., 2021. Numerical study of initiation pressure in hydraulic fracturing by dual criterion for non-circular wellbore. Engineering Fracture Mechanics 252, 107804.

Zhu, H., Deng, J., Jin, X., Hu, L., Luo, B., 2015. Hydraulic Fracture Initiation and Propagation from Wellbore with Oriented Perforation. Rock Mechanics and Rock Engineering 48, 585–601.

Zhuang, X., Zhou, S., Huynh, G.D., Areias, P., Rabczuk, T., 2022. Phase field modeling and computer implementation: A review. Engineering Fracture Mechanics 262, 108234.

Zi, G., Belytschko, T., 2003. New crack-tip elements for XFEM and applications to cohesive cracks. International Journal for Numerical Methods in Engineering 57, 2221–2240.

Ziaei-rad, V., Mollaali, M., Nagel, T., Kolditz, O., Yoshioka, K., 2023. Orthogonal decomposition of anisotropic constitutive models for the phase field approach to fracture. Journal of the Mechanics and Physics of Solids 171, 105143.

Appendix A

ELASTICITY PROBLEM: KINKED CRACK IN ANISOTROPIC SOLIDS

A.1 Theoretical background on anisotropic elasticity

Let us consider the coordinate system $\mathrm{x'y'}$ in such a way that the axis $\mathrm{x'}$ (principal direction 1) lies within the isotropy plane of a transversely isotropic material, while $\mathrm{y'}$ (principal direction 2) is oriented normal to the isotropy plane (see Figure A.1.1a). As shown in Figure A.1.1, the global coordinate system xy results from rotating the coordinate system $\mathrm{x'y'}$ along the axis $\mathrm{z'}$ by $-\beta$. By applying the transformation rules, the strain and stress tensors can be generally represented in the global coordinate xy and thus, Hooke's law can be rewritten as [Nejati et al., 2020a]

$$\begin{pmatrix} \epsilon_{\mathrm{x}} \\ \epsilon_{\mathrm{y}} \\ \gamma_{\mathrm{xy}} \end{pmatrix} = \frac{1}{E} \begin{pmatrix} \tilde{S}_{11} & \tilde{S}_{12} & \tilde{S}_{16} \\ \tilde{S}_{12} & \tilde{S}_{22} & \tilde{S}_{26} \\ \tilde{S}_{16} & \tilde{S}_{26} & \tilde{S}_{66} \end{pmatrix} \begin{pmatrix} \sigma_{\mathrm{x}} \\ \sigma_{\mathrm{y}} \\ \tau_{\mathrm{xy}} \end{pmatrix}, \tag{A.1.1}$$

where the components $\tilde{S}_{\mathrm{ij}}$ are given by Nejati et al. [2020a].

According to Lekhnitskii's formulation, the problem of two-dimensional anisotropic elasticity can be represented by a fourth order partial differential equation in terms of the *Airy* stress function [Lekhnitskii, 1968]. The general solution of this equation depends on the complex roots derived by solving the following characteristic equation:

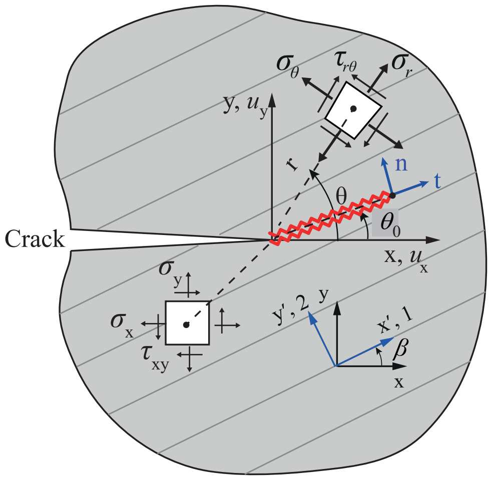

Figure A.1.1: An anisotropic plane with two local coordinate systems x′y′ and nt which coincide with the principal material directions and the direction of fracture growth, respectively. The global coordinate system xy makes the angle $-\beta$ with respect to x′y′.

$$\tilde{S}_{11}\mu^4 - 2\tilde{S}_{16}\mu^3 + (2\tilde{S}_{12} + \tilde{S}_{66})\mu^2 - 2\tilde{S}_{26}\mu + \tilde{S}_{22} = 0 \; . \tag{A.1.2}$$

The roots of this characteristic equation are complex, and always occur in conjugate pairs: $\mu_1 = a_1 + ib_1$, $\mu_2 = a_2 + ib_2$, $\mu_3 = \bar{\mu}_1$, $\mu_4 = \bar{\mu}_2$ [Lekhnitskii, 1968]. The simplest form of the characteristic equation is obtained in the material coordinate system x′y′, given as

$$\mu'^4 + \left(\frac{1+\xi}{\kappa_1\eta} + 2\xi\nu'\frac{(1-\kappa_3\eta)}{\kappa_1\eta}\right)\mu'^2 + \frac{\kappa_2}{\kappa_1}\xi = 0 \; . \tag{A.1.3}$$

Here, $\kappa_1 = \kappa_2 = \kappa_3 = 1$ for the plane-stress condition and $\kappa_1 = 1-\nu^2$, $\kappa_2 = 1-\xi\nu'^2$, $\kappa_3 = 1+\nu$ for the plane-strain condition. The dimensionless parameters ξ and η are defined as

$$\xi = \frac{E}{E'}, \qquad \eta = \frac{G'}{G'_{\mathrm{sv}}}, \tag{A.1.4}$$

where G'_{sv} is the transverse shear modulus approximated from the Saint-Venant relation: $1/G'_{\mathrm{sv}} = 1/E + (1+2\nu')/E'$. The reasons for employing ξ, η to formulate elasticity equations are given in detail in Nejati et al. [2019b, 2020b].

The complex roots of Eq. A.1.3, μ'_1 and μ'_2, are practically functions of only ξ and η for the plane-stress condition. This is because the influence of ν' on the roots of Eq. A.1.3 is negligible [Nejati et al., 2019a]. However, for the plane-strain case, μ'_1 and μ'_2 depend also on the parameters κ_1, κ_2 and κ_3. Once the complex parameters μ'_1 and μ'_2 are evaluated from Eq. A.1.3, the transformed complex parameters in the coordinate system xy are readily computed from [Lekhnitskii, 1968]

$$\mu_{\mathrm{k}} = \frac{\mu'_{\mathrm{k}}\cos\beta + \sin\beta}{\cos\beta - \mu'_{\mathrm{k}}\sin\beta}\,, \qquad \mathrm{k} = 1, 2. \tag{A.1.5}$$

Let us now present the stress, strain, and displacement fields in the vicinity of the crack tip. Assume that a crack is oriented along x-axis. Sih et al. [1965] first derived the crack tip fields in an anisotropic plane, and presented the fields using only the singular terms. Recently, the fields corresponding to the higher order terms have also been derived [Ghouli et al., 2020; Nejati et al., 2021c]. We consider only the first two terms of the crack tip asymptotic field, formulating the polar stress fields near to the crack tip under mixed-mode I/II loading as

$$\begin{aligned}
&\begin{pmatrix}\sigma_{\mathrm{r}}\\ \sigma_\theta\\ \tau_{\mathrm{r}\theta}\end{pmatrix} = \frac{K_{\mathrm{eff}}}{\sqrt{2\pi r}}\left[\begin{pmatrix}\tilde{\sigma}_{\mathrm{r}}(\mu_{\mathrm{k}},\theta,\lambda)\\ \tilde{\sigma}_\theta(\mu_{\mathrm{k}},\theta,\lambda)\\ \tilde{\tau}_{\mathrm{r}\theta}(\mu_{\mathrm{k}},\theta,\lambda)\end{pmatrix} + \frac{T\sqrt{2\pi r}}{K_{\mathrm{eff}}}\begin{pmatrix}\cos^2\theta\\ \sin^2\theta\\ -\sin\theta\cos\theta\end{pmatrix}\right]\,,\\
&\tilde{\sigma}_{\mathrm{r}} = \Re\left[\frac{1}{(\mu_1-\mu_2)}\left\{\frac{\left(\lambda \pm \mu_1\sqrt{1-\lambda^2}\right)(\sin\theta-\mu_2\cos\theta)^{\,2}}{\sqrt{\cos\theta+\mu_2\sin\theta}} - \frac{\left(\lambda \pm \mu_2\sqrt{1-\lambda^2}\right)(\sin\theta-\mu_1\cos\theta)^{\,2}}{\sqrt{\cos\theta+\mu_1\sin\theta}}\right\}\right]\,,\\
&\tilde{\sigma}_\theta = \Re\left[\frac{1}{(\mu_1-\mu_2)}\left\{\left(\lambda \pm \mu_1\sqrt{1-\lambda^2}\right)(\cos\theta+\mu_2\sin\theta)^{\,3/2} - \left(\lambda \pm \mu_2\sqrt{1-\lambda^2}\right)(\cos\theta+\mu_1\sin\theta)^{\,3/2}\right\}\right]\,,\\
&\tilde{\tau}_{\mathrm{r}\theta} = \Re\left[\frac{1}{(\mu_1-\mu_2)}\left\{\left(\lambda \pm \mu_1\sqrt{1-\lambda^2}\right)(\sin\theta-\mu_2\cos\theta)\sqrt{\cos\theta+\mu_2\sin\theta}\right.\right.\\
&\left.\left.\quad - \left(\lambda \pm \mu_2\sqrt{1-\lambda^2}\right)(\sin\theta-\mu_1\cos\theta)\sqrt{\cos\theta+\mu_1\sin\theta}\right\}\right]\,.
\end{aligned} \tag{A.1.6}$$

In Eq. A.1.6, T is a constant stress acting parallel to the crack, known as the T-stress, and r and θ are the polar coordinates. The mode-mixity parameter λ is defined as the ratio of mode II stress intensity factor to the effective stress intensity factor, K_{eff}, which yields

$$\lambda = \frac{K_{\text{II}}}{K_{\text{eff}}}, \quad K_{\text{eff}} = \sqrt{K_{\text{I}}^2 + K_{\text{II}}^2}. \tag{A.1.7}$$

where K_{I} and K_{II} are modes I and II stress intensity factors. $\lambda = 0$ and $\lambda = \pm 1$ denote pure modes I and II loadings, respectively, while $-1 < \lambda < 1$ represents a range of mixed-mode loadings with different contributions of each mode. The ± sign in Eq. (A.1.6) represents the sign of mode I stress intensity factor. Since $K_{\text{I}} > 0$ in this study, the positive sign is used in the formulations of this paper. which is assumed to be positive in this study. The effective stress intensity factor also indicates the intensity of the stresses in the mixed-mode I/II loading near the crack tip. Note that the complex parameters μ_1, μ_2 must be obtained in the crack tip coordinate system xy. The strain and displacement fields in the Cartesian coordinate are also given by [Nejati et al., 2020a, 2021c]

$$\begin{aligned}
\begin{pmatrix} \epsilon_{\text{x}} \\ \epsilon_{\text{y}} \\ \gamma_{\text{xy}} \end{pmatrix} &= \frac{K_{\text{eff}}}{E\sqrt{2\pi r}} \left[\begin{pmatrix} \tilde{\epsilon}_{\text{x}}(p_{\text{k}}, \mu_{\text{k}}, \theta, \lambda) \\ \tilde{\epsilon}_{\text{y}}(q_{\text{k}}, \mu_{\text{k}}, \theta, \lambda) \\ \tilde{\gamma}_{\text{xy}}(d_{\text{k}}, \mu_{\text{k}}, \theta, \lambda) \end{pmatrix} + \frac{T\sqrt{2\pi r}}{K_{\text{eff}}} \begin{pmatrix} \tilde{S}_{11} \\ \tilde{S}_{12} \\ \tilde{S}_{16} \end{pmatrix} \right], \\
\tilde{\epsilon}_{\text{x}} &= \Re \left[\frac{1}{(\mu_1 - \mu_2)} \left\{ \frac{p_2 \left(\lambda \pm \mu_1 \sqrt{1-\lambda^2}\right)}{\sqrt{\cos\theta + \mu_2 \sin\theta}} - \frac{p_1 \left(\lambda \pm \mu_2 \sqrt{1-\lambda^2}\right)}{\sqrt{\cos\theta + \mu_1 \sin\theta}} \right\} \right], \\
\tilde{\epsilon}_{\text{y}} &= \Re \left[\frac{1}{(\mu_1 - \mu_2)} \left\{ \frac{\mu_2 q_2 \left(\lambda \pm \mu_1 \sqrt{1-\lambda^2}\right)}{\sqrt{\cos\theta + \mu_2 \sin\theta}} - \frac{\mu_1 q_1 \left(\lambda \pm \mu_2 \sqrt{1-\lambda^2}\right)}{\sqrt{\cos\theta + \mu_1 \sin\theta}} \right\} \right], \\
\tilde{\gamma}_{\text{xy}} &= \Re \left[\frac{1}{(\mu_1 - \mu_2)} \left\{ \frac{d_2 \left(\lambda \pm \mu_1 \sqrt{1-\lambda^2}\right)}{\sqrt{\cos\theta + \mu_2 \sin\theta}} - \frac{d_1 \left(\lambda \pm \mu_2 \sqrt{1-\lambda^2}\right)}{\sqrt{\cos\theta + \mu_1 \sin\theta}} \right\} \right],
\end{aligned} \tag{A.1.8}$$

and

$$\begin{pmatrix} u_{\mathrm{x}} \\ u_{\mathrm{y}} \end{pmatrix} = \frac{K_{\mathrm{eff}}}{E}\sqrt{\frac{2r}{\pi}}\left[\begin{pmatrix} \tilde{u}_{\mathrm{x}}(p_{\mathrm{k}},\mu_{\mathrm{k}},\theta,\lambda) \\ \tilde{u}_{\mathrm{y}}(q_{\mathrm{k}},\mu_{\mathrm{k}},\theta,\lambda) \end{pmatrix} + \frac{\sqrt{\frac{\pi r}{2}}T}{K_{\mathrm{eff}}}\begin{pmatrix} \tilde{S}_{11}(\cos\theta + \Re(\mu_1+\mu_2)\sin\theta) \\ \tilde{S}_{12}\sin\theta \end{pmatrix}\right] ,$$

$$\tilde{u}_{\mathrm{x}} = \Re\left[\frac{p_2\left(\pm\mu_1\sqrt{1-\lambda^2}+\lambda\right)\sqrt{\mu_2\sin\theta+\cos\theta} - p_1\left(\pm\mu_2\sqrt{1-\lambda^2}+\lambda\right)\sqrt{\mu_1\sin\theta+\cos\theta}}{E\left(\mu_1-\mu_2\right)}\right] ,$$

$$\tilde{u}_{\mathrm{y}} = \Re\left[\frac{q_2\left(\pm\mu_1\sqrt{1-\lambda^2}+\lambda\right)\sqrt{\mu_2\sin\theta+\cos\theta} - q_1\left(\pm\mu_2\sqrt{1-\lambda^2}+\lambda\right)\sqrt{\mu_1\sin\theta+\cos\theta}}{E\left(\mu_1-\mu_2\right)}\right] ,$$

(A.1.9)

where

$$\begin{aligned} p_{\mathrm{k}} &= \tilde{S}_{11}\mu_{\mathrm{k}}^2 + \tilde{S}_{12} - \tilde{S}_{16}\mu_{\mathrm{k}} \ , \\ q_{\mathrm{k}} &= \tilde{S}_{12}\mu_{\mathrm{k}} + \tilde{S}_{22}/\mu_{\mathrm{k}} - \tilde{S}_{26} \ , \quad (\mathrm{k}=1,2) \\ d_{\mathrm{k}} &= \tilde{S}_{16}\mu_{\mathrm{k}}^2 + \tilde{S}_{26} - \tilde{S}_{66}\mu_{\mathrm{k}} \ . \end{aligned} \qquad \text{(A.1.10)}$$

One can transform Eq. (A.1.8) to obtain the strain field in the polar coordinate system as

$$
\begin{aligned}
&\begin{pmatrix} \epsilon_{\mathrm{r}} \\ \epsilon_{\theta} \\ \gamma_{\mathrm{r}\theta} \end{pmatrix} = \frac{K_{\mathrm{eff}}}{E\sqrt{2\pi r}} \left[\begin{pmatrix} \tilde{\epsilon}_{\mathrm{r}}(\tilde{S}_{ij}, \mu_{\mathrm{k}}, \theta, \lambda) \\ \tilde{\epsilon}_{\theta}(\tilde{S}_{ij}, \mu_{\mathrm{k}}, \theta, \lambda) \\ \tilde{\gamma}_{\mathrm{r}\theta}(\tilde{S}_{ij}, \mu_{\mathrm{k}}, \theta, \lambda) \end{pmatrix} + \frac{T\sqrt{2\pi r}}{K_{\mathrm{eff}}} \begin{pmatrix} \tilde{S}_{\mathrm{r}} \\ \tilde{S}_{\theta} \\ \tilde{S}_{\mathrm{r}\theta} \end{pmatrix} \right] , \\
&\tilde{\epsilon}_{\mathrm{r}} = \Re \left[\frac{1}{(\mu_1 - \mu_2)} \left\{ \frac{\left(\lambda \pm \mu_1\sqrt{1-\lambda^2}\right)}{\sqrt{\cos\theta + \mu_2 \sin\theta}} \left(p_2 \cos^2\theta + \mu_2 q_2 \sin^2\theta + d_2 \sin\theta\cos\theta\right) - \right. \right. \\
&\left. \left. \frac{\left(\lambda \pm \mu_2\sqrt{1-\lambda^2}\right)}{\sqrt{\cos\theta + \mu_1 \sin\theta}} \left(p_1 \cos^2\theta + \mu_1 q_1 \sin^2\theta + d_1 \sin\theta\cos\theta\right) \right\} \right] , \\
&\tilde{\epsilon}_{\theta} = \Re \left[\frac{1}{(\mu_1 - \mu_2)} \left\{ \frac{\left(\lambda \pm \mu_1\sqrt{1-\lambda^2}\right)}{\sqrt{\cos\theta + \mu_2 \sin\theta}} \left(p_2 \sin^2\theta + \mu_2 q_2 \cos^2\theta - d_2 \sin\theta\cos\theta\right) - \right. \right. \\
&\left. \left. \frac{\left(\lambda \pm \mu_2\sqrt{1-\lambda^2}\right)}{\sqrt{\cos\theta + \mu_1 \sin\theta}} \left(p_1 \sin^2\theta + \mu_1 q_1 \cos^2\theta - d_1 \sin\theta\cos\theta\right) \right\} \right] , \\
&\tilde{\gamma}_{\mathrm{r}\theta} = \Re \left[\frac{1}{(\mu_1 - \mu_2)} \left\{ \left(- \frac{(p_2 - \mu_2 q_2)\left(\lambda \pm \mu_1\sqrt{1-\lambda^2}\right)}{\sqrt{\cos\theta + \mu_2 \sin\theta}} + \frac{(p_1 - \mu_1 q_1)\left(\lambda \pm \mu_2\sqrt{1-\lambda^2}\right)}{\sqrt{\cos\theta + \mu_1 \sin\theta}} \right) \sin 2\theta \right. \right. \\
&\left. \left. + \left(\frac{d_2\left(\lambda \pm \mu_1\sqrt{1-\lambda^2}\right)}{\sqrt{\cos\theta + \mu_2 \sin\theta}} - \frac{d_1\left(\lambda \pm \mu_2\sqrt{1-\lambda^2}\right)}{\sqrt{\cos\theta + \mu_1 \sin\theta}} \right) \cos 2\theta \right\} \right] ,
\end{aligned}
\tag{A.1.11}
$$

where

$$
\begin{aligned}
\tilde{S}_{\mathrm{r}} &= \tilde{S}_{11}\cos^2\theta + \tilde{S}_{12}\sin^2\theta + \tilde{S}_{16}\sin\theta\cos\theta, \\
\tilde{S}_{\theta} &= \tilde{S}_{11}\sin^2\theta + \tilde{S}_{12}\cos^2\theta - \tilde{S}_{16}\sin\theta\cos\theta, \\
\tilde{S}_{\mathrm{r}\theta} &= (\tilde{S}_{12} - \tilde{S}_{11})\sin 2\theta + \tilde{S}_{16}\cos 2\theta.
\end{aligned}
\tag{A.1.12}
$$

A.2 Energy release rate (ERR) function

This section gives the details of the derivation of the energy release rate due to the development of a kink at the tip of the main crack in an anisotropic plane. An exact solution is derived from the dislocation theory, while a simpler approximate solution is obtained assuming an infinitesimal kink and the stress field near the main crack. In the approximate solution, the assumption of an infinitesimally small kink allows us to derive a closed-form approximation for the stress intensity factors at the kinked crack tip. Contrary to the approximate solution, the dislocation technique is applicable to the problems in which the kink segment is large, provided that the higher order terms in the stress series expansion are included. Both methods are explained next.

A.2.1 Dislocation technique

The dislocation technique provides an exact formulation for the energy release rate function $\mathcal{G}(\theta)$ in anisotropic materials. This technique is basically formulated based on the Stroh formalism and singular integral equation approach [Yang and Yuan, 2000]. Implementation of the dislocation technique yields a system of integral equations governing the kinked crack problem. According to Traction-free condition, this system is constructed by the superposition of two solutions: a solution for a line dislocation in an infinite plane without a crack, and a solution in the presence of a crack. The latter solution is subjected to the opposite traction deduced by the line dislocation. The full details are given in Yang and Yuan [2000]. The sum of the two solutions leads to the following integral equation:

$$\int_{-1}^{1}\left(\frac{\boldsymbol{I}}{\gamma-\chi}+\frac{1}{2}\frac{\boldsymbol{I}}{1+\chi+\sqrt{(1+\chi)(1+\gamma)}}+\frac{1}{2}\sum_{\alpha=1}^{2}\Re\left[\boldsymbol{B}\left\langle\frac{1}{1+\chi+\sqrt{(1+\chi)(1+\gamma)\frac{\bar{z}_\alpha}{z}}}\right\rangle\boldsymbol{Y}_\alpha\right]\right)\frac{\mathbf{q}(\gamma)\mathrm{d}\gamma}{(1+\gamma)^{s}(1-\gamma)^{1/2}}=$$
$$\frac{1}{\sqrt{\pi(1+\chi)}}\Re\left[\boldsymbol{B}\left\langle\sqrt{z}\right\rangle\boldsymbol{B}^{-1}\right]\mathbf{k}-\sqrt{r}\,\mathbf{t}\sin\theta\,,\quad -1\leq\chi\leq 1 \tag{A.2.1}$$

where

$$\langle\sqrt{z}\rangle = diag[\sqrt{\cos\theta+\mu_1\sin\theta}, \sqrt{\cos\theta+\mu_2\sin\theta}], \left\langle \frac{1}{1+\chi+\sqrt{(1+\chi)(1+\gamma)\dfrac{\bar{z}_\alpha}{z}}} \right\rangle =$$
$$diag[\frac{1}{1+\chi+\sqrt{(1+\chi)(1+\gamma)\dfrac{\cos\theta+\bar{\mu}_\alpha\sin\theta}{\cos\theta+\mu_1\sin\theta}}}, \frac{1}{1+\chi+\sqrt{(1+\chi)(1+\gamma)\dfrac{\cos\theta+\bar{\mu}_\alpha\sin\theta}{\cos\theta+\mu_2\sin\theta}}}], \tag{A.2.2}$$

and

$$\begin{aligned} \boldsymbol{B} &= \begin{pmatrix} -\mu_1 & -\mu_2 \\ 1 & 1 \end{pmatrix}, \\ \boldsymbol{Y}_\alpha &= \boldsymbol{B}^{-1}\bar{\boldsymbol{B}}\boldsymbol{I}_\alpha\bar{\boldsymbol{B}}^{-1}, \quad \boldsymbol{I}_{\alpha=1} = diag[1,0], \quad \boldsymbol{I}_{\alpha=2} = diag[0,1]. \end{aligned} \tag{A.2.3}$$

The unknown function $q(\gamma)$ is bounded within $-1 \le \gamma \le 1$, and can be obtained by using Chebychev polynomials when $s = 1/2$ and $\mathbf{q}(-1) = 0$ are assumed. The detail of the numerical techniques for solving integral equations is discussed in Erdogan et al. [1973]. Due to the linearity of the integral equation with respect to the function $\mathbf{q}(\gamma)$, the solution is divided into the sum of the solutions due to k-term and T-term. Thus, the unknown function $\mathbf{q}(\gamma)$ can be expressed by

$$\mathbf{q}(\gamma) = K_{\text{II}}\mathbf{q}_2^{(1)}(\gamma) + K_{\text{I}}\mathbf{q}_1^{(1)}(\gamma) + \sqrt{r}T\mathbf{q}_1^{(2)}(\gamma)\ , \tag{A.2.4}$$

where the superscripts (i), $i = 1, 2$ stand for k-term and T-term, respectively. The principle of superposition allows us to obtain $\mathbf{q}_1^{(1)}$, $\mathbf{q}_2^{(1)}$, and $\mathbf{q}_1^{(2)}$ by solving the following integral equations:

$$\int_{-1}^{1}\left(\frac{\boldsymbol{I}}{\gamma-\chi}+\frac{1}{2}\frac{\boldsymbol{I}}{1+\chi+\sqrt{(1+\chi)(1+\gamma)}}+\frac{1}{2}\sum_{\alpha=1}^{2}\Re\left[\boldsymbol{B}\left\langle\frac{1}{1+\chi+\sqrt{(1+\chi)(1+\gamma)\frac{\bar{z}_{\alpha}}{z}}}\right\rangle\boldsymbol{Y}_{\alpha}\right]\right)\frac{\mathbf{q}_1^{(1)}(\gamma)\mathrm{d}\gamma}{(1+\gamma)^{s}(1-\gamma)^{1/2}}=$$

$$\frac{1}{\sqrt{\pi(1+\chi)}}\Re\left[\boldsymbol{B}\left\langle\sqrt{z}\right\rangle\boldsymbol{B}^{-1}\right]\begin{pmatrix}0\\1\end{pmatrix},$$

$$\int_{-1}^{1}\left(\frac{\boldsymbol{I}}{\gamma-\chi}+\frac{1}{2}\frac{\boldsymbol{I}}{1+\chi+\sqrt{(1+\chi)(1+\gamma)}}+\frac{1}{2}\sum_{\alpha=1}^{2}\Re\left[\boldsymbol{B}\left\langle\frac{1}{1+\chi+\sqrt{(1+\chi)(1+\gamma)\frac{\bar{z}_{\alpha}}{z}}}\right\rangle\boldsymbol{Y}_{\alpha}\right]\right)\frac{\mathbf{q}_2^{(1)}(\gamma)\mathrm{d}\gamma}{(1+\gamma)^{s}(1-\gamma)^{1/2}}=$$

$$\frac{1}{\sqrt{\pi(1+\chi)}}\Re\left[\boldsymbol{B}\left\langle\sqrt{z}\right\rangle\boldsymbol{B}^{-1}\right]\begin{pmatrix}1\\0\end{pmatrix},$$

$$\int_{-1}^{1}\left(\frac{\boldsymbol{I}}{\gamma-\chi}+\frac{1}{2}\frac{\boldsymbol{I}}{1+\chi+\sqrt{(1+\chi)(1+\gamma)}}+\frac{1}{2}\sum_{\alpha=1}^{2}\Re\left[\boldsymbol{B}\left\langle\frac{1}{1+\chi+\sqrt{(1+\chi)(1+\gamma)\frac{\bar{z}_{\alpha}}{z}}}\right\rangle\boldsymbol{Y}_{\alpha}\right]\right)\frac{\mathbf{q}_1^{(2)}(\gamma)\mathrm{d}\gamma}{(1+\gamma)^{s}(1-\gamma)^{1/2}}=$$

$$-\sin\theta\begin{pmatrix}0\\1\end{pmatrix}. \tag{A.2.5}$$

By application of numerical techniques, Eq. (A.2.5) forms a system of linear algebraic equations. The vectors $\mathbf{q}_1^{(1)}$, $\mathbf{q}_2^{(1)}$, and $\mathbf{q}_1^{(2)}$ can then determine the stress intensity factor $\mathbf{k}^{(k)}$ defined at the crack tip with the radial distance of $r = L_\mathrm{c}$ from the tip of the original crack. Therefore for the exact solution, Eq. (2.8) has the following form

$$\begin{pmatrix}K_{\mathrm{II}}^{(k)}\\K_{\mathrm{I}}^{(k)}\end{pmatrix}=K_{\mathrm{eff}}\frac{\pi\sqrt{\pi}}{2^{s}}\begin{pmatrix}\cos\theta & \sin\theta\\-\sin\theta & \cos\theta\end{pmatrix}\left(\left[\ \mathbf{q}_2^{(1)},\mathbf{q}_1^{(1)}\ \right]\begin{pmatrix}\lambda\\\pm\sqrt{1-\lambda^{2}}\end{pmatrix}+\frac{T\sqrt{L_\mathrm{c}}}{K_{\mathrm{eff}}}\mathbf{q}_1^{(2)}\right). \tag{A.2.6}$$

or

$$\begin{pmatrix} K_{\mathrm{II}}^{(k)} \\ K_{\mathrm{I}}^{(k)} \end{pmatrix} = K_{\mathrm{eff}} \left(\overbrace{\frac{\pi\sqrt{\pi}}{2^s} \begin{pmatrix} \cos\theta & \sin\theta \\ -\sin\theta & \cos\theta \end{pmatrix} \left[\mathbf{q}_2^{(1)}, \mathbf{q}_1^{(1)} \right]}^{[C_{\mathrm{ij}}]} \begin{pmatrix} \lambda \\ \pm\sqrt{1-\lambda^2} \end{pmatrix} + \frac{T\sqrt{L_{\mathrm{c}}}}{K_{\mathrm{eff}}} \overbrace{\frac{\pi\sqrt{\pi}}{2^s} \begin{pmatrix} \cos\theta & \sin\theta \\ -\sin\theta & \cos\theta \end{pmatrix} \mathbf{q}_1^{(2)}}^{[b_{\mathrm{j}}]} \right) . \tag{A.2.7}$$

A.2.2 Approximate solution

Azhdari and Nemat-Nasser [1996] first applied the approximate solution based on modified Irwin's formula in terms of the stress intensity factors $K_{\mathrm{I}}^{(k)}$ and $K_{\mathrm{II}}^{(k)}$, to obtain the energy release rate function. This method was then verified by the fundamental definition of the ERR function, i.e. the work required for closure of the kink gap and restore the required normal and shear stresses defined before kinking. In the approximate solution, $\mathcal{G}(\theta)$ adjacent to the crack tip under the mixed-mode I/II loading condition is calculated from Eq. (2.6) in terms of the vector $\mathrm{k}^{(k)} = \left\{ K_{\mathrm{II}}^{(k)}, K_{\mathrm{I}}^{(k)} \right\}^{\mathsf{T}}$ [Azhdari and Nemat-Nasser, 1996]. Let us now define the coefficients C_{ij} and b_{j} based on the closed-form relations given by Li and Xu [2007]. According to Eq. (2.8), we arrive at

$$\begin{aligned}
C_{11} &= \Re\left[\frac{1}{\mu_1-\mu_2} \left\{ \mu_1 \left(\cos\theta + \mu_2 \sin\theta\right)^{3/2} - \mu_2 \left(\cos\theta + \mu_1 \sin\theta\right)^{3/2} \right\} \right] , \\
C_{12} &= \Re\left[\frac{1}{\mu_1-\mu_2} \left\{ \left(\cos\theta + \mu_2 \sin\theta\right)^{3/2} - \left(\cos\theta + \mu_1 \sin\theta\right)^{3/2} \right\} \right] , \\
C_{21} &= \Re\left[\frac{1}{\mu_1-\mu_2} \left\{ \mu_1 \left(\sin\theta - \mu_2 \cos\theta\right) \sqrt{\cos\theta + \mu_2 \sin\theta} - \mu_2 \left(\sin\theta - \mu_1 \cos\theta\right) \sqrt{\cos\theta + \mu_1 \sin\theta} \right\} \right] , \\
C_{22} &= \Re\left[\frac{1}{\mu_1-\mu_2} \left\{ \left(\sin\theta - \mu_2 \cos\theta\right) \sqrt{\cos\theta + \mu_2 \sin\theta} - \left(\sin\theta - \mu_1 \cos\theta\right) \sqrt{\cos\theta + \mu_1 \sin\theta} \right\} \right] , \\
b_1 &= \sqrt{\frac{8}{\pi}} \sin^2\theta , \\
b_2 &= -\sqrt{\frac{8}{\pi}} \sin\theta \cos\theta .
\end{aligned} \tag{A.2.8}$$

Under the pure mode I loading, the expression given by Nejati et al. [2020a] can be achieved by setting $\lambda = 0$ in the above relation.

A.2.3 Comparison of the approximate solution with dislocation technique

In this section, we present the comparison between the results predicted by the MERR criterion when the ERR function is determined based on the dislocation technique and the approximate solution. According to Section 2.4.2, although the dislocation technique provides the exact solution for the ERR function, the approximate solution can be considered as an alternative method with acceptable accuracy. Table A.2.1 lists the error values associated with each of the techniques used for determining the ERR function. As given in Table A.2.1, the errors calculated for both techniques are in the same order. This implies that the approximate solution provides accurate results as compared to the results of the dislocation technique. However, if the crack kinks at the higher values of θ_0 (e.g. when $\theta_0 > 75°$), the error of the approximate solution might be enlarged [Li and Xu, 2007]. Therefore, we can conclude that as long as the kink crack is small, the approximate solution can be considered as a good candidate for determining the ERR function in anisotropic materials.

Error function	Technique used to derive the ERR function	Set I	Set II	Set III	Set IV	Average
e_{θ_0}	Dislocation technique	1.28	**1.42**	1.52	**1.45**	1.42
	Approximate solution	**1.25**	1.44	**1.50**	1.46	**1.41**
$e_{K^c_{\text{eff}}}$	Dislocation technique	**1.28**	**2.37**	1.55	**1.29**	**1.62**
	Approximate solution	**1.28**	**2.37**	**1.54**	**1.29**	**1.62**

Table A.2.1: Comparison of the prediction errors for different techniques used to determine the ERR function. The error functions are defined in Eq. (2.20).

Appendix B

ELASTICITY PROBLEM: ANISOTROPIC PLANE WITH A HOLE

B.1 Infinite anisotropic plane with a circular hole

The stress field around an intact pressurized wellbore subjected to pre-existing remote loading is derived based on the superposition principle of the problems described as follows. 1) stress-free hole with biaxial loading at remote boundaries (distinguished by the superscript s). 2) uniform pressure acting on the hole and stress-free remote boundaries (distinguished by the superscript p). The superposition of these two problems therefore gives the distributions of the stress components acting in the intact domain V: $\sigma^{\text{int}} = \sigma_\theta(\theta) = \sigma_2\tilde{\sigma}_\theta^{\text{s}} + p_{\text{b}}\tilde{\sigma}_\theta^{\text{p}}$ and $\tau^{\text{int}} = \tau_{r\theta}(\theta) = \sigma_2\tilde{\tau}_{\text{r}\theta}^{\text{s}} + p_{\text{b}}\tilde{\tau}_{\text{r}\theta}^{\text{p}}$. For the sake of simplicity, we express the stress field of each problem in the global coordinate system xyz, and then apply the transformation rule to obtain the dimensionless hoop stresses (i.e. $\tilde{\sigma}_\theta^{\text{s}}$ and $\tilde{\sigma}_\theta^{\text{p}}$) and shear stresses (i.e. $\tilde{\tau}_{\text{r}\theta}^{\text{s}}$ and $\tilde{\tau}_{\text{r}\theta}^{\text{p}}$). The stress field of an infinite anisotropic plate with a stress-free circular hole around the boundary is given by [Amadei, 1983]:

$$\begin{aligned}
&\begin{pmatrix} \sigma_{\mathrm{x}}^{\mathrm{s}} \\ \sigma_{\mathrm{y}}^{\mathrm{s}} \\ \tau_{\mathrm{xy}}^{\mathrm{s}} \end{pmatrix} = \sigma_2 \begin{pmatrix} \tilde{\sigma}_{\mathrm{x}}^{\mathrm{s}} \\ \tilde{\sigma}_{\mathrm{y}}^{\mathrm{s}} \\ \tilde{\tau}_{\mathrm{xy}}^{\mathrm{s}} \end{pmatrix} , \\
&\tilde{\sigma}_{\mathrm{x}}^{\mathrm{s}} = -1 - \Re\left[\sum_{j=1}^{2} \mu_{\mathrm{j}}^2 f_{\mathrm{j}}(\mu_1,\mu_2,\lambda) F_{\mathrm{j}}(\mu_1,\mu_2,\frac{z_j}{R})\right] , \\
&\tilde{\sigma}_{\mathrm{y}}^{\mathrm{s}} = -\frac{1}{\lambda} - \Re\left[\sum_{j+1}^{2} f_{\mathrm{j}}(\mu_1,\mu_2,\lambda) F_{\mathrm{j}}(\mu_1,\mu_2,\frac{z_j}{R})\right] , \\
&\tilde{\tau}_{\mathrm{xy}}^{\mathrm{s}} = \Re\left[\sum_{j=1}^{2} \mu_{\mathrm{j}} f_{\mathrm{j}}(\mu_1,\mu_2,\lambda) F_{\mathrm{j}}(\mu_1,\mu_2,\frac{z_j}{R})\right] ,
\end{aligned} \tag{B.1.1}$$

where

$$\begin{aligned}
&\begin{cases} F_1(\mu_1,\mu_2,\frac{z_1}{R}) = \dfrac{1}{(\mu_1-\mu_2)\,(\pm\sqrt{(\frac{z_1}{R})^2-\mu_1^2-1})\left(\pm\sqrt{(\frac{z_1}{R})^2-\mu_1^2-1}+\dfrac{z_1}{R}\right)} \\ F_2(\mu_1,\mu_2,\frac{z_2}{R}) = \dfrac{-1}{(\mu_1-\mu_2)\,(\pm\sqrt{(\frac{z_2}{R})^2-\mu_2^2-1})\left(\pm\sqrt{(\frac{z_2}{R})^2-\mu_2^2-1}+\dfrac{z_2}{R}\right)} \end{cases} , \\
&\begin{cases} f_1(\mu_1,\mu_2,\lambda) = (1-i\mu_1)\left(-\dfrac{\mu_2}{\lambda}+i\right) \\ f_2(\mu_1,\mu_2,\lambda) = (1-i\mu_2)\left(-\dfrac{\mu_1}{\lambda}+i\right) \end{cases} .
\end{aligned} \tag{B.1.2}$$

Here, μ_1 and μ_2 are the conjugate complex roots of a characteristic polynomial describing the dependency of the elasticity solution on the material constants for the plane anisotropic body [Lekhnitskii, 1968]. Expressing the characteristic equation in the global coordinate xy, we arrive at

$$\tilde{\boldsymbol{S}}_{11}\mu^4 - 2\tilde{\boldsymbol{S}}_{16}\mu^3 + (2\tilde{\boldsymbol{S}}_{12} + \tilde{\boldsymbol{S}}_{66})\mu^2 - 2\tilde{\boldsymbol{S}}_{26}\mu + \tilde{\boldsymbol{S}}_{22} = 0 \ , \tag{B.1.3}$$

where the coefficients $\tilde{\boldsymbol{S}}_{\mathrm{ij}}$ represent the components of the material compliance matrix and given by [Nejati et al., 2020b]. In Eq. B.1.2, the ratios z_j/R $(j = 1, 2)$ are defined in the domain V as $z_j/R = \delta(\cos\theta + \mu_1 \sin\theta)$. Here, δ is defined as the ratio r/R, where r denotes the radial distance between the crack tip and the wellbore center.

The second problem incorporates the contribution of the internal pressure p_{b} applied to the hole. Recalling the functions $F_{\mathrm{j}}(\mu_1, \mu_2, \frac{z_{\mathrm{j}}}{R})$ given in Eq B.1.2, the components $\tilde{\sigma}^{\mathrm{p}}_{\mathrm{x}}$, $\tilde{\sigma}^{\mathrm{p}}_{\mathrm{y}}$, and $\tilde{\tau}^{\mathrm{p}}_{\mathrm{xy}}$ are defined as [Savin, 1961; Sadd, 2014]

$$\begin{cases} \tilde{\sigma}^{\mathrm{p}}_{\mathrm{x}} = \Re\left[\sum_{j=1}^{2} \mu_{\mathrm{j}}^2 g_{\mathrm{j}}(\mu_1, \mu_2) F_{\mathrm{j}}\right], \\ \tilde{\sigma}^{\mathrm{p}}_{\mathrm{y}} = \Re\left[\sum_{j=1}^{2} g_{\mathrm{j}}(\mu_1, \mu_2) F_{\mathrm{j}}\right], \\ \tilde{\tau}^{\mathrm{p}}_{\mathrm{xy}} = -\Re\left[\sum_{j=1}^{2} \mu_{\mathrm{j}} g_{\mathrm{j}}(\mu_1, \mu_2) F_{\mathrm{j}}\right], \end{cases} \quad \text{where} \quad \begin{pmatrix} g_1(\mu_1, \mu_2) = (\mu_1 + i)(1 + i\mu_2) \\ g_2(\mu_1, \mu_2) = (\mu_2 + i)(1 + i\mu_1) \end{pmatrix}. \tag{B.1.4}$$

B.2 Infinite anisotropic plane with an inclusion

The simple Cauchy kernel is common to integral equations governing the crack problems provided that the entire crack lies within the homogeneous part of the material [Hills et al., 1996]. Any additional terms of the kernel components are introduced to the problem by the differences in the geometry and presence of inclusions. Many attempts have so far been made to derive closed-form solutions to a variety of crack problems. Particularly, the present problem entails knowledge on the stress field when the dislocation is interacting with a circular hole embedded inside an infinite anisotropic plane. Fortunately, Wu [1992] has derived the closed-form solution of a dislocation with an elliptic inclusion in an anisotropic material. In this context, an infinitely soft inclusion with equal semi-axes mimics the desired configuration for a cylindrical wellbore located in a transversely isotropic formation [Wu, 1992]. Assuming $z_\alpha = X + \mu^*_\alpha Y$ and $z_{\alpha 0} = \boldsymbol{X}_{01} + \mu^*_\alpha \boldsymbol{X}_{02}$, the matrix components $\boldsymbol{J}_{\mathrm{ij}}(z, z_0)$ on the plane $Y = 0$ can be expressed as

$$\begin{aligned}
\boldsymbol{J}_{11}(X,\boldsymbol{X}_{01}) &= \boldsymbol{J}_{11}(z,z_0)|_{\substack{Y=0,\\ \boldsymbol{X}_{02}=0}} = \Re\left[\boldsymbol{B}_{11} i \boldsymbol{\mathcal{J}}_{11,z}(z,z_0)|_{\substack{Y=0,\\ \boldsymbol{X}_{02}=0}}\right] + \Re\left[\boldsymbol{B}_{12} i \boldsymbol{\mathcal{J}}_{21,z}(z,z_0)|_{\substack{Y=0,\\ \boldsymbol{X}_{02}=0}}\right] + \Im\left[\boldsymbol{\mathcal{J}}^{*}_{11,z}(z,z_0)|_{\substack{Y=0,\\ \boldsymbol{X}_{02}=0}}\right]\\
\boldsymbol{J}_{12}(X,\boldsymbol{X}_{01}) &= \boldsymbol{J}_{12}(z,z_0)|_{\substack{Y=0,\\ \boldsymbol{X}_{02}=0}} = \Re\left[\boldsymbol{B}_{11} i \boldsymbol{\mathcal{J}}_{12,z}(z,z_0)|_{\substack{Y=0,\\ \boldsymbol{X}_{02}=0}}\right] + \Re\left[\boldsymbol{B}_{12} i \boldsymbol{\mathcal{J}}_{22,z}(z,z_0)|_{\substack{Y=0,\\ X_{02}=0}}\right] + \Im\left[\boldsymbol{\mathcal{J}}^{*}_{12,z}(z,z_0)|_{\substack{Y=0,\\ \boldsymbol{X}_{02}=0}}\right]\\
\boldsymbol{J}_{21}(X,\boldsymbol{X}_{01}) &= \boldsymbol{J}_{21}(z,z_0)|_{\substack{Y=0,\\ \boldsymbol{X}_{02}=0}} = \Re\left[\boldsymbol{B}_{21} i \boldsymbol{\mathcal{J}}_{11,z}(z,z_0)|_{\substack{Y=0,\\ \boldsymbol{X}_{02}=0}}\right] + \Re\left[\boldsymbol{B}_{22} i \boldsymbol{\mathcal{J}}_{21,z}(z,z_0)|_{\substack{Y=0,\\ \boldsymbol{X}_{02}=0}}\right] + \Im\left[\boldsymbol{\mathcal{J}}^{*}_{21,z}(z,z_0)|_{\substack{Y=0,\\ \boldsymbol{X}_{02}=0}}\right]\\
\boldsymbol{J}_{22}(X,\boldsymbol{X}_{01}) &= \boldsymbol{J}_{22}(z,z_0)|_{\substack{Y=0,\\ \boldsymbol{X}_{02}=0}} = \Re\left[\boldsymbol{B}_{21} i \boldsymbol{\mathcal{J}}_{12,z}(z,z_0)|_{\substack{Y=0,\\ \boldsymbol{X}_{02}=0}}\right] + \Re\left[\boldsymbol{B}_{22} i \boldsymbol{\mathcal{J}}_{22,z}(z,z_0)|_{\substack{Y=0,\\ X_{02}=0}}\right] + \Im\left[\boldsymbol{\mathcal{J}}^{*}_{22,z}(z,z_0)|_{\substack{Y=0,\\ \boldsymbol{X}_{02}=0}}\right]\\
&.
\end{aligned} \tag{B.2.1}$$

where the Stroh Matrix $\boldsymbol{B}$ in Eq. B.2.1 is

$$\boldsymbol{B} = \begin{pmatrix} -k_1\mu_1^* & -k_2\mu_2^* \\ k_1 & k_2 \end{pmatrix}, \tag{B.2.2}$$

and the matrices $\boldsymbol{\mathcal{J}}(z,z_0)$ and $\boldsymbol{\mathcal{J}}^*(z,z_0)$ on the plane $Y=0$ can be expressed as

$$\begin{aligned}
&\boldsymbol{\mathcal{J}}^*(z,z_0) = [\boldsymbol{B}\left\langle \ln(z-z_0) - \ln(z+z_0)\right\rangle \boldsymbol{B}^{\intercal}]\\
&\boldsymbol{\mathcal{J}}(z,z_0) = \left[\left\langle \ln(1-\frac{m}{g(z)g(z_0)}) - \ln(1-\frac{m}{g(z)g(-z_0)})\right\rangle \boldsymbol{B}^{\intercal} - \boldsymbol{G}(z,z_0)\bar{\boldsymbol{B}}^{\intercal}\right], \text{ where } \quad m = \frac{1+i\mu^*}{1-i\mu^*},\\
&g(z) = \frac{z}{R(1-i\mu^*)} + \sqrt{(\frac{z}{R(1-i\mu^*)})^2 - m}\\
&\boldsymbol{G}_{\mathrm{jk}}(z,z_0) = (\boldsymbol{B}^{-1}\bar{\boldsymbol{B}})_{\mathrm{jk}}(\ln(1-\frac{1}{g(z_{\mathrm{j}})\bar{g}(z_{\mathrm{k0}})}) - \ln(1-\frac{1}{g(z_{\mathrm{j}})\bar{g}(-z_{\mathrm{k0}})}))
\end{aligned} \tag{B.2.3}$$

In Eqs. B.2.2 and B.2.3, the complex parameters μ_k^* must be defined along the initiation direction θ_0, and thus the complex parameters μ_k obtained from Eq. B.1.3, are transformed into the local coordinate system XY by [Lekhnitskii, 1968]

$$\mu_{\mathrm{k}}^* = \frac{\mu_{\mathrm{k}}\cos\theta_0 + \sin\theta_0}{\cos\theta_0 - \mu_{\mathrm{k}}\sin\theta_0}\,, \qquad \mathrm{k} = 1, 2. \tag{B.2.4}$$

Appendix C

MODELING HYDRAULIC FRACTURE INITIATION

In Chapter 3, we applied the mixed criterion to study hydraulic fracture initiation from a notch-free wellbore subjected to compressive in-situ stresses, situated in a transversely isotropic rock formation. To address the requirement of the mixed criterion, we employed the displacement discontinuity method to calculate the fracture energy, where a kernel matrix tailored to the geometry in question is adopted. Particularly in our study, this kernel must well describe the stress induced by a unit edge dislocation interacting with a wellbore within a transversly isotropic formation. The mathematical complexity inherent in this kernel demands a comprehensive assessment of the correctness of the mathematical relationships. Despite the validation given in the preceding chapter, the reliability of the results remained unconfirmed. This is due to this fact that isotropic material represents a specific instance of anisotropy, and unlike the rock formation assumed in Chapter 3, it is independent of material orientation.

C.1 Finite element modelling

To calculate the fracture energy through finite element modelling, we created two separate 2D models for the crack-free and cracked states, where an infinite plane containing a circular hole is taken as a transversely isotropic formation. While all the boundary conditions between these two states is kept unchanged, the introduction of symmetrical cracks to an initially notch-free wellbore yields a variation in elastic strain energy between the two states. Following the elemental crack advancement approach, this variation serves as an indicator of the fracture energy. The ANSYS APDL scripts utilized to simulate these two states are available online on GitHub[1]. However, to ensure the correctness of finite element implementation, we first compare the finite element (FE) and analytical distribution of the hoop stress surrounding the initially notch-free wellbore, where the fluid is pressurized up to the initiation pressure and the formation is subjected to the stress anisotropy of $\lambda = 2$. The distribution at the distance of 103 mm away from the wellbore center is presented in Figure C.1.1, depicting two material anisotropy ratios (i.e. $\xi = 3$ and $\xi = 4$) with three different material anisotropy orientations. To extract the initiation pressures corresponding to each variation, the readers are referred to the findings outlined in Chapter 3.

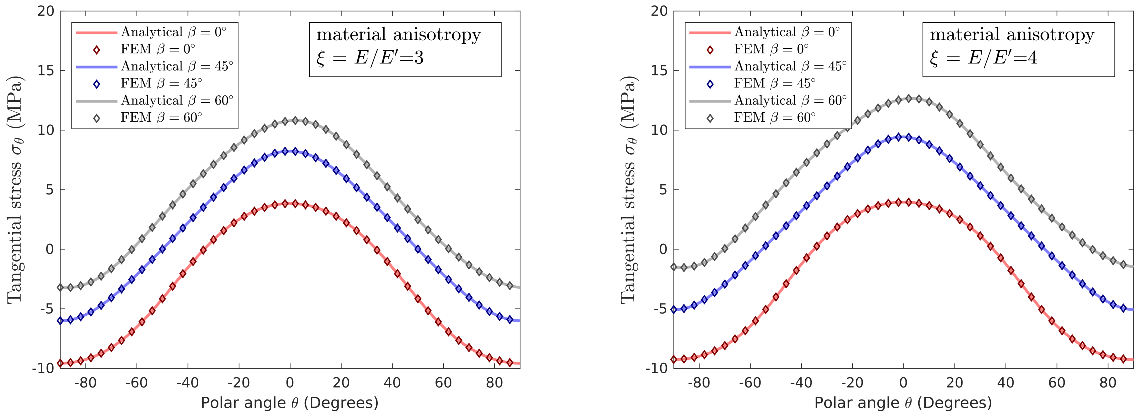

(a) (b)

Figure C.1.1: The distribution of the hoop stress around the notch-free wellbore at initiation obtained by finite element (FE) modelling and analytical relations (see B.1) for different material anisotropy ratios and orientations.

Once the finite element implementation is validated, we employed a python automation script to loop over different initiation pressures in such a way that three conditions of the mixed criterion are met. This script, responsible to automate ANSYS simulations, can also be accessed on GitHub at the same repository[1]. In the context of a stress anisotropy of $\lambda = 2$, Figure C.1.2 compares the initiation parameters calculated through finite element (FE) modelling and the displacement discontinuity method (DDM). As shown in Figure C.1.2,

---

[1] `https://github.com/mahsasakha/FE_Crack_Anisotropic_Formation.git`

the initiation parameters of two different approaches are in agreement for the case of $\lambda = 2$, where the highest deviations of the initial crack from the isotropy plane are observed. Therefore, this comparison can confirm the correctness of the kernel matrix defined in Chapter 3.

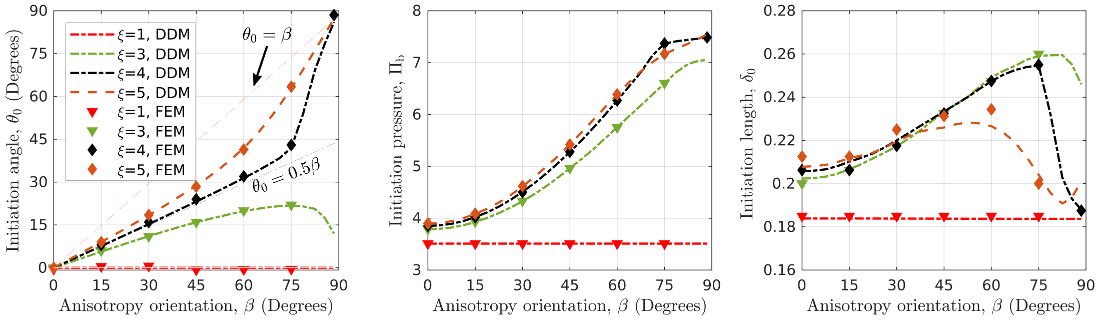

Figure C.1.2: Comparing wellbore initiation parameters calculated through FEM and DDM for various material anisotropy under stress anisotropy $\lambda = 2$.